Cronfa
Swansea University's Research Repository

Mechanics of Micro-Architected Lattice Structures

Swansea University
Engineering Department

A dissertation
submitted to Swansea University
for the Degree of MSc

by

Frances Micah Arago

2023

Copyright: The Author, Frances M. Arago, 2023.

Declaration

This work has not previously been accepted in substance for any degree and is not being concurrently submitted in candidature for any degree.

Signed: *FRANCES MICAH ARAGO*
Date: 16/12/2021

This thesis is the result of my own investigation, except where otherwise stated. Where correction services have been used, the extent and nature of the correction is clearly market in a footnote(s).

Signed: *FRANCES MICAH ARAGO*
Date: 16/12/2021

I hereby give consent for my thesis, if accepted, to be available for photocopying and for inter-library load, and for the title and summary to be made available to outsider organisations.

Signed: *FRANCES MICAH ARAGO*
Date: 16/12/2021

The University's ethical procedures have been followed and, where appropriate, that ethical approval has been granted.

Signed: *FRANCES MICAH ARAGO*
Date: 16/12/2021

Acknowledgements

First and foremost, I would like to express my sincere thanks and gratitude to my supervisor, Professor Sondipon for his continuous guidance, patience and understanding throughout the course of this project.

Also, I would like to thank my co-research students, Shuvajit Mukherjee and Yatish Chandra for their support, and advice during the course of this research paper, especially through the difficult stages with finite element analysis. As well as Erlyne Limbo for her support and feedback.

And last but not least, my parents, Carmela and Vincent Arago, for their unending support and encouragement in all my endeavours.

Abstract

Honeybees construct nests that consist of tessellated hexagonal prismatic structures. The bees develop a linear succession of tetrapod structures that serve as the nest's foundation in the initial stage of construction. This natural hexagonal lattice structure has been the epitome of extensive aerospace applications. And, has particularly been widely used on aircraft control surfaces as they provide an ideal set of mechanical properties; minimal density and ability to withstand high magnitudes of compressive and shear force.

This paper analyses this hexagonal lattice configuration using theoretical analysis and simulations. It first analyses the lattice structure by breaking it down into three individual components somewhat resembling the constructional stages in which the nests are developed: cantilever beam, unit cell which is initially the tetrapod structure, and the complete system of the lattice itself.

In further chapters, refined geometries, namely stepped and quadratic lattice of the honeycomb, are then analysed with the objective of enhancing its strength to weight ratio, this is again analysed through the same bottom-up approach and procedure. Two approaches are implemented in the enhancement procedure. The obtained numerical results are then reviewed through simulations using multiple computer-aided software, Solidworks and ANSYS where the mechanical properties are established and compared.

Contents

List of Figures

10(a) Hexagonal lattice structure experiencing a compressive stress in both directions 1 and 2

10(b) Force in the constituent beams within the unit cell model. The compressive axial force is equivalent to $P\cos\theta + W\sin\theta$ with $P = \sigma 1 b (h + l \sin\theta)$ and $W = \sigma 2 b l \cos\theta$

(11) Contours of the Poisson's ratios and normalised effective elastic moduli of a lattice subjected to a compressive stress in directions 1 and 2 corresponding to fig. (9). The contours of a unit cell with a cell angle of 30 degrees are plotted as normalised compressive stress in both directions with $\alpha = t/l = 0.15$ and $\beta = h/l = 1$.

12(a) Hexagonal lattice structure experiencing a tensile stress in 1-direction

12(b) Force in the constituent beams within the unit cell model. The tensile axial force is equivalent to $P\cos\theta$ with $P = \sigma 1 b (h + l \sin\theta)$.

(13) Equivalent normalised Young's modulus, $(E_1/E\alpha^3)$ against the normalised tensile stress $(\sigma_1/E\alpha^3)$ in direction-1 as shown in fig. (11). A comparison of the analytical expressions results and finite element analysis results are presented. Two different hexagonal lattice geometries are analysed and considered in (a) and (b).

(14) Contours of the Poisson's ratios and normalised effective elastic moduli of a lattice subjected to a tensile stress in direction 1 corresponding to fig. (11). The normalised tensile stress $(\sigma_1/E\alpha^3)$ varies in the x-axis as well as the cell angle in the y-axis. The geometric dimensional ratios are $\alpha = t/l = 0.15$ and $\beta = h/l = 1$.

(15) (a) Hexagonal lattice structure experiencing a tensile stress in the 2-direction
(b) Force in the constituent beams within the unit cell model. The tensile axial force is equivalent to $W\sin\theta$ with $W = \sigma 2 b l \cos\theta$.

(16) Contours of the Poisson's ratios and normalised effective elastic moduli of a lattice subjected to a tensile stress in direction 2 corresponding to fig. (7). The normalised tensile stress $(\sigma_2/E\alpha^3)$ varies in the x-axis as well as the cell angle in the y-axis. The geometric dimensional ratios are $\alpha = t/l = 0.15$ and $\beta = h/l = 1$.

(17) (a) Hexagonal lattice structure experiencing a tense e stress in both directions 1 and 2
(b) Force in the constituent beams within the unit cell model. The tensile axial force is equivalent to $P\cos\theta + W\sin\theta$ with $P = \sigma_1 b (h + l \sin\theta)$ and $W = \sigma_2 b l \cos\theta$

(18) Contours of the Poisson's ratios and normalised effective elastic moduli of a lattice subjected to a tensile stress in directions 1 and 2 corresponding to fig. (9). The contours of a unit cell with a cell angle of 30 degrees are plotted as normalised tensile stress in both directions with $\alpha = t/l = 0.15$ and $\beta = h/l = 1$.

(19) Dimensions of Unit Cell Model; length (l), height (h) and thickness (t).

(20) Three graphs for the results of Case 1 where $\theta = 30$ degrees are illustrated.
(a) Young's Modulus against Strain value
(b) Young's Modulus against Stress value
(c) Normalised Axis

(21) Three graphs for the results of Case 1 where θ = 45 degrees are illustrated.
(a) Young's Modulus against Strain value
(b) Young's Modulus against Stress value
(c) Normalised Axis

(22) Three graphs for the results of Case 4 where θ = 30 degrees are illustrated.
(a) Young's Modulus against Strain value
(b) Young's Modulus against Stress value
(c) Normalised Axis

(23) Three graphs for the results of Case 4 where θ = 45 degrees are illustrated.
(a) Young's Modulus against Strain value
(b) Young's Modulus against Stress value
(c) Normalised Axis

(24) Three special 2D geometric cases are illustrated.
(a) The auxetic lattice where θ is negative
(b) The rhombus lattice where h=0
(c) The rectangular lattice where θ=0. The corresponding and degenerated unit cells are highlighted in red in the figures.

25(a) Stepped Lattice Geometry

25(b) Corresponding Unit Cell of the stepped lattice seen in (a)

(26) Dimensions of Uniform Beam

(27) Dimensions of Stepped Beam

28(a) Schematic of step-up beam model i.e. where $t_1 > t_2$

28(b) Schematic of step-down beam model i.e. where $t_1 > t_2$

(29) Stepped Lattice and a detailed view of its corresponding unit cell to show how the unit cell is multiplied and developed to make the whole system

(30) Mesh Convergence Results for Case 2a

(31) The simulation set up of the lattices to be tested where the blue areas are where the fixed support was applied whilst the red cross-sectional areas represent where the magnitude of forces were subjected

(32) The relationship between the stress and strain for all cases
(a) Case 1 Results
(b) Case 2a Results
(c) Case 2b Results
(d) Case 3a Results
(e) Case 3b Results
(f) Case 3c Results

(33) The finite results for all cases where the relationship is shown between the young's modulus and force whilst also a single plot is shown for the theoretical young's modulus value

(a) Case 1 Results
(b) Case 2a Results
(c) Case 2b Results
(d) Case 3a Results
(e) Case 3b Results
(f) Case 3c Results

(34) Dimensions of Uniform Beam

(35) Dimensions of Optimised Beam

(36) Co-ordinates of Optimised Beam with quadratic profile

(37) Non-uniform beam subjected to a downwards force, P.

(38) Dimensions and geometry of Unit Cell with epsilon value of 0.1

(39) Mesh Convergence Results for Epsilon=0

40(a) Arrow indicating where force is applied on a beam model with an epsilon value of 0.4

40(b) Beam model with an epsilon value of 0.4 where the green covered face area indicates the location in which the fixed support is applied

(41) Simulation set up of unit cell model with epsilon value of 0.2 where the blue covered face indicates where the fixed support has been applied and the red arrows indicating where the fore is subjected upon.

(42) Model of Lattice with ε=0.3136

(43) Faces of Lattices indicated by blue covered area that are subjected to compressive forces

(44) Faces of Lattices with fixed supports

(45) Numerical and Finite Element Analysis Results

(46) Results of Unit Cell Models where the ratio of the uniform unit cell deformation

(47) Finite Element Results of Lattice Models where the ratio of Young's Modulus for the uniform model and altered model is plotted again the epsilon value corresponding to individual lattice models

List of Tables

Chapter 1 – Preface

1.1 Introduction

Through recent years, three-dimensional (3D) printing technologies have progressed significantly and have become a revolutionary advancement in the way products have been developed and manufactured. Due to this technological phenomenon, it has opened the world to new methods of manufacturing products, it is not only harnessed by large scale industries but directly by the consumer [1].

Additive Manufacturing (AM) or Additive Layer Manufacturing (ALM), more widely known as 3D printing, is a manufacturing process which uses computer aided design (CAD) [2]. ALM is implemented by means of developing models and structures of various scales and intricacies by combining materials layer by layer using a method called fused depositional modelling (FDM) [3]. This can include micron level additive manufacturing in the 10–20-micron range to a build volume of 1.4m x 1.11m x 1.5m [4-5]. Each layer is equivalent to a thin cross-section of the CAD model. Configurations developed through ALM are fundamentally different from traditionally made structures due to the variance in the interior configuration. The structure can be manipulated and altered in numerous ways. Some of the multiple parameters that can be applied to a 3D printed component include diversifying the volume fractions, ranging from 0 – 100% or altering the internal configuration that the model could entail [6]. These infill structures include honeycomb, grid, and concentric circles [7]. Predictably, combining different parameters would greatly affect the mechanical properties of the design. For instance, increasing the density comes with increasing strength but undesirably increasing the weight.

By combing the comprehensive array of materials that can now be utilised and this new manufacturing approach, it provides unique advantages over conventional manufacturing. It can reduce costs, increase production speed as well as allowing for unlimited complex and customisable designs without an added cost [8-17]. In particular, the sustainable aspect that ALM provides is of particular interest as this would reduce material wastage bringing forth a further reduction in cost.

At present, there are a wide range of experimental and theoretical studies carried out worldwide focusing on the superior parameter combinations. However, as ALM is a relatively

new advancement, there is a lack of thorough analysis and investigation into the possible irregular geometries that could perform well in all areas.

Therefore, this paper will examine a specific infill pattern, in this instance the hexagonal arrangement, better known as the honeycomb structure. This particular infill was chosen due to its presence in nature and due to the fact, it has already been extensively used on aircraft surfaces. Further investigation could potentially influence the alteration of current manufactured components. The objective, in the interest of aerospace applications, is to optimise the resistive capability to deformation of the altered structure, whilst maintaining the mass of the uniform configuration. In a simplified manner, to ultimately achieve minimal deformation[18]. The investigation involves an in-depth analysis of the structure when subjected to compressive and tensive forces in the horizontal and vertical direction, both together and separately. A probable complication of uniform hexagonal structures is the positive Poisson's ratio that they entail. This would result in the elongation of the structure in the direction parallel to the load and analogously, minimise the cross-sectional area perpendicular to the load. This can result in failure. Thus, by taking this into consideration two approaches are analysed in the enhancement procedure through the distribution of the cross-sectional area: the introduction of 'steps' in the lattice structure and profile optimisation.

To achieve this, numerous models are created using the CAD software, Solidworks and then simulated on another CAD software, ANSYS. Two software are used in the simulation process as each have their own area of expertise; ANSYS has the ability to analyse the structure created by Solidworks in a more thorough manner. Comparisons between the theoretical results and finite element analysis (FEA) results will then be developed and discussed.

1.2 Thesis Layout

The paper is structured into 3 main chapters (2, 3, 4) which is further split into various sections and subsections. Conclusions and summaries are then written in the chapter 5, the final chapter.

1.2.1 Hexagonal Lattice Analysis

The second chapter of this paper establishes the theoretical foundation required to understand the nonlinear dynamics of hexagonal lattice configurations subjected to in-plane compressive and tensile stresses. As previously stated, the bottom-up approach is used where analysis begins

at the unit cell, then subsequently a complete complex system of an entire lattice. Results are validated through different approaches and methods: numerical analysis and finite element analysis. The physical properties of lattice materials such as malleability and high compressibility are among the reasons, they perfectly fulfil the criteria to be exploited in a range of revolutionary and innovative engineering applications.

With the aim of analysing and designing optimised and intricate cellular metamaterials, a high level of physics-based understanding is crucial. In conjunction with this, choosing the correct computational approach to use is of utmost importance. The analysis of the honeycomb structure consists of splitting it into individual segments and where further analysis is conducted for each separate subdivision. Again, this is more widely known as the bottom-up approach [19-25].

The constitutive beam elements' stiffness matrices coefficients are used to express the nonlinear equivalent elastic modulus and Poisson's ratios of the stressed lattice. Transcendental displacement function allows the derivation of the stiffness coefficients required. These are the exact solutions of corresponding governing ordinary differential equations with appropriate boundary conditions. The closed-form analytical equivalent elastic properties of the lattice are expressed in terms of different functions depending on the stress that is subjected upon the structure. For the compressive case, it is expressed in terms of trigonometric functions whilst contrarily, when subjected to a tensile stress it is expressed as a hyperbolic function.

Three special cases of diverse lattice structures are then investigated using these general expressions: auxetic hexagonal, rhombus-shaped, and rectangular lattices. The analytical expressions derived are then validated through finite element simulations, specifically independent nonlinear computational analysis. Separate numerical expressions were developed for lattices under applied loads in multiple directions. It is shown that the equivalent elastic moduli act adversely when under compression and tension, a softening effect and stiffening effect occurs respectively. It is important to note that the Poisson's ratios are not significantly dependent on the applied stresses and thus are not entirely significant in these cases but will continue to be discussed. The proposed analytical methodology, as well as the recent closed-form expressions offer a computationally effective and mechanically intuitive structure for the study and parametric nature of lattice materials subjected to external stresses.

1.2.2 Stepped Lattice

The third chapter of this paper explores one approach of optimising a hexagonal lattice configuration through varying the geometry of the constitutive beam elements by introducing ‘steps. The analysis consists of the same procedures as the preceding chapter where the hexagonal honeycomb structure is separated into sub systems and individually analysed. This would then be pieced together to develop the complex lattice which is then again analysed as a whole system. The two major forms to be investigated and demonstrated are ‘step-up’ and ‘step-down’ geometries, further defined in the chapter. Likewise, the validation of results is then again executed through different approaches and methods: numerical analysis and finite element analysis.

The objective of this analysis is the development of a geometry with a heightened deformation resistance whilst maintaining the mass of the uniform structure. It is crucial that the mass of the altered structure is maintained for comparison purposes. The main focal point is the derivation of the closed form expressions of these ‘stepped’ hexagonal lattices. Further objectives include investigating the effect of redistributing the mass in the constitutive beam elements whilst of course as previously mentioned maintaining the uniform beam mass. This combined with obtaining a range of equivalent elastic parameter values which can then be manipulated for design purposes and achieve the criteria.

In the same manner as the preceding chapter, the numerical theory developed can be compared to the current beam theory that has been researched; Euler-Bernoulli beam theory. These are exploited to derive the closed form derivations.

1.2.3 Quadratic Profile

The fourth chapter of this paper investigates another approach of optimising the hexagonal configuration but in this instance through varying the beam profile by introducing a quadratic curve merely due to its simplicity and also as the thickness of the member is so small, using higher order curves are not necessary as it wouldn’t have a huge additional impact. Identical procedures are implemented as the first optimising approach.

For the attainment of theoretical values, boundary conditions were first put into place to find the unknown constants of the beam element. Subsequently, analysis is then conducted on the unit cell which would consist of an inclined angle of 30 degrees. It is important to note that necessary changes in the numerical analysis could be made to the derivations if the inclined

angle was any other value. The numerical analysis of this piece of the lattice consists of the formulation of the individual cantilever beams' local stiffness matrices and transforming them into a global coordinate system resembling the lattice. Initially, the derivation of the lattice expressions is derived from the unit cell. Periodic boundary conditions were applied for a minimum number of unit cells i.e., an assumption made is the deformation of one-unit cell is identical to all the other unit cells. The establishment of stiffness matrix coefficients is of absolute importance and continues to be an objective of the paper as it allows the strength comparisons to be made between the uniform and optimised lattice.

Chapter 2 – Hexagonal Lattice Analysis

2.1 Summary

This chapter summarises the findings of [26] and sets out much of the analytical framework that is then used to extend this work to refined geometries. Beginning from subsection 2.2 of Chapter 2. This section presents the elasticity tensor of 2D lattices along with the unit cell approach used to obtain the equivalent elastic properties. The equivalent elastic properties of 6 cases are investigated: 3 cases for compression and 3 in tension. These properties include elastic moduli, Poisson's ratio, and shear modulus. In closed form, the elements of the elasticity tensor are expressed in terms of the stiffness matrix coefficients of the beams within the unit cell.

In the next section, subsection 2.3, the Euler-Bernoulli beam is analysed when subjected to axial forces. Three cases are considered: (a) using the classical finite element method, the stiffness matrix can be obtained, (b) the exact stiffness matrix can be obtained when subjected to a compressive axial force, and (c) the exact stiffness matrix can be obtained when subjected to a tensile axial force. In summary, the derivation of the stiffness matrix of the beam is obtained in this section. And from this, the expression of the equivalent elastic properties of the lattice can then be obtained.

Subsection 2.4 illustrates and deliberates hexagonal lattice configurations subjected to compressive stresses. Again, three separate scenarios are considered: (a) compressive stresses in the horizontal direction, (b) compressive stresses in the vertical direction and (c) compressive stresses in both directions.

The same three cases are discussed in subsection 2.5 but with forces in tension. Subsection 2.6 describes the methodology and finite element analysis procedures for the simulations. Subsection 2.7 discusses and compares the results of the two approaches: numerical and finite element analysis. Subsection 2.8 applies the general theoretical framework for the equivalent elastic properties of strained hexagonal lattices to various lattice geometries. Auxetic hexagonal lattices, rhombus-shaped lattices, and rectangular lattices are among the special cases studied. The five equivalent elastic constants have exact closed-form expressions that have been explicitly derived.

And finally, subsection 2.9 and 2.10 summarises all the analysis and discussions of each section and conclusions are drawn based on the findings obtained as well as recommendations for future research.

2.2 Equivalent elastic moduli of hexagonal lattices

2.2.1 The elasticity tensor of 2D lattices

A key property when performing global stress-strain analysis on a lattice material is the effective elastic property. The expression for an in-plane elastic 2D material is as follows:

$$\begin{Bmatrix} \varepsilon_{11} \\ \varepsilon_{22} \\ 2\varepsilon_{12} \end{Bmatrix} = \begin{bmatrix} 1/E_1 & -v_{21}/E_2 & 0 \\ -v_{12}/E_1 & 1/E_2 & 0 \\ 0 & 0 & 1/G_{12} \end{bmatrix} \begin{Bmatrix} \sigma_{11} \\ \sigma_{22} \\ \sigma_{12} \end{Bmatrix} \quad (1)$$

This expression is developed based on the orthotropic material. The representation of each symbol within the 2D material is as follows:

- $\varepsilon_{(-)}$ – Strain
- $\sigma_{(-)}$ – Stress
- E_1 – Transverse Young's Modulus
- E_2 – Longitudinal Young's Modulus
- G_{12} – Shear Modulus
- v_{12}, v_{21}– Poisson's Ratios

The stress-strain relationship can be defined by these properties. This can be illustrated by inverting the coefficient matrix in eq. (1) as

$$\begin{Bmatrix} \sigma_{11} \\ \sigma_{22} \\ \sigma_{12} \end{Bmatrix} = \begin{bmatrix} E_1/(1-v_{12}v_{21}) & v_{21}E_1/(1-v_{12}v_{21}) & 0 \\ v_{12}E_2/(1-v_{12}v_{21}) & E_2/(1-v_{12}v_{21}) & 0 \\ 0 & 0 & G_{12} \end{bmatrix} \begin{Bmatrix} \varepsilon_{11} \\ \varepsilon_{22} \\ 2\varepsilon_{12} \end{Bmatrix} \quad (2)$$

With the assumption that the material is subjected to large magnitudes of external stress, the elastic constants will be affected and thus require to be altered. Furthermore, with the assumption of linear material behaviour, it is also important to consider geometric nonlinearity arising due to large deformation. The equations below can then be obtained from eq. (2):

$$\sigma_{11}(\mu) = \frac{E_1(\mu)}{\left(1 - v_{12}(\mu)v_{21}(\mu)\right)}\left(\varepsilon_{11}(\mu) + v_{21}(\mu)\varepsilon_{22}(\mu)\right)$$
$$\sigma_{22}(\mu) = \frac{E_2(\mu)}{\left(1 - v_{12}(\mu)v_{21}(\mu)\right)}\left(v_{12}(\mu)\varepsilon_{11}(\mu) + \varepsilon_{22}(\mu)\right) \quad (3)$$
$$\sigma_{12}(\mu) = G_{12}(\mu)[2\varepsilon_{12}(\mu)]$$

Definition of μ is defined later in the paper, please refer to Eq. (20).

As seen in eq. (3), three elastic moduli and two Poisson's ratios, better known as the five elasticity constants, are put as functions of μ, a scalar parameter. This represents the external stress that the lattice is subjected to. The exact expression of this parameter will depend on the nature of the applied stress, but this will be further investigated and discussed later in the paper. The analysis of complex systems such as a lattice structure with embedded cellular materials is overseen by boundary value problems. It is found that generally, various numerical methods including finite element analysis are crucial to solve these problems. These methods allow the use of stress-dependent elasticity constants which allow coarser discretisation leading to an efficient computational approach. The efficiency is dependent upon the existence and implementation of these elasticity constants as they take account the nonlinear stress-strain relationship that is seen in eq. (3).

2.2.2 The Unit Cell Approach

The effective elastic property of a lattice structure can be obtained using the periodicity of a suitably selected unit cell. In fig. (1), a hexagonal lattice configuration is illustrated with its corresponding unit cell. The unit cell can be seen repetitively throughout the lattice where the unit cell is tessellated creating the entire lattice. When subjected to in-plane compressive and tensile stresses, each of the unit cell walls will uniformly bend and expand/compress. On the other hand, when subjected to out-of-plane uniform stresses, the three segments of the unit cell in fig. 1(b) can be represented as single beam elements. Each of these elements are seen in fig. 1(c) with six degrees of freedom and two nodes on each end. Thus, the stiffness matrix of fig. 1(c) can be expressed by a 6 x 6 matrix with degrees of freedom at each node corresponding to the multiple deformations: axial, transverse and rotational. The equivalent elastic moduli of

hexagonal cellular materials are obtained by Gibson and Ashby as eq. (4 - 8) [24]. It is important to note that the expansive/compressive deformations are ignored and only the bending deformation is considered in these expressions.

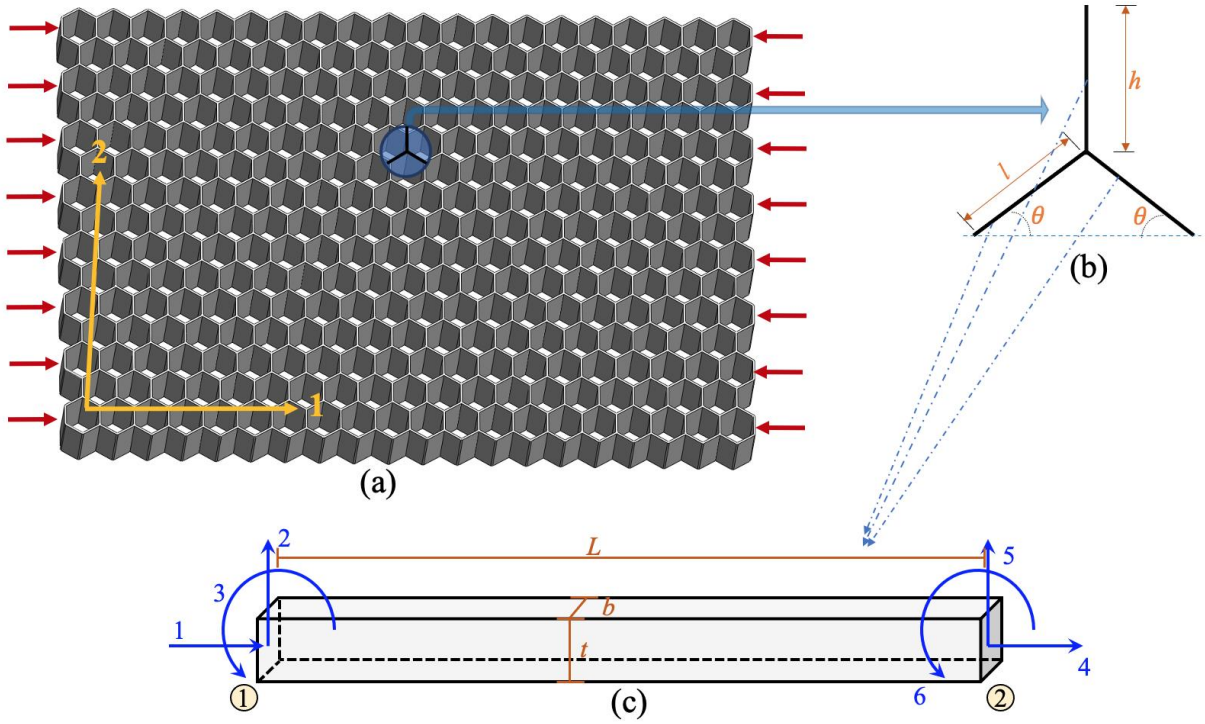

Fig. 1(a) Illustration of a hexagon lattice structure under compressive stress in direction- 1 only
Fig. 1(b) A single unit cell used to analyse the entire lattice structure
Fig. 1(c) A beam element (representing the three different segments/beams in the unit cell model) with two nodes on each end as well as six degrees of freedom. Each degree of freedom at each node represents the axial, transverse, and rotational deformations.

$$E_{1_{GA}} = E\alpha^3 \frac{\cos(\theta)}{(\beta + \sin\theta)\sin^2\theta} \tag{4}$$

$$E_{2_{GA}} = E\alpha^3 \frac{(\beta + \sin\theta)}{\cos^3\theta} \tag{5}$$

$$v_{12_{GA}} = \frac{\cos^2\theta}{(\beta + \sin\theta)\sin\theta} \tag{6}$$

$$v_{21_{GA}} = \frac{(\beta + \sin\theta)\sin\theta}{\cos^2\theta} \tag{7}$$

$$G_{12_{GA}} = E\alpha^3 \frac{(\beta + \sin\theta)}{\beta^2(1 + 2\beta)\cos\theta} \tag{8}$$

The representation of the symbols in the Gibson and Ashby expressions above are as follows:

- E – Elastic Modulus of the base material
- θ – Cell angle as shown in fig. 1(b)

- α and β – Geometric non-dimensional ratios given by eq. (9 - 10)

$$\alpha = \frac{t}{l}\ (thickness\ ratio) \tag{9}$$

$$\beta = \frac{h}{l}\ (height\ ratio) \tag{10}$$

The main focal point of this paper is to analyse the elastic behaviour of 2D lattices when subjected to in-plane stresses. Using the top-down approach, the way in which the three structures shown in fig. (1), fig. 1(b) and fig. 1(c) work together to be analysed are explained as follows. In general, a non-linear relationship is to be expected. This can be seen in the elastic constants which are dependent on the applied stress as in eq. (3). When a cellular material is subjected to external stresses as illustrated in fig 1. (a), it results in forces and moments shown in fig. 1(b). Using the coefficients of the stiffness matrix of the beam element shown in fig. 1(c), the deformation of the unit cell when subjected to an applied stress can be obtained.

$$E_1(\mu) = \frac{K_{55}(\mu)\cos(\theta)}{b(\beta + \sin\theta)\sin^2\theta\left(1 + \cot^2\theta\frac{K_{55}(\mu)}{K_{44}(\mu)}\right)} \tag{11}$$

$$E_2(\mu) = \frac{K_{55}(\mu)(\beta + \sin\theta)}{bcos^3\theta\left(1 + \tan^2\theta\frac{K_{55}(\mu)}{K_{44}(\mu)} + 2\sec^2\theta\frac{K_{55}(\mu)}{K_{44}^{(h)}(\mu)}\right)} \tag{12}$$

$$v_{12}(\mu) = \frac{\cos^2\theta\left(1 - \frac{K_{55}(\mu)}{K_{44}(\mu)}\right)}{(\beta + \sin\theta)\sin\theta\left(1 + \cot^2\theta\frac{K_{55}(\mu)}{K_{44}(\mu)}\right)} \tag{13}$$

$$v_{21}(\mu) = \frac{(\beta + \sin\theta)\sin\theta\left(1 - \frac{K_{55}(\mu)}{K_{44}(\mu)}\right)}{\cos^2\theta\left(1 + \tan^2\theta\frac{K_{55}(\mu)}{K_{44}(\mu)} + 2\sec^2\theta\frac{K_{55}(\mu)}{K_{44}^{(h)}(\mu)}\right)} \tag{14}$$

$$G_{12}(\mu) = \frac{(\beta + \sin\theta)}{bcos\theta} = \frac{1}{\left(-\frac{h^2}{slK_{65}(\mu)} + \frac{4K_{66}^{\left(\frac{h}{2}\right)}(\mu)}{\left(K_{55}^{\left(\frac{h}{2}\right)}(\mu)K_{66}^{\left(\frac{h}{2}\right)}(\mu) - \left(K_{56}^{\left(\frac{h}{2}\right)}(\mu)\right)^2\right)} + \frac{(cos\theta + (\beta + \sin\theta)tan\theta)^2}{K_{44}(\mu)}\right)} \tag{15}$$

The representation of each symbol in eq. (11 – 15) are as follows:

- b – depth of the lattice

- K_{ij} – ij-th element of the stiffness matrix of the beam element shown in Fig. 1(c)

- μ – External stress parameter in which the stiffness coefficients have been made in the function of

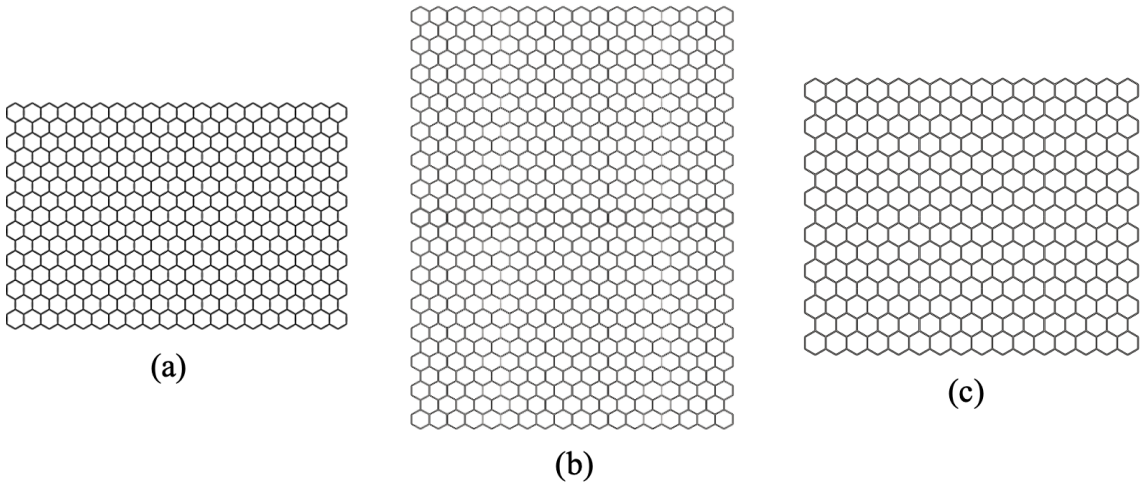

Fig. 2(a) Lattice model for the obtainment of E_1
Fig. 2(b) Lattice model for the obtainment of E_2
Fig. 2(c) Lattice model for the obtainment of G_{12}

It is important to note that to obtain values E_1, E_2 and G_{12}, different models must be simulated. For E_1, the number of cells must be greater in the x-axis whilst for E_2, there must be more cells in the y-axis. And for G_{12}, the model must be square and thus equal cells in both axes. This paper focuses on the first model in fig. 2(a) and therefore the obtainment of E_1.

2.3 Stiffness matrices of axially loaded beams

2.3.1 The classical beam element

When analysing the beam element, it is important to consider the magnitude of the forces applied to the hexagonal lattice structure as a whole. When the lattice is subjected to a compressive or tensile stress, the beam members would also experience compression or tension in the same manner. If the axial forces applied were miniscule, the deformation, whether it be compression or tension, would not have a significant impact on the bending of the beam. However, if the applied force was on a larger scale, the deformation experienced cannot be

ignored. The Euler-Bernoulli theory is used to characterise the underlying deformation undergone by the beams.

A beam with a compressive force, N, is shown in fig. (2).

Fig. (3) A Euler-Bernoulli beam subjected to an axial force, N.

From this diagram shown in fig. (3), the transverse deflection can then be derived giving the following fourth-order ordinary differential equation:

$$EI\frac{d^4W(x)}{dx^4} + N\frac{d^2W(s)}{dx^2} = F(x) \tag{16}$$

The representation of the symbols in eq. (16) are as follows:

- *W(x)* – Transverse Displacement
- *F(x)* – Applied Transverse force acting on the beam
- *E* – Young's Modulus of the beam material
- *I* – Inertia Moment of the beam cross-section
- *EI* – Bending stiffness of the beam

As shown in fig. (3), the beam element has two nodes on each end and four degrees of freedom. The displacement field within the element is expressed by cubic shape functions [25] for the classical finite element analysis and they are given by

$$\boldsymbol{N}(\xi) = [2\xi^3 - 3\xi^2 + 1, L\xi(\xi-1)^2, -2\xi^3 + 3\xi^2, L\xi^2(\xi-1)]^T \tag{17}$$

In eq. (17), the non-dimensional length variable is expressed as

$$\xi = x/L \tag{18}$$

It should be noted that these shape functions are not explicitly derived from the exact solution of the governing differential equation that is eq. (16) with relevant boundary conditions. The

stiffness matrix of the general beam element can be obtained by using these shape functions in accordance with the traditional variational formulation [25]. This is expressed as

$$\begin{aligned}\boldsymbol{K} &= EI\int_0^L \frac{d^2\boldsymbol{N}(x)}{dx^2}\frac{d^2\boldsymbol{N}^T(x)}{dx^2}dx - N\int_0^L \frac{d\boldsymbol{N}(x)}{dx}\frac{d\boldsymbol{N}^T(x)}{dx}dx \\ &= \frac{EI}{L^3}\int_0^1 \frac{d^2\boldsymbol{N}(\xi)}{d\xi^2}\frac{d^2\boldsymbol{N}^T(\xi)}{d\xi^2}d\xi - \frac{N}{L}\int_0^1 \frac{d\boldsymbol{N}(\xi)}{d\xi}\frac{d\boldsymbol{N}^T(\xi)}{d\xi}d\xi \\ &= \frac{EI}{L^3}\int_0^1 \left(\frac{d^2\boldsymbol{N}(\xi)}{d\xi^2}\frac{d^2\boldsymbol{N}^T(\xi)}{d\xi^2} - \mu^2\frac{d\boldsymbol{N}(\xi)}{d\xi}\frac{d\boldsymbol{N}^T(\xi)}{d\xi}\right)d\xi\end{aligned} \tag{19}$$

In eq. (19), the non-dimensional axial force is given by

$$\mu^2 = \frac{NL^2}{EI} \tag{20}$$

Expanding and simplifying the integral in eq. (19), the classical stiffness matrix of a beam element corresponding to fig. (3) is obtained as

$$\boldsymbol{K} = \frac{EI}{L^3}\begin{bmatrix} d_1 & d_2L & -d_1 & d_2L \\ & d_3L^2 & -d_2L & d_4L^2 \\ & & d_1 & -d_2L \\ sym & & & d_3L^2 \end{bmatrix} \tag{21}$$

The representation of each symbol in eq. (21) is as follows:

- $d_1 = 12 - \frac{6}{5}\mu^2$
- $d_2 = 6 - \frac{1}{10}\mu^2$
- $d_3 = 4 - \frac{2}{15}\mu^2$
- $d_4 = 2 + \frac{1}{30}\mu^2$ (22)

But if the axial forces were in tension, these equations would also be valid, but the signs would change as follows:

- $d_1 = 12 + \frac{6}{5}\mu^2$
- $d_2 = 6 + \frac{1}{10}\mu^2$
- $d_3 = 4 + \frac{2}{15}\mu^2$

(23)

- $d_4 = 2 - \frac{1}{30}\mu^2$

If $\mu = 0$, this implies there is no axial force applied, eq. (21) can be therefore simplified and reduced to the conventional stiffness matrix of Euler-Bernoulli beams as

$$\boldsymbol{K}_{EB} = \boldsymbol{K}_{(\mu=0)} = \frac{EI}{L^3}\begin{bmatrix} 12 & 6L & -12 & 6L \\ 6L & 4L^2 & -6L & 2L^2 \\ -12 & -6L & 12 & -6L^2 \\ 6L & 2L^2 & -6L & 4L^2 \end{bmatrix} \tag{24}$$

Since the integral in eq. (19) is evaluated precisely when deriving the stiffness matrix, the error when using this matrix in the sense of the finite element analysis stems from the assumption that the displacement field within the beam is not perfectly expressed by the cubic polynomials used in the shape function in eq. (17). Therefore, when solving practical problems, the required number of elements is increased. This could potentially be appropriate in a numerical approach, but the exact stiffness matrix of the beam elements is necessary to obtain the closed-form analytical expressions of the equivalent elastic properties.

2.3.2 Beams subjected to a compressive force

In comparison to the previous example, if the stiffness matrix is derived using the exact displacement field, only 'one' element is required for an entire beam. This will allow the obtainment of the exact expressions for the elasticity constants of the lattice material. Using eq. (16), by transforming the non-dimensional coordinate ξ the following is obtained

$$\frac{\mathrm{d}^4\omega(\xi)}{\mathrm{d}\xi^4} + \mu^2\frac{\mathrm{d}^2\omega(\xi)}{\mathrm{d}\xi^2} = 0 \tag{25}$$

In eq. (25), $\omega(\xi) = W(x)$ and the subjected force is absent. Assuming a solution of the form

$$\omega(\xi) = \exp\left[\lambda\xi\right] \tag{26}$$

and substituting eq. (26) into eq. (25) results in the expression below

$$\lambda^4 + \mu^2\lambda^2 = 0 \quad or \quad \lambda^2(1+\mu^2) = 0 \tag{27}$$

Solving eq. (27) gives four solutions

$$\lambda^2 = 0, \lambda = \pm i\mu \quad or \quad \lambda_{1,2,3,4} = 0,0,\pm i\mu \tag{28}$$

Using these solutions, the vector of basis functions can be obtained as

(29)

$$s^T(\xi) = \left\{e^{(0,0,\pm i\mu)\xi}\right\} = \{1, \xi, \sin\mu\xi\,, \cos\mu\xi\}$$

The general solution can then be expressed as

$$\omega(\xi) = \mathrm{s}^{\mathrm{T}}(\xi)\mathbf{c} \tag{30}$$

Here, the vector of unknown constants is given by

$$\mathbf{c} = \{c_1, c_2, c_3, c_4\}^T \tag{31}$$

Using eq. (30) which is made of displacement functions, the vector of shape functions is expressed as

$$\boldsymbol{N}(\xi) = \begin{Bmatrix} N_1(\xi) \\ N_2(\xi) \\ N_3(\xi) \\ N_4(\xi) \end{Bmatrix} = \begin{bmatrix} \boldsymbol{c}_1^T \\ \boldsymbol{c}_2^T \\ \boldsymbol{c}_3^T \\ \boldsymbol{c}_4^T \end{bmatrix} \mathrm{s}(\xi) \tag{32}$$

The vector of constants, allowing the existence of the jth shape function, is c_j. The boundary conditions that characterise the form functions are required to achieve these unknown constants. Table 1 depicts the relationship between shape functions and boundary conditions, where boundary conditions in each column give rise to the subsequent shape function. When solving eq. (30) for the four sets of boundary conditions mentioned above, one obtains

$$\boldsymbol{A}[\mathbf{c}_1, \mathbf{c}_2, \mathbf{c}_3, \mathbf{c}_4] = \mathbf{I}$$

	$N_1(\xi)$	$N_2(\xi)$	$N_3(\xi)$	$N_4(\xi)$
$W(0) = \omega(0)$	1	0	0	0
$\Theta(0) = \omega'(0)/L$	0	1	0	0
$W(L) = \omega(1)$	0	0	1	0
$\Theta(L) = \omega'(1)/L$	0	0	0	1

(33)

Table (1) The correlation between the boundary conditions and shape functions

Table (1) depicts a 4 x 4 identity matrix, and the matrix A is identified as

$$\boldsymbol{A}\begin{bmatrix} s^T(0) \\ \frac{1}{L}s'^T(0) \\ s^T(1) \\ \frac{1}{L}s'^T(1) \end{bmatrix} = \begin{bmatrix} 1 & 0 & 0 & 1 \\ 0 & L^{-1} & \mu/L & 0 \\ 1 & 1 & \sin(\mu) & \cos(\mu) \\ 0 & L^{-1} & -\frac{\mu\cos(\mu)}{L} & -\frac{\mu\sin(\mu)}{L} \end{bmatrix} \tag{34}$$

By solving eq. (33) for the unknown constants and substituting into eq. (32), the exact shape function can be obtained as

$$\boldsymbol{N}(\xi) = [\boldsymbol{A}^{-1}]^T s(\xi) = \tag{35}$$

$$\begin{bmatrix} \frac{\mu\cos(\mu)-\sin(\mu)+\mu}{\mu\cos(\mu)-2\sin(\mu)+\mu} & -\frac{\mu\sin(\mu)}{\mu\sin(\mu)+2\cos(\mu)-2} & \frac{\sin(\mu)}{\mu\sin(\mu)+2\cos(\mu)-2} & -\frac{\sin(\mu)}{\mu\cos(\mu)-2\sin(\mu)+\mu} \\ -\frac{L(\mu\cos(\mu)-\sin(\mu))}{\mu(\mu\sin(\mu)+2\cos(\mu)-2)} & -\frac{L\sin(\mu)}{\mu\cos(\mu)-2\sin(\mu)+\mu} & \frac{L(-\sin(\mu)+\mu(\cos(\mu)+1))}{\mu(-2\mu\sin(\mu)+\mu(\cos(\mu)+1))} & \frac{L(\mu\cos(\mu)-\sin(\mu))}{\mu(\mu\sin(\mu)+2\cos(\mu)-2)} \\ -\frac{\sin(\mu)}{\mu\cos(\mu)-2\sin(\mu)+\mu} & \frac{\mu\sin(\mu)}{\mu\sin(\mu)+2\cos(\mu)-2} & -\frac{\sin(\mu)}{\mu\sin(\mu)+2\cos(\mu)-2} & \frac{\sin(\mu)}{\mu\cos(\mu)-2\sin(\mu)+\mu} \\ \frac{L(\mu-\sin(\mu))}{\mu(\mu\sin(\mu)+2\cos(\mu)-2)} & -\frac{L\sin(\mu)}{\mu\cos(\mu)+2\sin(\mu)+\mu} & \frac{L\sin(\mu)}{\mu(\mu\cos(\mu)-2\sin(\mu)+\mu)} & \frac{L(\sin(\mu)-\mu)}{\mu(\mu\sin(\mu)+2\cos(\mu)-2)} \end{bmatrix} \begin{Bmatrix} 1 \\ \xi \\ \sin(\mu\xi) \\ \cos(\mu\xi) \end{Bmatrix} \tag{36}$$

Through substitution of the exact shape functions in the integral expression of the stiffness matrix in eq. (19) and simplification, the following expression is obtained

$$\begin{aligned} \boldsymbol{K} &= \frac{EI}{L^3}\boldsymbol{A}^{-1^T}\left\{\int_0^1 \left(\frac{d^2s(\xi)}{d\xi^2}\frac{d^2s^T(\xi)}{d\xi^2} - \mu^2\frac{ds(\xi)}{d\xi}\frac{ds^T(\xi)}{d\xi}\right)d\xi\right\}\boldsymbol{A}^{-1} \\ &= \frac{EI}{L^3}\begin{bmatrix} d_1 & d_2L & -d_1 & d_2L \\ & d_3L^2 & -d_2L & d_4L^2 \\ & & d_1 & -d_2L \\ sym & & & d_3L^2 \end{bmatrix} \end{aligned} \tag{37}$$

The non-dimensional coefficients in the above equation are given by:

- $d_1 = -\frac{\mu^3\sin(\mu)}{\Delta}$
- $d_2 = -\frac{\mu^2(\cos(\mu)-1)}{\Delta}$
- $d_3 = -\frac{\mu(\mu\cos(\mu)-\sin(\mu))}{\Delta}$
- $d_4 = -\frac{\mu(\sin(\mu)-\mu)}{\Delta}$
- $\Delta = \mu\sin(\mu) + 2\cos(\mu) - 2$

(38)

The four unique non-dimensional coefficients are solely functions of the axial force parameter, μ .Using expansion and the Taylor series about $\mu = 0$, the following are obtained:

- $d_1 = 12 - \frac{6}{5}\mu^2 - \frac{1}{700}\mu^4 - \frac{1}{63000}\mu^6 - \frac{37}{194040000}\mu^8 - \frac{59}{25225200000}\mu^{10} + O(\mu^{12})$
- $d_2 = 6 - \frac{1}{10}\mu^2 - \frac{1}{1400}\mu^4 - \frac{1}{126000}\mu^6 - \frac{37}{388080000}\mu^8 - \frac{59}{50450400000}\mu^{10} + O(\mu^{12})$

- $d_3 = 4 - \frac{2}{5}\,\mu^2 - \frac{11}{6300}\mu^4 - \frac{1}{270000}\mu^6 - \frac{509}{582120000}\mu^8 - \frac{14617}{681080400000}\mu^{10} + O(\mu^{12})$
- $d_4 = 2 + \frac{1}{3-}\,\mu^2 - \frac{13}{12600}\mu^4 - \frac{11}{3780000}\mu^6 - \frac{907}{1164240000}\mu^8 - \frac{27641}{1362160800000}\mu^{10} + O(\mu^{12})$

(39)

Using only the first term in the above expansion, it confirms that the stiffness matrix in eq. (37) reduced to the classical stiffness matrix of the Euler- Bernoulli beam [25] given in eq. (24). If the second term of this expansion is considered, the classical tangent stiffness matrix of Euler-Bernoulli beams is obtained, as seen in eq. (22). As a result, the higher-order terms, quantify the enlarged impact of the axial force on the transverse deflection of the beam.

2.3.3 Beams subjected to a tensile force

When the beam is subjected to a tensile force, the equation for the deflection in the transverse direction of the beam can be expressed in the non-dimensional coordinate ξ as

$$\frac{\mathrm{d}^4\omega(\xi)}{\mathrm{d}\xi^4} - \mu^2\frac{\mathrm{d}^2\omega(\xi)}{\mathrm{d}\xi^2} = 0 \tag{40}$$

Similarly, to the preceding case, a solution of the form $w(\xi) = \exp[\lambda\xi]$. Substituting this into eq. (40), the following equation is obtained

$$\lambda^4 - \mu^2\lambda^2 = 0 \quad or \quad \lambda^2(1-\mu^2) = 0 \tag{41}$$

Solving eq. (41) gives four solutions

$$\lambda^2 = 0, \lambda = \pm\mu \quad or \quad \lambda_{1,2,3,4} = 0{,}0 \pm \mu \tag{42}$$

Using these solutions, the vector of basis functions can be obtained as

$$s^T(\xi) = \left\{e^{(0,0,\pm i\mu)\xi}\right\} = \{1, \xi, \sinh\mu\xi\,, \cosh\mu\xi\} \tag{43}$$

By following a similar procedure to the previous compressive case, the stiffness is express by eq. (37). But instead, the four non-dimensional stiffness coefficients are now given in terms of hyperbolic functions.

- $d_1 = \frac{\mu^3\sinh(\mu)}{\Delta}$
- $d_2 = \frac{\mu^2(\cosh(\mu)-1)}{\Delta}$
- $d_3 = \frac{\mu(\mu\cosh(\mu)-\sinh(\mu))}{\Delta}$
- $d_4 = \frac{\mu(\sinh(\mu)-\mu)}{\Delta}$
- $\Delta = \mu\sinh(\mu) - 2\cosh(\mu) + 2$

(44)

Again, the four unique non-dimensional coefficients in terms of the tensile axial force parameter, μ. By using expansion and the Taylor series about $\mu = 0$, it is found that the first two terms are identical to the classical coefficients given in Eq. (23).

2.3.4 The general stiffness matrix

As stated in the previous sections of this paper, the beam element shown in fig. 1(c) is illustrated to have two nodes and three degrees of freedom per node thus totalling six degrees of freedom. This includes both axial and bending deformation which is discussed in previous subsections. The axial deformation seen in eq. (45) corresponds to degrees of freedom 1 and 4. Similarly, the bending deformation governed by eq. (16) corresponds to the displacements of the degrees of freedom 2,3,5 and 6. The equation related to axial deformation is expressed by a second-order ordinary differential equation as

$$EA\frac{\partial^2 U(x)}{\partial x^2} = F_a(b) \tag{45}$$

The representation of the symbols in Eq. (45) is as follows:

- *U(x)* – Transverse Displacement
- $F_a(x)$ – Applied transverse force acting on the beam
- *E* – Young's Modulus of the beam material
- *A* – Cross-sectional area of the beam
- *EA* – Axial Stiffness of the beam

As previously mentioned, the axial, transverse and rotational deformations are represented by the degrees of freedom of each node or in simpler terms the arrows 1-6 in Fig. (1c). The stiffness matrix of the beam element in fig. 1(c) is expressed by the 6 x 6 matrix.

$$\mathrm{K}(\mu) = \begin{bmatrix} \frac{EA}{L} & 0 & 0 & -\frac{EA}{L} & 0 & 0 \\ 0 & \frac{d_1 EI}{L^3} & \frac{d_2 EI}{L^2} & 0 & -\frac{d_1 EI}{L^3} & \frac{d_2 EI}{L^2} \\ 0 & \frac{d_2 EI}{L^2} & \frac{d_3 EI}{L} & 0 & -\frac{d_2 EI}{L^2} & \frac{d_4 EI}{L} \\ -\frac{EA}{L} & 0 & 0 & \frac{EA}{L} & 0 & 0 \\ 0 & -\frac{d_1 EI}{L^3} & -\frac{d_2 EI}{L^2} & 0 & \frac{d_1 EI}{L^3} & -\frac{d_2 EI}{L^2} \\ 0 & \frac{d_2 EI}{L^2} & \frac{d_4 EI}{L} & 0 & -\frac{d_2 EI}{L^2} & \frac{d_3 EI}{L} \end{bmatrix} \quad (46)$$

The non-dimensional coefficients (d_1, d_2, d_3 and d_4) is dependent of the direction of the force whether it is tensile or compressive. And whether it is considered with the exact beam theory as given by eqs. (22), (23), (39) and (44) or the classical theory.

The geometry of the cross-section beam is as follows: *b* is the width and *t* represents the thickness. The moment of inertia and the cross-sectional area are given by

$$I = \frac{1}{12} bt^3 \quad (47)$$

$$and\ A = bt \quad (48)$$

An error measure is introduced to understand the errors that are given by the classical finite element stiffness matrix. The error norm below is defined for a given stiffness coefficient.

$$\varepsilon_k = 100 \times \frac{d_{kclassical} - d_k}{d_{kEB}}, \quad k = 1,2 \ldots 4 \quad (49)$$

In eq. (49), d_{kEB} represents the stiffness coefficients that originated from the conventional Euler-Bernoulli beam equation in eq. (24). Fig. (4) illustrates the errors for the four unique coefficients for various non-dimensional axial force magnitudes, μ, specifically for compressive and tensile forces. It is important to be aware of the behavioural difference of errors for the two cases. It is evident in fig. (4) that the error is larger when the force is compressive in comparison to the tensile force error. As the compressive axial force increases, the error increases proportionally up to 10%. Nevertheless, the coefficient, d_1, experiences an error of less than 2%. This is important to note as it's the most crucial equivalent elastic property.

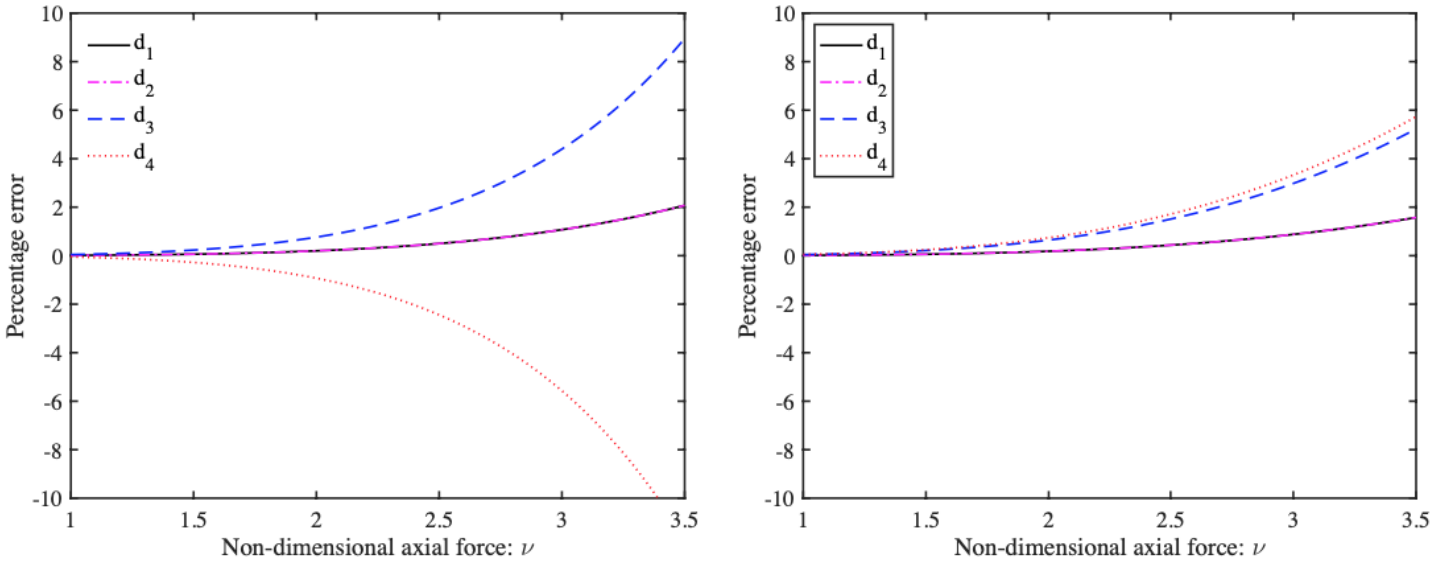

Fig. (4) In contrast to the exact transcendental stiffness coefficients as functions of the non-dimensional axial force, errors in the four special stiffness coefficients obtained using the classical method.

2.4 Lattices under compressive stress

With the purpose of obtaining the necessary properties such as $E_1(\mu)$, $E_2(\mu)$, $v_{12}(\mu)$ and $v_{21}(\mu)$, the two coefficients from the 6x6 element stiffness matrix of the inclined member and another coefficient from the other 6x6 element stiffness matrix of the vertical member are required. These are K_{55}, K_{44} and $K_{44}^{(h)}$, and can obtained from the unit-cell derivations in subsection 2.2.

The element stiffness matrix in eq. (46) provides the respective coefficients. Eqs. (47) and (48), equations for moment of inertia and the cross-sectional area, can be used to derive the stiffness coefficients as

$$K_{55}(\mu) = \frac{d_1 EI}{l^3} = Eb\alpha^3 \frac{d_1}{12}, K_{44} = \frac{EA}{l} = Eb\alpha \quad and \quad K_{44}^{(h)} = \frac{EA}{h} = \frac{Ebt}{h} = \frac{Eb\alpha}{\beta} \tag{50}$$

From eq. (50), the Poisson's ratios can be obtained

$$\frac{K_{55}(\mu)}{K_{44}} = \alpha^2 \frac{d_1}{12} \quad and \quad \frac{K_{55}(\mu)}{K_{44}^{(h)}} = \alpha^2 \beta \frac{d_1}{12} \tag{51}$$

Then, by substituting eqs. (50) an (51) into eqs. (11) – (14). The general expressions can be obtained

$$E_1(\mu) = \frac{E\alpha^3 \cos\theta}{(\beta + sin\theta)\left(12\sin^2\frac{\theta}{d_1} + \alpha^2\cos^2\theta\right)} \tag{52}$$

$$E_2(\mu) = \frac{E\alpha^3(\beta + \sin\theta)}{\left(\frac{12}{d_1} - \alpha^2\right)\cos^3\theta + \alpha^2(2\beta + 1)\cos\theta} \tag{53}$$

$$v_{12}(\mu) = \frac{\cos^2\theta\left(\frac{12}{d_1} - \alpha^2\right)}{(\beta + sin\theta)sin\theta(12/d_1 + \alpha^2\cot^2\theta)} \tag{54}$$

$$v_{21}(\mu) = \frac{(\beta + sin\theta)sin\theta\left(\frac{12}{d_1} - \alpha^2\right)}{\left(\frac{12}{d_1} - \alpha^2\right)\cos^2\theta + \alpha^2(2\beta + 1)} \tag{55}$$

As a means to obtain the shear modulus, five elements are required from two different stiffness matrices. The two coefficients of the 6 x 6 element stiffness matrix of the inclined member which are K_{65}, K_{44} and three other elements from the stiffness matrix of the vertical with half the length. (The supplementary paper provided will give further details on this). There is no axial force acting on the vertical members as there is an applied shear stress present. Thus, in eq. (15), the only term affected by the axial stress in the expression of the shear modulus is K_{65}. This coefficient corresponds to the segments/members of the unit cell which are inclined. Thus, the following expression is acquired

$$K_{65}(\mu) = -d_2 \frac{EI}{l^2} = -d_2 \frac{Ebt^3}{12l^2} \tag{56}$$

The three elements of the stiffness matrix of the vertical member with half the length is required. This is given by

$$K_{55}^{(h/2)} = \frac{12EI}{\left(\frac{h}{2}\right)^3} = \frac{8Ebt^3}{h^3}, \quad K_{56}^{(h/2)} = -\frac{6EI}{\left(\frac{h}{2}\right)^2} = -\frac{2Ebt^3}{h^2}, \quad K_{66}^{(h/2)} = \frac{4EI}{\frac{h}{2}} = \frac{2Ebt^3}{3h} \tag{57}$$

Using the above equations, the expression below can be obtained

$$G_{12}(\mu) = \frac{\beta+sin\theta}{bcos\theta} \frac{1}{\left(-\frac{h^2}{2lK_{65}(\mu)} + \frac{4K_{66}^{\left(\frac{h}{2}\right)}}{\left(K_{55}^{\left(\frac{h}{2}\right)} K_{66}^{\left(\frac{h}{2}\right)} - \left(K_{56}^{\left(\frac{h}{2}\right)}\right)^2\right)}\right)} = \frac{E\alpha^3(\beta+sin\theta)}{\left(\beta^2\left(\frac{6}{d_2}+2\beta\right)+\alpha^2(cos\theta+(\beta+sin\theta)tan\theta)^2\right)cos\theta} \tag{58}$$

By taking $lim_{\mu\to 0}$ and substituting $\alpha^2 = 0$, the derivations of the equations can be simplified to corresponding classical expressions by Gibson and Ashby in eqs. (4 – 8) [24]. The stresses in two directions both separately and together are considered for this paper. Four properties are discussed: E_1, E_2, v_{12} and v_{21}. The shear modulus is not included since there is a miniscule difference, in simple terms there is a limited effect on this property.

2.4.1 Case 1 – Compressive stress in direction-1 only

Fig. (5) illustrates a compressive stress in direction- 1 acting on the hexagonal lattice configuration. The equivalent force acting on the unit cell is also shown on fig. (4).

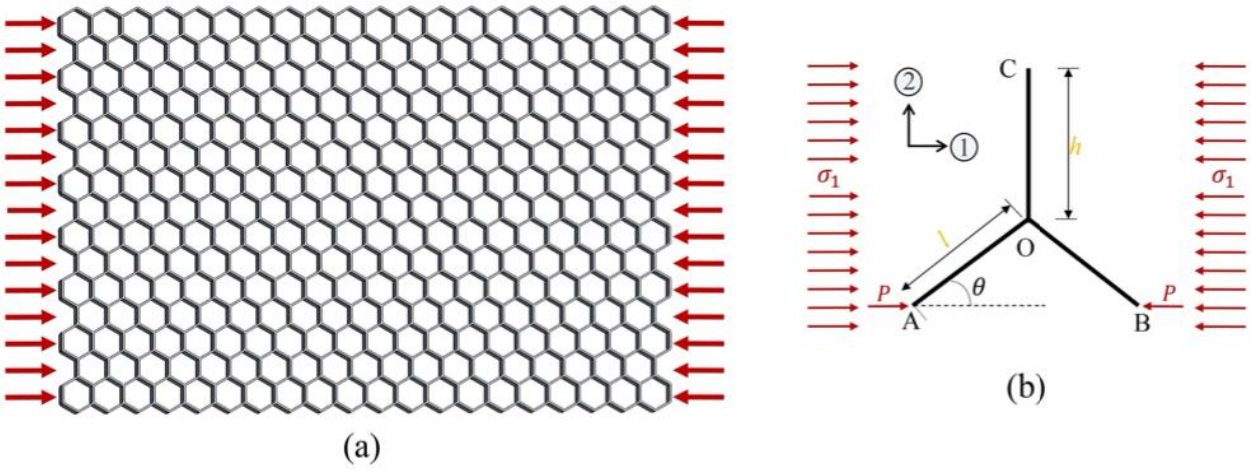

Fig. (5) (a) Hexagonal lattice structure experiencing a compressive stress in 1-direction
Fig. (5) (b) Force in the constituent beams within the unit cell model. The compressive axial force is equivalent P cos θ with P = σ1b (h + l sin θ).

The compressive axial force acting on the inclined beam elements is N = P cos θ where

$$P = \sigma_1 b(h + lsin\theta) \tag{59}$$

The symbols b and σ_1 represent the out-of-plane thickness of the lattice and applied stress respectively. From these, the non-dimensional axial force in eq. (20) can be obtained as

$$\mu^2 = \frac{Nl^2}{EI} = \frac{\sigma_1 b(h + l\sin\theta)\cos\theta\, l^2}{\frac{Ebt^3}{12}} = \left(\frac{\sigma_1}{E}\right)\frac{12(\beta + \sin\theta)}{\alpha^3}\cos\theta$$

$$or \quad \mu = \sqrt{\left(\frac{\sigma_1}{E\alpha^3}\right)12(\beta + \sin\theta)\cos\theta} \tag{60}$$

The non-dimensional coefficient, d_1 which appears in eqs. (52) – (55) can be obtained using the above expression of μ as well as using eq. (22) or eq. (38). Which equation used is solely dependent on whether the classical or exact formulation is chosen. For the classical case, the non-dimensional coefficient from eq. (22) is used to obtain the following approximate expressions

$$E_1^{(c)}(\mu) \approx \frac{E\alpha^3\cos\theta}{(\beta + \sin\theta)(10\sin^2\theta/(10 - \mu^2)\sin^2\theta + \alpha^2\cos^2\theta)} \tag{61}$$

$$E_2^{(c)}(\mu) \approx \frac{E\alpha^3(\beta + \sin\theta)}{(10/(10 - \mu^2) - \alpha^2)\cos^3\theta + \alpha^2(2\beta + 1)\cos\theta)} \tag{62}$$

$$v_{12}^{(c)}(\mu) \approx \frac{\cos^2\theta\,(10/(10 - \mu^2) - \alpha^2)}{(\beta + \sin\theta)\sin\theta\,(10/(10 - \mu^2) + \alpha^2\cot^2\theta)} \tag{63}$$

$$v_{21}^{(c)}(\mu) \approx \frac{(\beta + \sin\theta)\sin\theta\,(10/(10 - \mu^2) - \alpha^2)}{(10/(10 - \mu^2) - \alpha^2)\cos^2\theta + \alpha^2(2\beta + 1)} \tag{64}$$

The superscript $(\bullet)^{(c)}$ represents the elastic constants for the lattice when it is subjected to a compressive stress. It is clearly shown from these expressions that all four of the constants are nonlinear functions of the stress parameter, μ, which is obtained in eq. (60). On the other hand, using the non-dimensional coefficient from eq. (38), the exact expression can be attained. Substitution of the coefficient must be carried out into eqs. (52) – (55) and simplification for the exact expression of the elastic constants. Therefore, the following expressions for the constants are derived.

$$E_1^{(c)}(\mu) = \frac{E\alpha^3\mu^3 \sin(\mu)\cos\theta}{(\beta + \sin\theta)(\mu^3 \sin(\mu)\,\alpha^2 \cos^2\theta - 12\sin^2\theta\Delta)} \tag{65}$$

$$E_2^{(c)}(\mu) = \frac{E\alpha^3\mu^3 \sin(\mu)\,(\beta + \sin\theta)}{\mu^3 \sin(\mu)\,\alpha^2(2\beta + 1)\cos\theta - (\mu^3 \sin(\mu)\,\alpha^2 + 12\Delta)\cos^3\theta} \tag{66}$$

$$v_{12}^{(c)}(\mu) = \frac{\cos^2\theta\,(12\Delta + \mu^3 \sin(\mu)\,\alpha^2)}{(\beta + \sin\theta)\sin\theta\,(12\Delta - \mu^3 \sin(\mu)\,\alpha^2 \cot^2\theta)} \tag{67}$$

$$v_{21}^{(c)}(\mu) = \frac{(\beta + \sin\theta)\sin\theta\,(12\Delta + \mu^3 \sin(\mu)\,\alpha^2)}{(12\Delta + \mu^3 \sin(\mu)\,\alpha^2)\cos^2\theta - \mu^3 \sin(\mu)\,\alpha^2(2\beta + 1)} \tag{68}$$

where $\Delta = \mu \sin(\mu) + 2\cos(\mu) - 2$.

A nonlinear relationship with the applied stress is evident as a direct result of the trigonometric functions of the stress parameter μ in eq. (60) present in these expressions. Fig. (6) presents the comparison of analytical results to the direct nonlinear finite element simulation results. The graph in fig. (6) presents the normalised compressive stress, $\sigma 1/ E\alpha^3$ against an equivalent normalised modulus, $E_1/E\alpha^3$. A comparison of the exact and approximate expressions given by eq. (65) and eq. (61) is also demonstrated. The results from both expressions are almost identical with very miniscule differences. ANSYS, a commercial software, has been used for the finite element analysis. A mesh study has been executed to ensure and increase the validity and accuracy of the results obtained. For the solution, the 'large deformation' feature was turned on for the nonlinear analysis to be carried out. Although, as it can be seen, the results are not identical to the analytical expressions, the trend is somewhat similar with a percentage error within 10%. It is astonishing that simple closed-form expressions can produce a similar result to the full scale nonlinear finite element analysis for the two different geometries analysed in fig. (6). These are further discussed in subsequent sections of this paper.

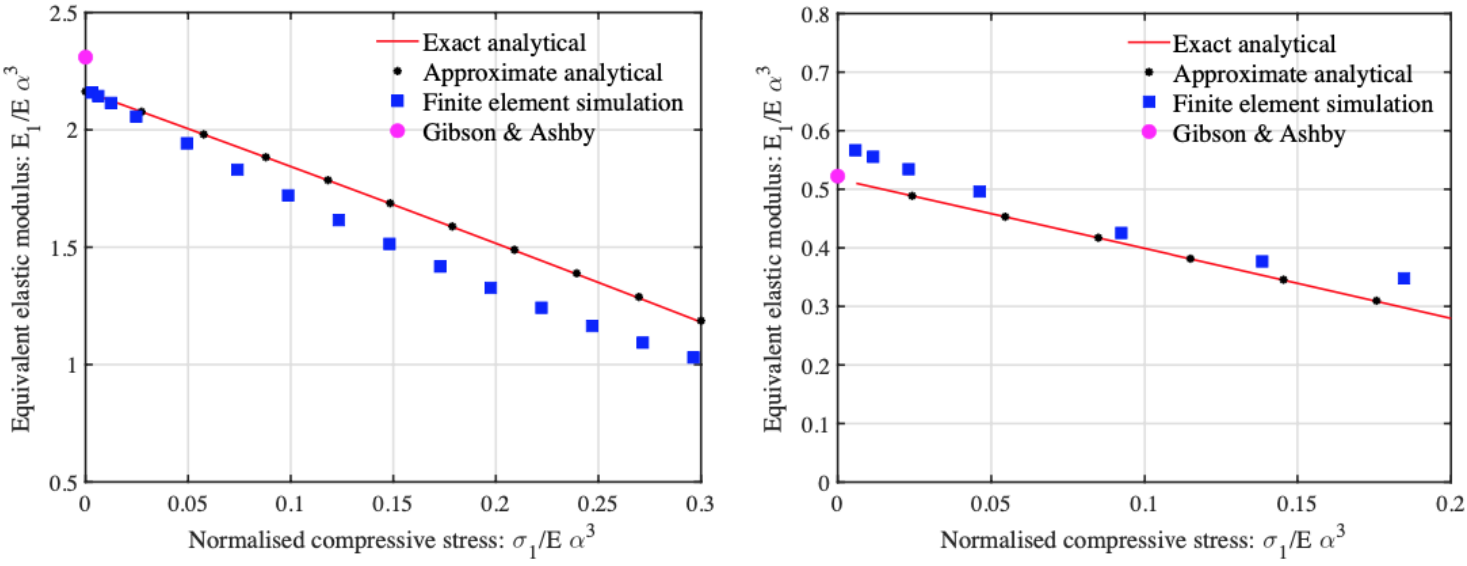

(a) $\theta = 30°$, $\alpha = t/l = 0.15$ and $\beta = h/l = 1$.

(b) $\theta = 45°$, $\alpha = t/l = 0.1$ and $\beta = h/l = 2$.

Fig. (6) Equivalent normalised Young's modulus, ($E_1/E\alpha^3$) against the normalised compressive stress ($\sigma_1/ E\alpha^3$) in direction-1 as shown in fig. (4). A comparison of the analytical expressions results, and finite element analysis results are presented. Two different hexagonal lattice geometries are analysed and considered in (a) and (b).

It can be observed in fig. (6) that as the applied compressive stress increases, the effective Young's modulus decreases significantly and further from the classical results. Fig. (7) displays contours of the Poisson's ratios of the lattice when subjected to a compressive stress in direction- 1 and its normalised effective elastic moduli. This figure should help understand the observations found in fig. (6). The effect on E_1 decreases as the cell angle increases whilst the effect increases on E_2 for all magnitudes of the compressive stress. Furthermore, the effect that the cell angle has on the Poisson's ratios is as follows; there's a decreasing effect on v_{12} whilst an increasing effect is put upon v_{21} for all values of the compressive stress. Moreover, the increasing compressive stress for all values of the cell angle, θ, causes a decrease in the elastic moduli. But this is expected as by analysing the lattice material, it can be known that the stiffness decreases due to the compressive stress which causes the lattice to experience a softening effect in direction- 1. Likewise, as the compressive stress increases, there is a slight increase in the Poisson's ratios.

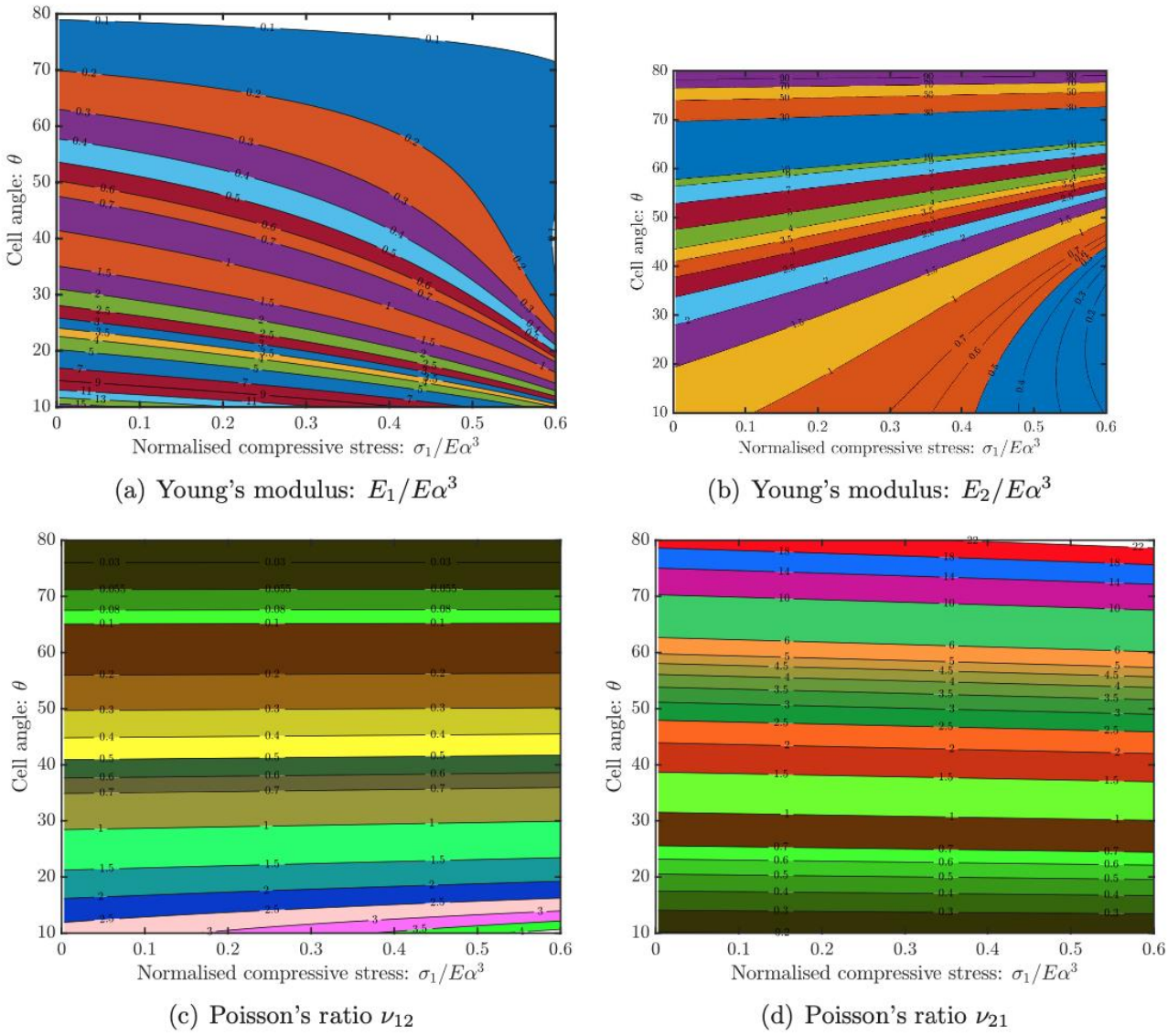

Fig. (7) Contours of the Poisson's ratios and normalised effective elastic moduli of a lattice subjected to a compressive stress in direction 1 corresponding to fig. (4). The normalised compressive stress ($\sigma_1/ E\alpha^3$) varies in the x-axis as well as the cell angle in the y-axis. The geometric dimensional ratios are $\alpha = t/l = 0.15$ and $\beta = h/l = 1$.

2.4.2 Case 2 – Compressive stress in direction-2 only

Now, the hexagonal lattice subjected to a compressive stress in direction-2 is analysed and observed in fig. (8). The equivalent force acting on the unit cell is also shown on fig. (8). The compressive axial force acting on the inclined beam elements is N = W sin θ where

$$W = \sigma_2 bl \cos\theta \tag{69}$$

The symbols b and σ_2 represent the out-of-plane thickness of the lattice and applied stress respectively. From these, the non-dimensional axial force in Eq. (20) can be obtained as

$$\mu^2 = \frac{Nl^2}{EI} = \frac{\sigma_1 bl \sin\theta \cos\theta \, l^2}{\frac{Ebt^3}{12}} = \left(\frac{\sigma_1}{E}\right)\frac{12 \sin\theta \cos\theta}{\alpha^3}$$

$$or \quad \mu = \sqrt{\left(\frac{\sigma_1}{E\alpha^3}\right) 12 \sin\theta \cos\theta} \tag{70}$$

The derivations of the expressions of the equivalent elastic constants in subsection 2.4.1 are valid with the expression of μ given in eq. (70). Fig. (9) displays contours of the Poisson's ratios of the lattice when subjected to a compressive stress in direction- 1 and its normalised effective elastic moduli. Similar to the preceding case, the effect on E_1 decreases as the cell angle increases whilst the effect increases on E_2 for all magnitudes of the compressive stress. Furthermore, the effect that the cell angle has on the Poisson's ratios is as follows; there's a decreasing effect on v_{12} whilst an increasing effect is put upon v_{21} for all values of the compressive stress. Moreover, the increasing compressive stress for all values of the cell angle, θ, causes a decrease in the elastic moduli. But this is expected as by analysing the lattice material, it can be known that the stiffness decreases due to the compressive stress which causes the lattice to experience a softening effect in direction- 1.

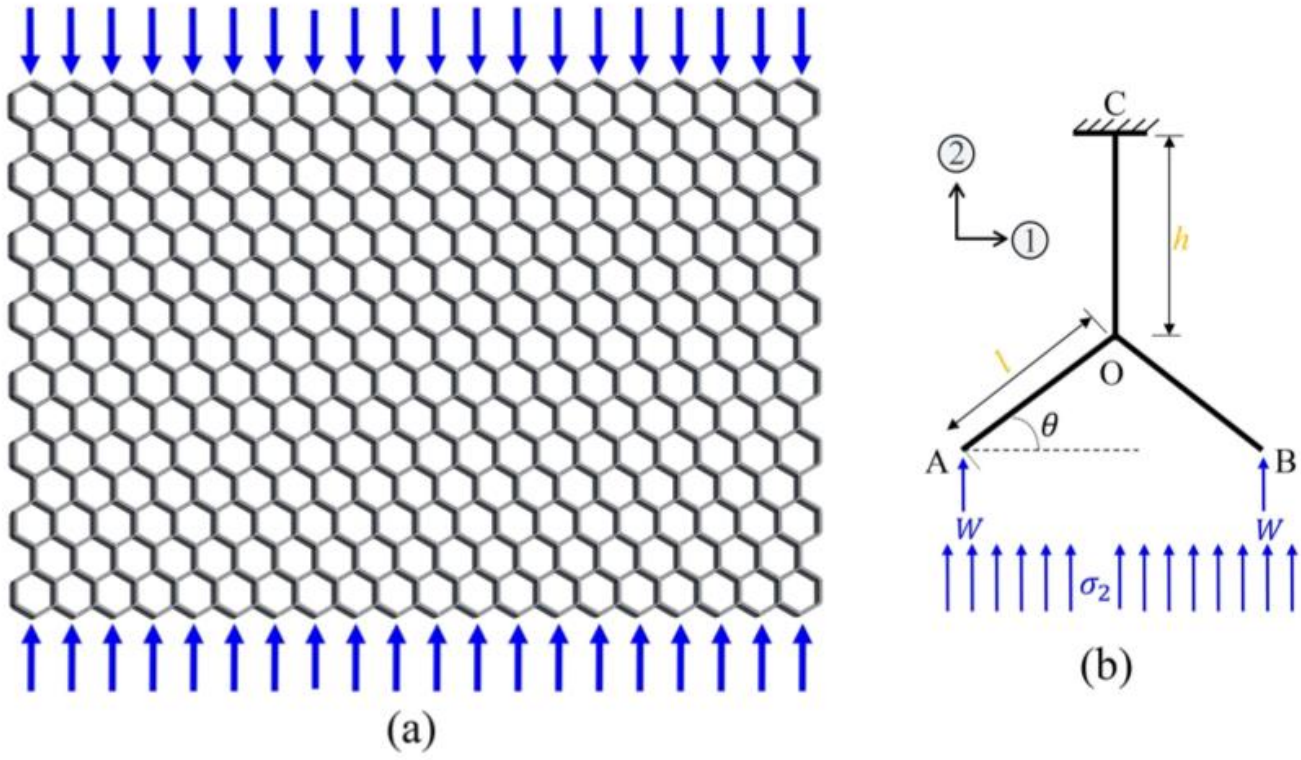

Fig. (8) (a) Hexagonal lattice structure experiencing a compressive stress in the 2-direction
Fig. (8) (b) Force in the constituent beams within the unit cell model. The compressive axial force is equivalent to Wsinθ with W = σ2blcosθ.

2.4.3 Case 3 – Compressive stresses in both directions

And finally, the hexagonal lattice subjected to both a compressive stress in direction--1 and direction- 2 is analysed and observed in fig. (10). The equivalent force acting on the unit cell is also shown on fig. (10). Since the axial force, N, within the individual beams are now functions of compressive stresses in both directions, σ1 and σ2. Using fig. 9(b), the total axial forces are

$$N = P\cos\theta + W\sin\theta = \sigma_1 b(h + l\sin\theta)\cos\theta + \sigma_2 bl\sin\theta\cos\theta \tag{71}$$

The non-dimensional axial force parameter can then be attained.

$$\mu^2 = \frac{Nl^2}{EI} = \frac{\sigma_1 b(h + l\sin\theta)\cos\theta\, l^2 + \sigma_2 bl\sin\theta\cos\theta\, l^2}{\frac{Ebt^3}{12}} \tag{72}$$

$$or \quad \mu = \sqrt{12\cos\theta\left\{\left(\frac{\sigma_1}{E\alpha^3}\right)(\beta + \sin\theta) + \left(\frac{\sigma_2}{E\alpha^3}\right)\sin\theta\right\}} \tag{73}$$

The derivations of the expressions of the equivalent elastic constants in subsection 2.4.1 are valid with the expression of μ given in eq. (72). Fig. (11) displays contours of the Poisson's ratios of the lattice when subjected to a compressive stress simultaneously in both direction- 1 and direction- 2 as well as its normalised effective elastic moduli. Both the elastic moduli are normalised by $E\alpha^3$. This normalised value decreases as the compressive stress values increase. Again, this is expected as by analysing the lattice material, it can be known that the stiffness decreases due to the compressive stress which causes the lattice to experience a softening effect in both directions.

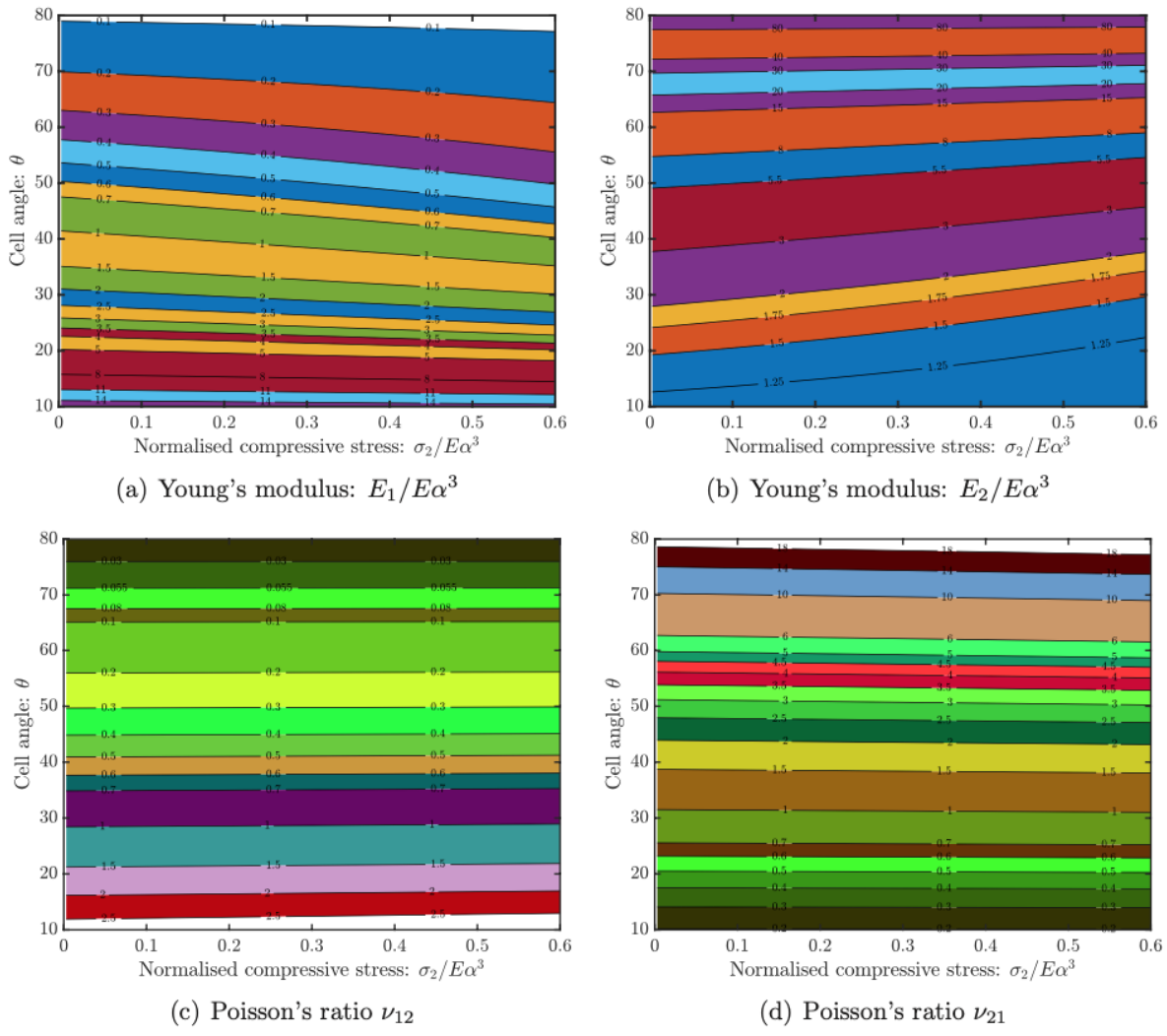

Fig. (9) Contours of the Poisson's ratios and normalised effective elastic moduli of a lattice subjected to a compressive stress in direction 2 corresponding to fig. (8). The normalised compressive stress ($\sigma_2/ E\alpha^3$) varies in the x-axis as well as the cell angle in the y-axis. The geometric dimensional ratios are $\alpha = t/l = 0.15$ and $\beta = h/l = 1$.

2.5 Lattices under tensile stress

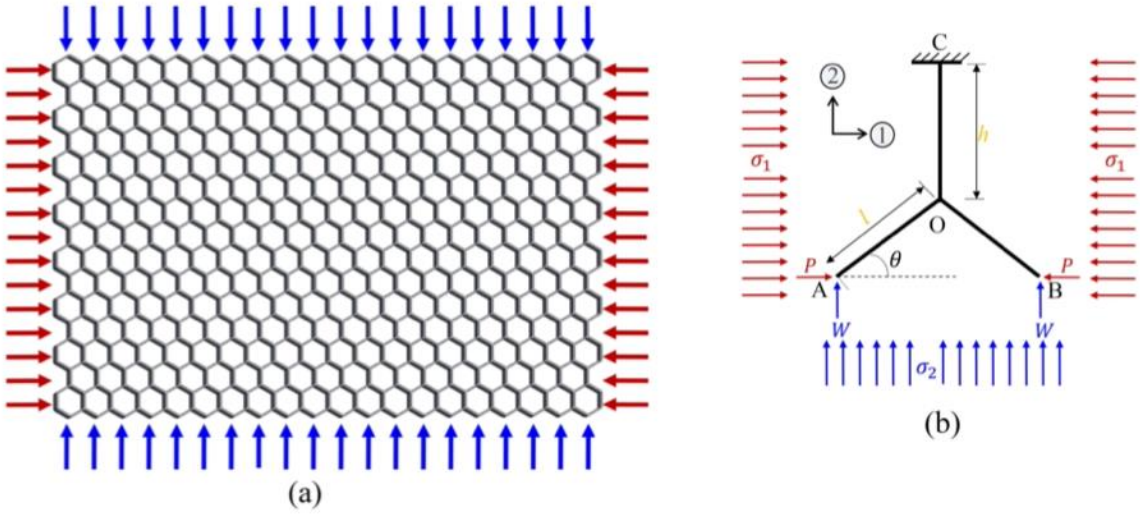

Fig. (10)(a) Hexagonal lattice structure experiencing a compressive stress in both directions 1 and 2
Fig. (10)(b) Force in the constituent beams within the unit cell model. The compressive axial force is equivalent to Pcos θ + Wsinθ with P = σ1b (h + l sin θ) and W = σ2blcosθ

The exact closed-form expressions for lattice when subjected to simultaneous compressive stresses in both directions have been derived for $E_1(\mu)$, $E_2(\mu)$, $\nu_{21}(\mu)$ and $\nu_{21}(\mu)$ in section 2.4. Eqs. (52), (53), (54) and (55) are generalised and thus has high validity when the stiffness coefficient, d1, is substituted by the tensile force case in the beam. This non-dimensional coefficient can be obtained using eq. (23) or eq. (44). Similar to the previous compressive case, which equation used is solely dependent on whether the classical or exact formulation is chosen. For the classical case, the non-dimensional coefficient from eq. (23) is used to obtain the following approximate expressions

$$E_1^{(c)}(\mu) \approx \frac{E\alpha^3 \cos\theta}{(\beta + \sin\theta)(10\sin^2\theta/(10+\mu^2)\sin^2\theta + \alpha^2\cos^2\theta)} \tag{74}$$

$$E_2^{(c)}(\mu) \approx \frac{E\alpha^3(\beta + \sin\theta)}{(10/(10+\mu^2) - \alpha^2)\cos^3\theta + \alpha^2(2\beta+1)\cos\theta)} \tag{75}$$

$$v_{12}^{(c)}(\mu) \approx \frac{\cos^2\theta\,(12/d_1 - \alpha^2)}{(\beta + \sin\theta)\sin\theta\,(10/(10+\mu^2) + \alpha^2\cot^2\theta)} \tag{76}$$

$$v_{21}^{(c)}(\mu) \approx \frac{(\beta + \sin\theta)\sin\theta\,(10/(10+\mu^2) - \alpha^2)}{(10/(10-\mu^2) - \alpha^2)\cos^2\theta + \alpha^2(2\beta+1)} \tag{77}$$

The superscript $(\bullet)^{(t)}$ represents the elastic constants for the lattice when it is subjected to a tensile stress. It is clearly shown from these expressions that all four of the constants are again nonlinear functions of the stress parameter, μ. On the other hand, using the non-dimensional coefficient from eq. (44), the exact expression can be attained. Substitution of the coefficient must be carried out into eqs. (52) – (55) and simplification for the exact expression of the elastic constants. Therefore, the following expressions for the constants are derived.

$$E_1^{(t)}(\mu) = \frac{E\alpha^3\mu^3 \sinh(\mu)\cos\theta}{(\beta+\sin\theta)(\mu^3\sinh(\mu)\,\alpha^2\cos^2\theta + 12\sin^2\theta\Delta)} \tag{78}$$

$$E_2^{(t)}(\mu) = \frac{E\alpha^3\mu^3 \sinh(\mu)\,(\beta+\sin\theta)}{\mu^3\sinh(\mu)\,\alpha^2(2\beta+1)\cos\theta + (-\mu^3\sinh(\mu)\,\alpha^2 + 12\Delta)\cos^3\theta} \tag{79}$$

$$v_{12}^{(t)}(\mu) = \frac{\cos^2\theta\,(12\Delta - \mu^3\sinh(\mu)\,\alpha^2)}{(\beta+\sin\theta)\sin\theta\,(12\Delta + \mu^3\sinh(\mu)\,\alpha^2\cot^2\theta)} \tag{80}$$

$$v_{21}^{(t)}(\mu) = \frac{(\beta+\sin\theta)\sin\theta\,(12\Delta - \mu^3\sin(\mu)\,\alpha^2)}{(12\Delta - \mu^3\sinh(\mu)\,\alpha^2)\cos^2\theta + \mu^3\sin(\mu)\,\alpha^2(2\beta+1)} \tag{81}$$

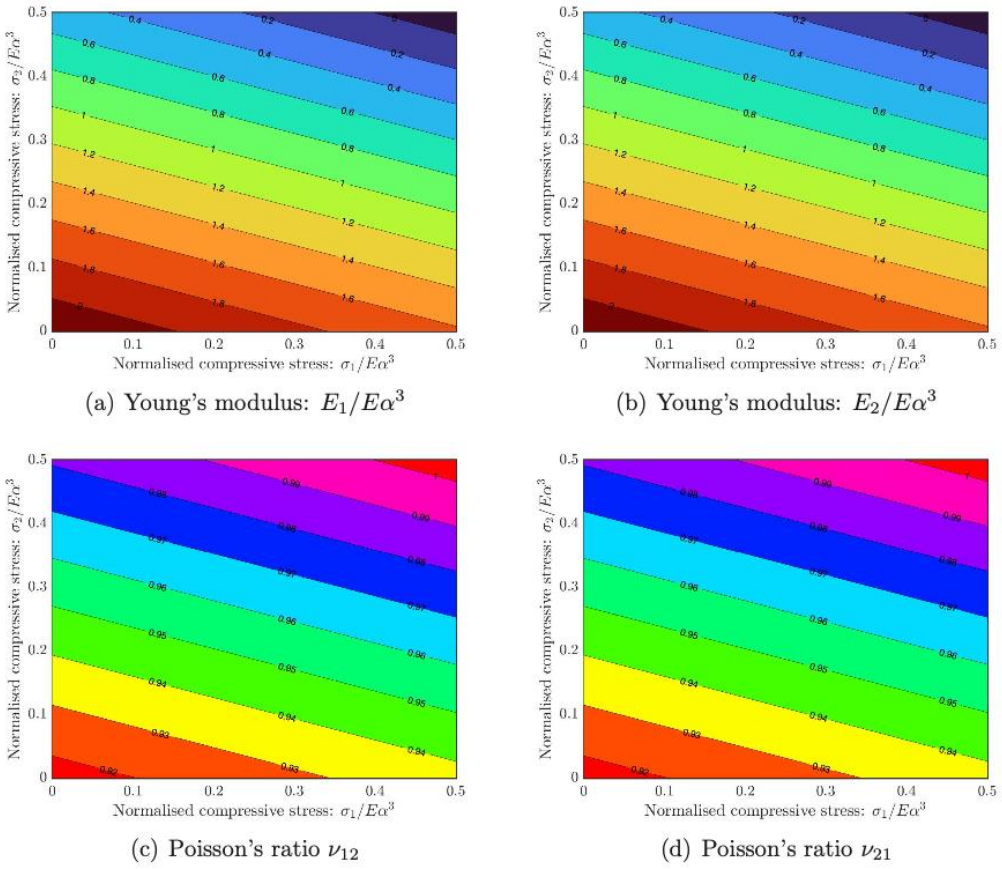

Fig. (11) Contours of the Poisson's ratios and normalised effective elastic moduli of a lattice subjected to a compressive stress in directions 1 and 2 corresponding to fig. (9). The contours of a unit cell with a cell angle of 30 degrees are plotted as normalised compressive stress in both directions with α= t/l =0.15 and β = h/l =1.

where $\Delta = \mu \sinh(\mu) - 2\cosh(\mu) + 2$.

A nonlinear relationship with the applied stress is evident as a direct result of the hyperbolic functions of the stress parameter μ present in these expressions.

2.5.1 Case 4 – Tensile stress in direction-1 only

Fig. (12) illustrates a compressive stress in direction- 1 acting on the hexagonal lattice configuration. The equivalent force acting on the unit cell is also shown on fig. (12). The forces applied are equal to the previous case in subsection 2.4.1 where a compressive stress is applied. Therefore, again, the value of μ is given by eq. (60).

A comparison of analytical results to the direct nonlinear finite element simulation results are illustrated in fig. (13). The graph in fig. (13) presents the normalised compressive stress, $\sigma 1/E\alpha^3$ against an equivalent normalised modulus, $E_1/E\alpha^3$. A comparison of the exact and approximate expressions given by eq. (78) and Eq. (74) is also demonstrated. And the results from the classical expression by Gibson and Ashby in eq. (4) is also plotted. The results from both expressions are almost identical with very miniscule differences.

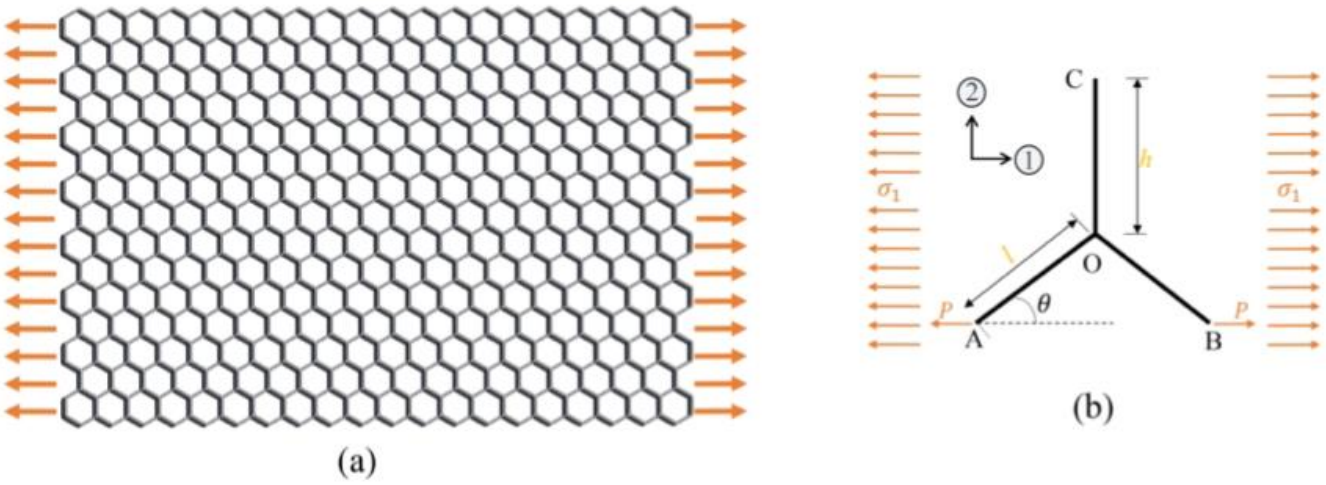

Fig. 12 (a) Hexagonal lattice structure experiencing a tensile stress in 1-direction
Fig. 12 (b) Force in the constituent beams within the unit cell model. The tensile axial force is equivalent to P cos θ with P = σ1b (h + l sin θ).

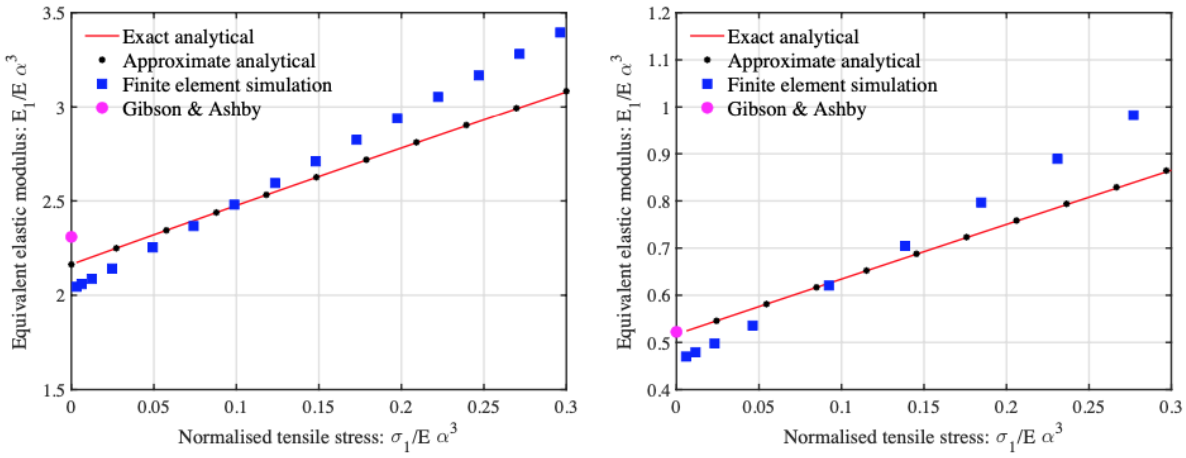

Fig. (13) Equivalent normalised Young's modulus, ($E_1/E\alpha^3$) against the normalised tensile stress ($\sigma_1/E\alpha^3$) in direction-1 as shown in fig. (11). A comparison of the analytical expressions results, and finite element analysis results are presented. Two different hexagonal lattice geometries are analysed and considered in (a) and (b).

ANSYS, a commercial software, has again been used for the finite element analysis. A mesh study has been executed to ensure and increase the validity and accuracy of the results obtained. For the solution, the 'large deformation' feature was turned on for the nonlinear analysis to be carried out. This would allow for the software to consider the stiffness changes as the geometry changes during the simulation. This feature is applied to all cases in this paper. The two lattice models considered in this case are the same as the compressive stress case discussed previously. But the difference is that the direction of stress has been changed when carrying out the finite element analysis since it is now a tensile case. Although, as it can be seen, the results are not identical to the analytical expressions, the trend is somewhat similar with a percentage error within 10%. It is astonishing that simple closed-form expressions can produce a similar result to the full scale nonlinear finite element analysis for the two different geometries analysed in fig. (13).

It can be observed in fig. (13) that as the applied tensile stress increases, the effective Young's modulus increases significantly and further from the classical results. Fig. (14) displays contours of the Poisson's ratios of the lattice when subjected to a tensile stress in direction- 1 and its normalised effective elastic moduli. This figure should help understand the observations found in fig. (13).

The effect on E_1 works similarly to the preceding case where it decreases as the cell angle increases whilst the effect increases on E_2 for all magnitudes of the tensile stress. Furthermore, the effect that the cell angle has on the Poisson's ratios is as follows; there's a decreasing effect on v_{12} whilst an increasing effect is put upon v_{21} for all values of the compressive stress. Moreover, the increasing tensile e stress for all values of the cell angle, θ, causes an increase in the elastic moduli. But this is expected as by analysing the lattice material, it can be known that the stiffness increases due to the tensile stress which causes the lattice to experience a stiffening effect in direction- 1. Likewise, as the tensile stress increases, there is a slight increase in the Poisson's ratios.

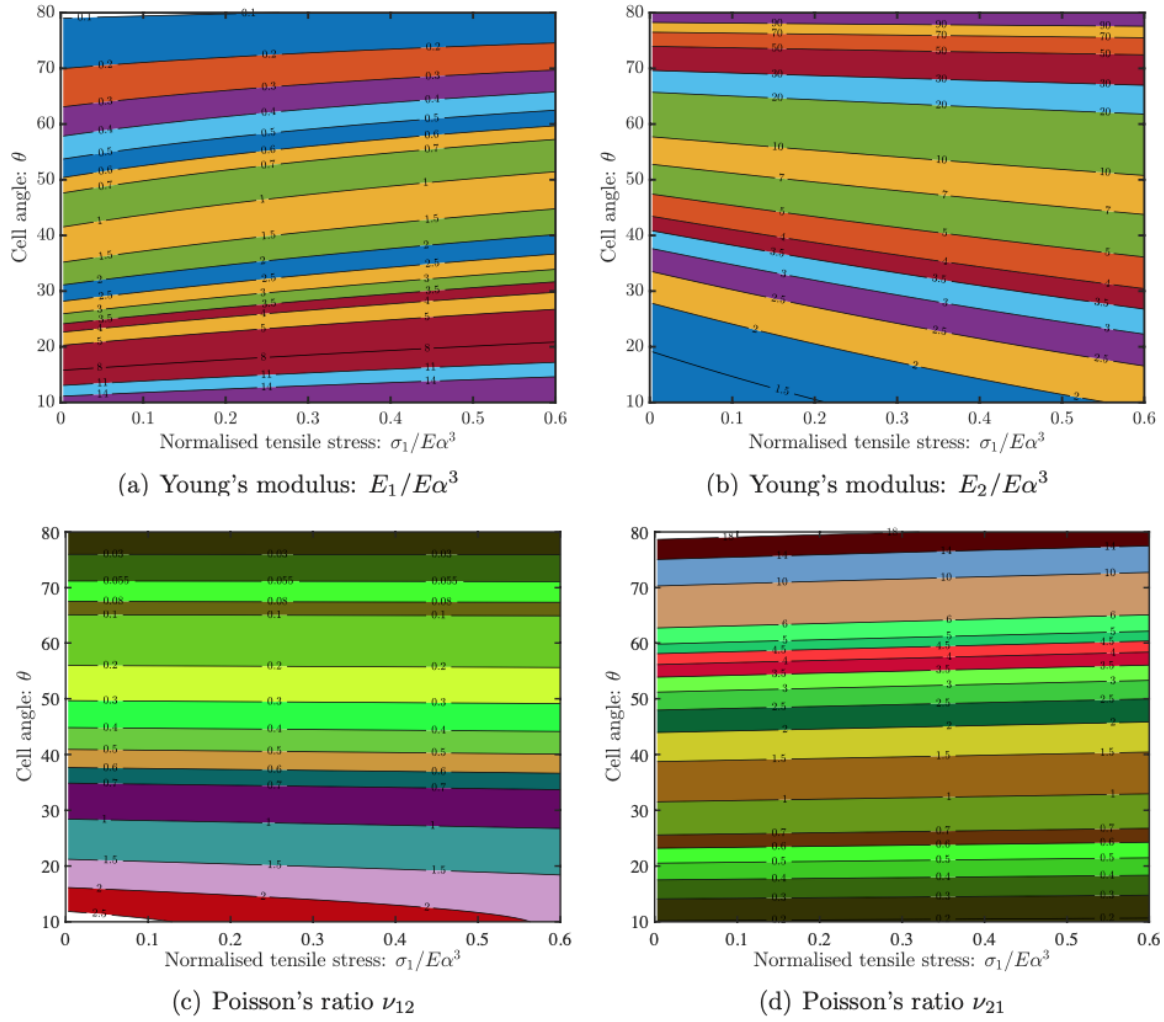

Fig. (14) Contours of the Poisson's ratios and normalised effective elastic moduli of a lattice subjected to a tensile stress in direction 1 corresponding to fig. (11). The normalised tensile stress ($\sigma_1/ E\alpha^3$) varies in the x-axis as well as the cell angle in the y-axis. The geometric dimensional ratios are $\alpha = t/l = 0.15$ and $\beta = h/l = 1$.

2.5.2 Case 5 – Tensile stress in direction-2 only

Now, the hexagonal lattice subjected to a tensile stress in direction-2 is analysed and observed in fig. (15). The equivalent force acting on the unit cell is also shown on fig. (15). The forces applied are equal to the previous case in subsection 2.4.1 where a compressive stress is applied. Therefore, again, the value of μ is given by eq. (70).

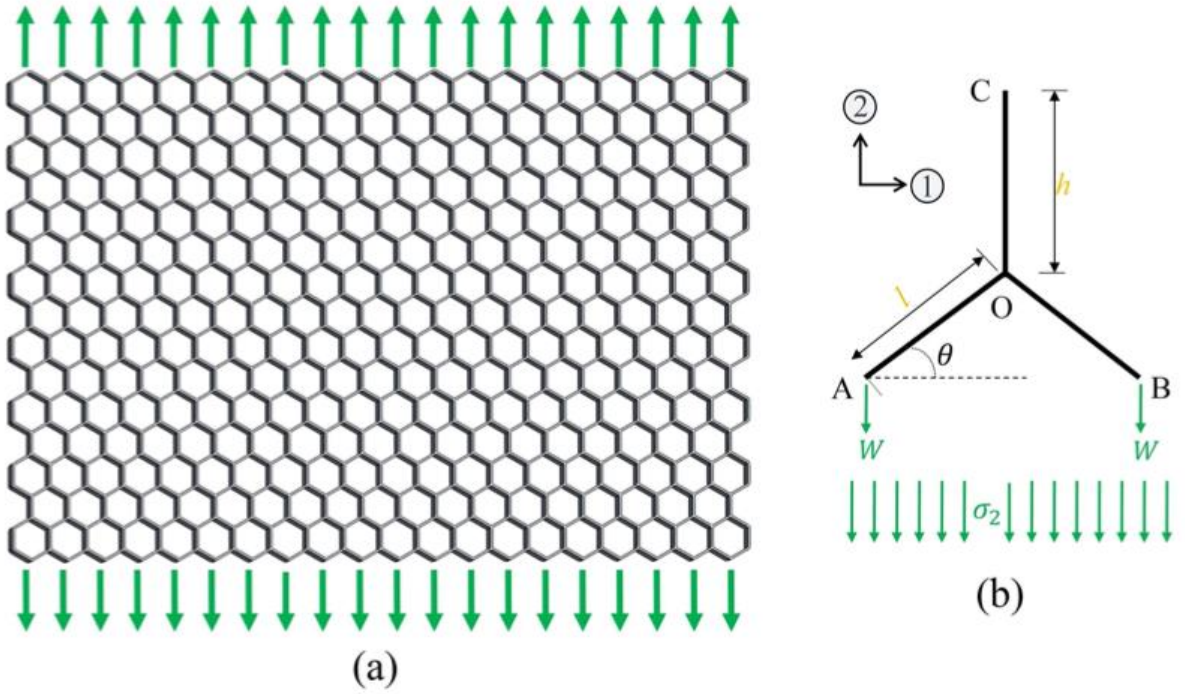

Fig. 15(a) Hexagonal lattice structure experiencing a tensile stress in the 2-direction
Fig. 15(b) Force in the constituent beams within the unit cell model. The tensile axial force is equivalent to $W\sin\theta$ with $W = \sigma_2 b l \cos\theta$.

Fig. (16) displays contours of the Poisson's ratios of the lattice when subjected to a tensile stress in direction-2 and its normalised effective elastic moduli. The effect on E_1 decreases as the cell angle increases whilst the effect increases on E_2 for all magnitudes of the tensile stress. Furthermore, the effect that the cell angle has on the Poisson's ratios is as follows; there's a decreasing effect on v_{12} whilst an increasing effect is put upon v_{21} for all values of the tensile stress. Moreover, the increasing tensile stress for all values of the cell angle, θ, causes an increase in the elastic moduli. But this is expected as by analysing the lattice material, it can be known that the stiffness increases due to the tensile stress which causes the lattice to experience a stiffening effect. Likewise, as the tensile stress increases, no significant change is seen in the Poisson's ratios.

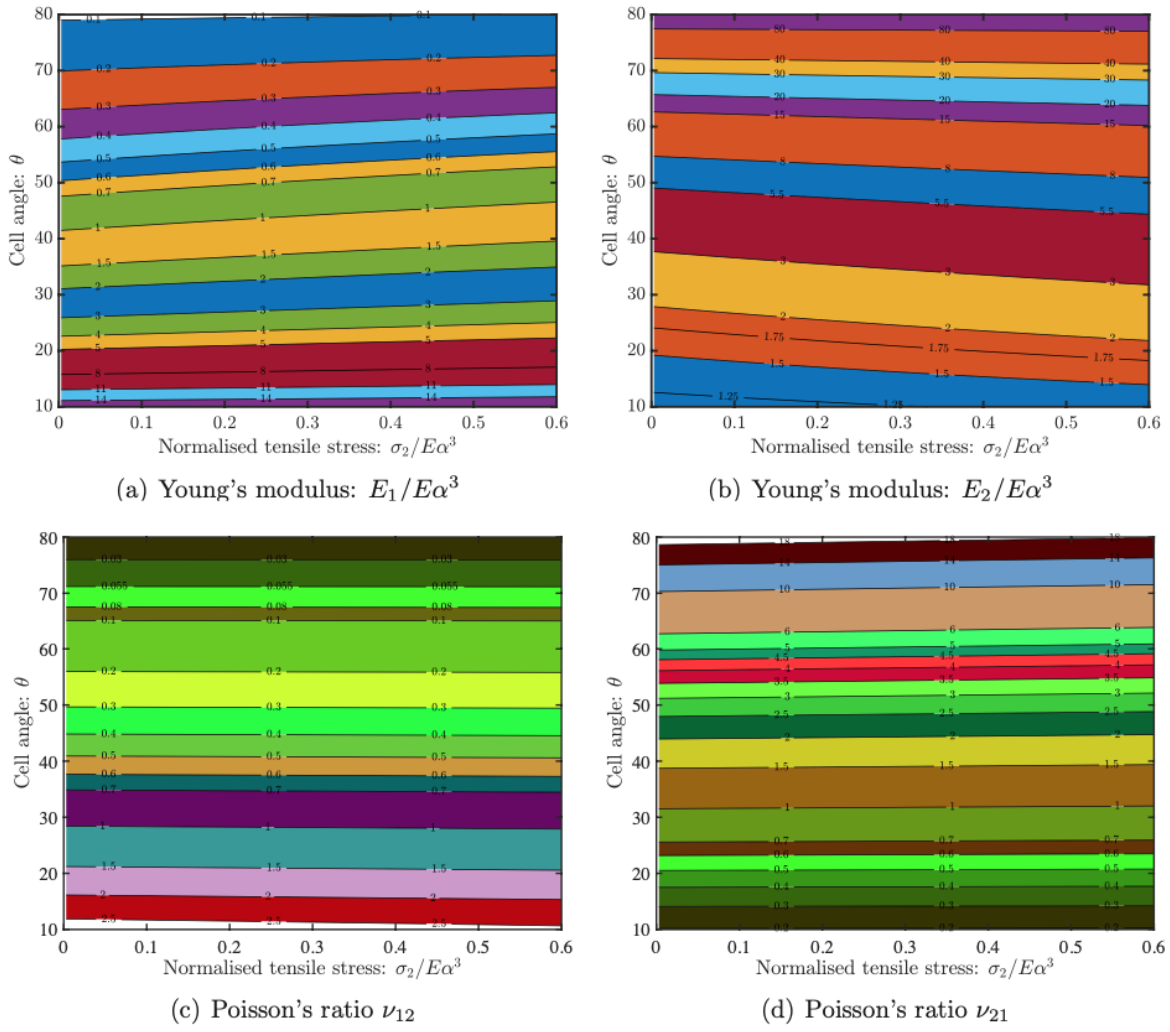

Fig. (16) Contours of the Poisson's ratios and normalised effective elastic moduli of a lattice subjected to a tensile stress in direction 2 corresponding to fig. (7). The normalised tensile stress ($\sigma_2/ E\alpha^3$) varies in the x-axis as well as the cell angle in the y-axis. The geometric dimensional ratios are $\alpha = t/l = 0.15$ and $\beta = h/l = 1$.

2.5.3 Case 6 – Tensile stresses in both directions

And finally, the hexagonal lattice subjected to both a tensile stress in direction-1 and direction-2 is analysed and observed in fig. (17). The equivalent force acting on the unit cell is also shown on fig. (17). The forces applied are equal to the previous case in subsection 2.4.1 where a compressive stress is applied. Therefore, the value of μ is given by eq. (72).

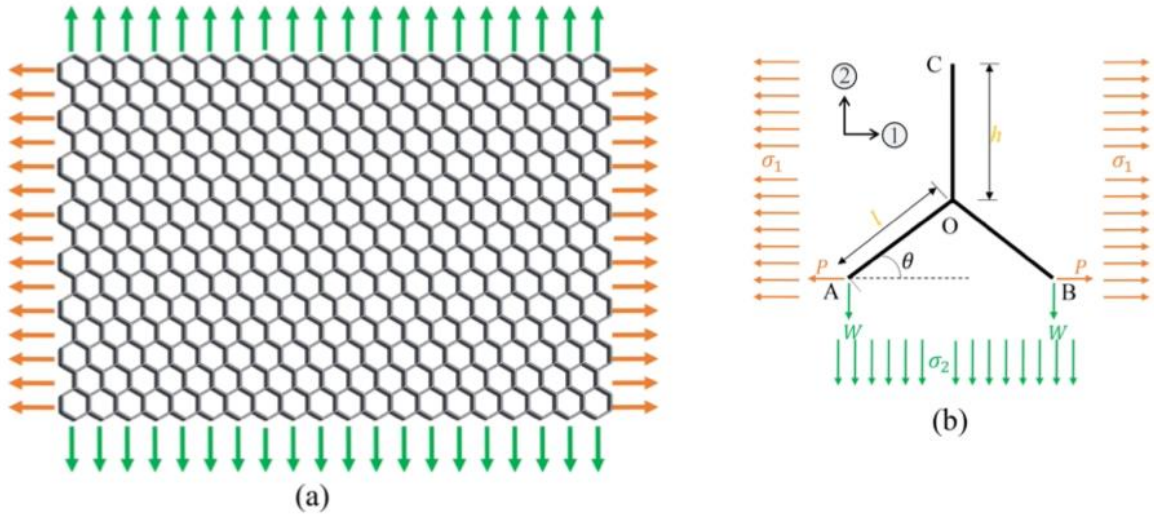

Fig. 17(a) Hexagonal lattice structure experiencing a tense e stress in both directions 1 and 2
Fig. 17(b) Force in the constituent beams within the unit cell model. The tensile axial force is equivalent to Pcos θ + Wsinθ with $P = \sigma_1 b\,(h + l \sin\theta)$ *and* $W = \sigma_2 blcos\theta$

Fig. (18) displays contours of the Poisson's ratios of the lattice when subjected to a tensile stress simultaneously in both direction- 1 and direction- 2 as well as its normalised effective elastic moduli. Both the elastic moduli are normalised by $E\alpha^3$. It is evident that the normalised value increases as the tensile stress values increase. Again, this is expected as by analysing the lattice material, it can be known that the stiffness decreases due to the tensile stress which causes the lattice to experience a stiffening effect in both directions. Consistent with the preceding observations, as the tensile stress increases, there is a slight increase in the Poisson's ratios. But it should be noted that they do not exceed a value of 1 for the parameter range that has been selected.

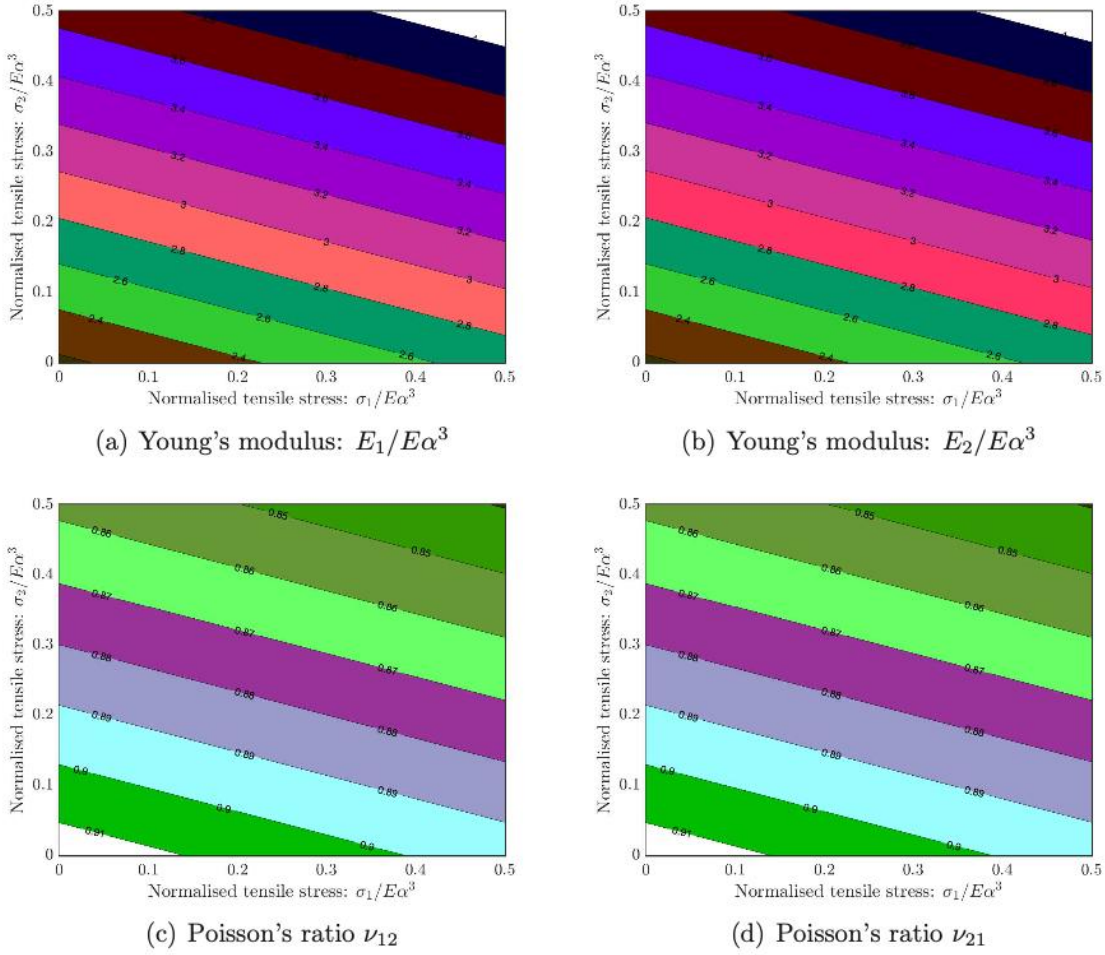

Fig. (18) Contours of the Poisson's ratios and normalised effective elastic moduli of a lattice subjected to a tensile stress in directions 1 and 2 corresponding to fig. (9). The contours of a unit cell with a cell angle of 30 degrees are plotted as normalised tensile stress in both directions with α= t/l =0.15 and β = h/l =1.

2.6 Methodology and Finite Element Analysis Procedures

It is important to emphasise that the finite element analysis is conducted on solid elements. Although using beam elements would increase the promptness of the simulation running time, a major benefit of using solid elements is that it would better resemble the physical problem and captures the influence of the 'joint' regions of the structures. Therefore, offering additional visualised information and allows the behaviour of the component to be fully captured such as distributions of stress and strains which are particularly important in this type of analysis. Furthermore, when conducting the experimental studies, the model to be tested is identical to

those being computationally analysed therefore providing a better comparison between the two results.

Finite element analysis was performed on two separate unit cells with varying cell angle values (θ): 30 and 45 degrees.

2.6.1 Geometry and Material Properties of Unit Cell and Lattice Models

The dimensions applied according to the diagram in fig. (19) to a unit cell with θ=30 degrees were as follows (all values are in millimetres):

- Length *(l)* = 8.23094011
- Height *(h)* = 8.23094011
- Thickness *(t)* = 0.8
- Depth *(b)* = 1

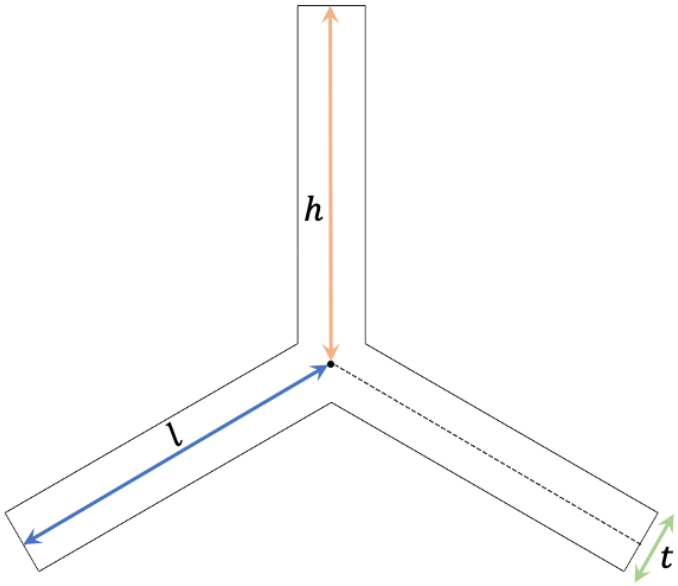

Fig. (19) Dimensions of Unit Cell Model; length (l), height (h) and thickness (t).

Whilst for a unit cell with θ=45 degrees, the dimensions were as follows:

- Length *(l)* = 8
- Height *(h)* = 8

- Thickness *(t)* = 0.8
- Depth *(b)* = 1

Since the simulations were run on a 3D model, these dimensions correspond to the inner skeleton of the solid element, this is again better depicted in fig. (19).

These were then expanded and tessellated to create the hexagonal lattice configuration model. The tested symmetrical model consisted of 20 by 8 hexagon units.

The material properties applied to the unit cell and lattice model were the default material settings of the software, ANSYS. These were from structural steel. This is not particularly important as the results are independent of the material used. The properties that were applied to all the simulations run in this paper are shown in Table (2).

Property	***Value***	***Units***
Elastic Modulus	200	GPa
Poisson's Ratio	0.3	
Mass Density	7850	kgm^{-3}
Tensile Yield Strength	250	MPa
Tensile Ultimate Strength	250	MPa
Shear Modulus	79.615	GPa
Bulk Modulus	172.5	GPa

Table (2) Mechanical Properties of Structural Steel

2.6.2 Simulation Set-Up of Unit Cell

The set-up of the FEA simulation study for the unit cell were again according to subsection 2.4.1. A fixed support was applied to the top face of the unit cell and subjected to compressive forces on the bottom two corner faces in direction-1 which in this case is in the horizontal direction.

The displacements experienced in the x-axis were observed and recorded in the same corner faces where the forces were subjected. In an ideal world, these values should be identical but recognisably in opposite directions. It is important to emphasise that the displacements experienced in the z-axis were fixed to a value of zero as this is an in-plane analysis. This was

observed in all the finite element analysis studies. As previously mentioned, the ‘large displacement’ feature was applied so that the geometrical stiffness can be observed in all cases.

For all finite element analysis studies, a mesh refinement study is highly suggested as it ensures the reliability, accuracy and validity of the results produced by the static simulations. But since ANSYS has a convergence feature, the mesh refinement study was automatically run by the software. The mesh would adapt and became more intricate until the set convergence was found in the results which in all instances was 5%.

2.6.3 Simulation Set-Up of Lattice

The set-up of the FEA simulation study for the lattice were once again according to subsection 2.4.1. A fixed support was applied onto all the parallel faces to the left of the lattice and subjected to various compressive forces on all the faces on the opposite side in direction-1 which in this case is in the vertical direction. The displacements in the x-axis were again observed and recorded. When analysing the lattice, it was found that due to the complexity of the lattice, the simulations were running for a prolonged period therefore a few simplified cases were conducted for each lattice simulated. Dependent on the results from the unit cell cases, three different magnitudes of force were applied that would cover the range that the unit cell was subjected to. This is so that comparisons can be implemented between the unit cell and lattice finite element and the classical case results as well as the exact analytical values. Again, an automatic mesh refinement was run by the convergence feature tool that ANSYS provides.

2.7 Results and Discussion

Graphical representations of the mechanical behaviour of the unit cell and lattice are illustrated. Three graphs in particular are demonstrated: Young’s modulus against the strain, young’s modulus against stress and finally the normalised compressive stress against an equivalent normalised modulus. Within these graphs, the approximate analytical, exact analytical, Gibson Ashby and Euler-Bernoulli values are also plotted in all three figures for comparison purposes. Cases 1 and 4 were particularly the centre of interest. Unequivocally, if the FEA results and theoretical results of these two simple cases were similar then it was assumed this would apply for all the other cases.

2.7.1 Case 1 Results for θ = 30 degrees

Various magnitudes of compressive forces in the horizontal direction were applied to the unit cell and lattice with a cell angle of 30 degrees to obtain the graphs demonstrated by fig. (20). The applied forces were adjusted so that both the unit cell and lattice results were comparable. A negative linear relationship is evident from these illustrations. Since the Gibson-Ashby and Euler-Bernoulli equations are not dependent on the stress applied, the results for these can be seen as a single plot at zero stress. The results from each case were seen to present somewhat identical trends.

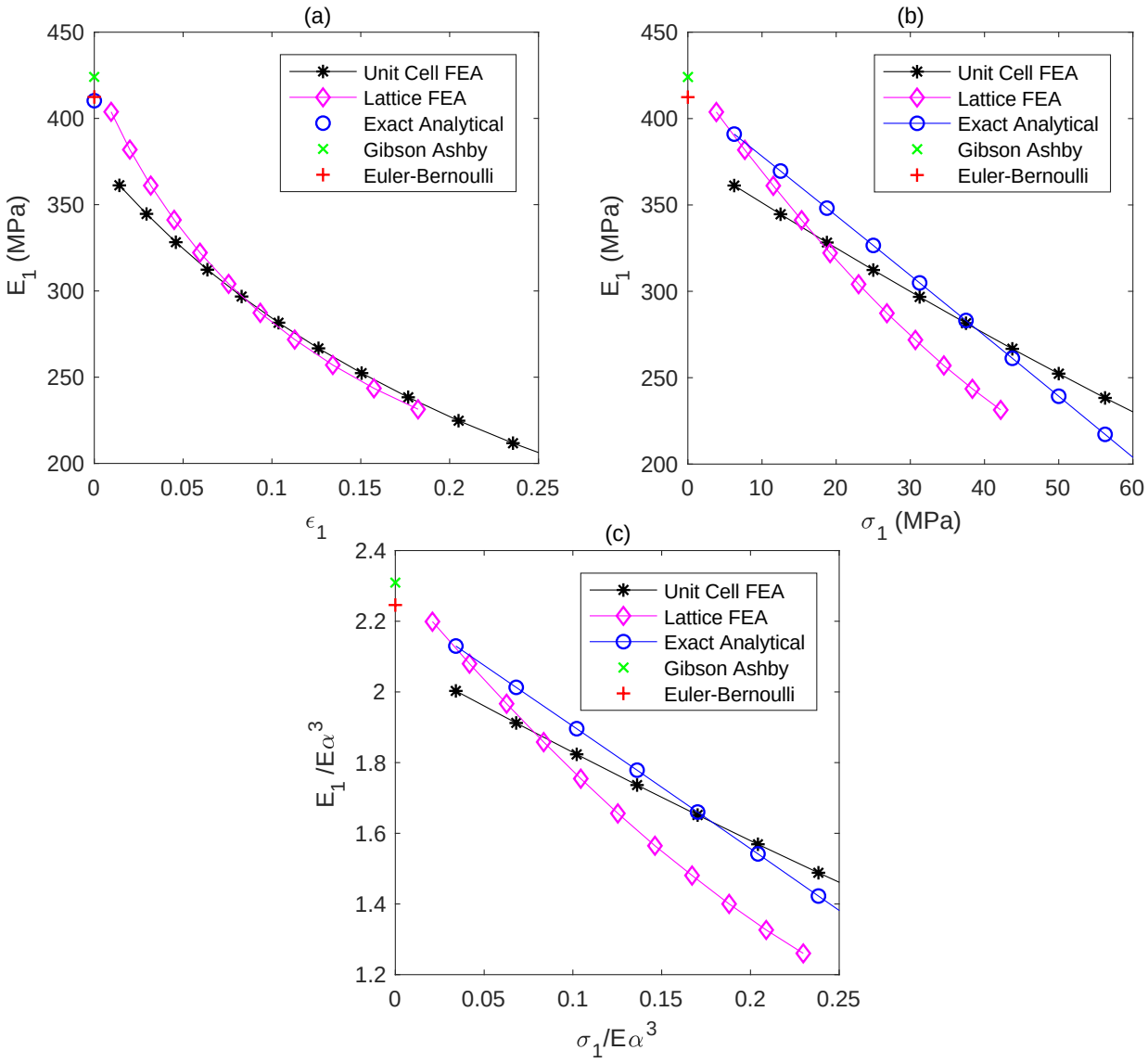

Fig. (20) Three graphs for the results of Case 1 where θ = 30 degrees are illustrated.
(a) Young's Modulus against Strain value
(b) Young's Modulus against Stress value
(c) Normalised Axis

The young's modulus, E_1, against the strain, ε_1, is displayed in fig. 20(a). There is a solid relationship between the two variables and can be observed to have a strong negative correlation for the unit cell and lattice results. Evidently as the applied compressive stress increases, the young's modulus draws further from the classical results.

Furthermore, fig. 20(b) exhibits the young's modulus, E_1, against the compressive stress, σ_1. Linear negative correlations can again be seen in this figure. Similarly, fig. 20(c) shows the same correlation where the equivalent normalised modulus, $E_1/E\alpha^3$, against the normalised compressive stress, $\sigma_1/E\alpha^3$ is plotted. For both cases, as the independent variable increases, the dependent variable decreases and goes further from the classical results. It should be noted that lattice results are seemingly nonlinear.

It should also be noted that the values presented in all graphs (fig. (20 - 23)) have been through the process of calibration, so that the results for all models can be visualised. But overall, for Case 1 where the inclined angle is 30 degrees, the percentage error found between the exact analytical results, unit cell and lattice results were: 9% and 0.5% respectively.

2.7.2 Case 1 Results for θ = 45 degrees

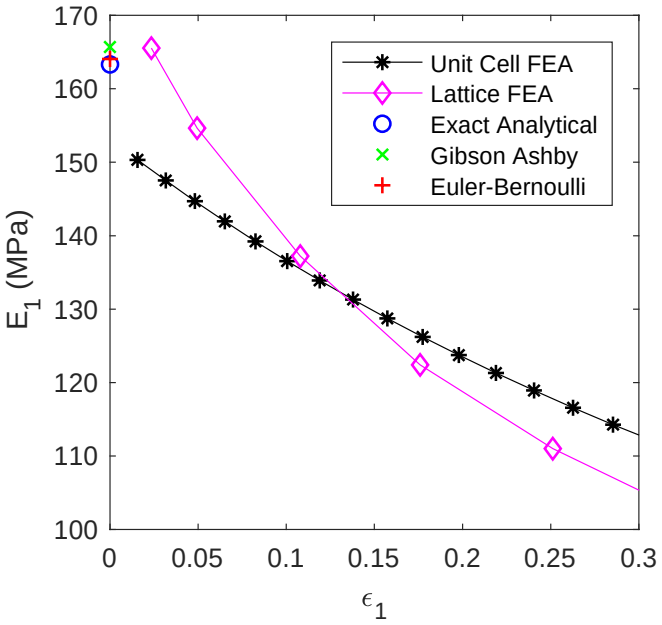

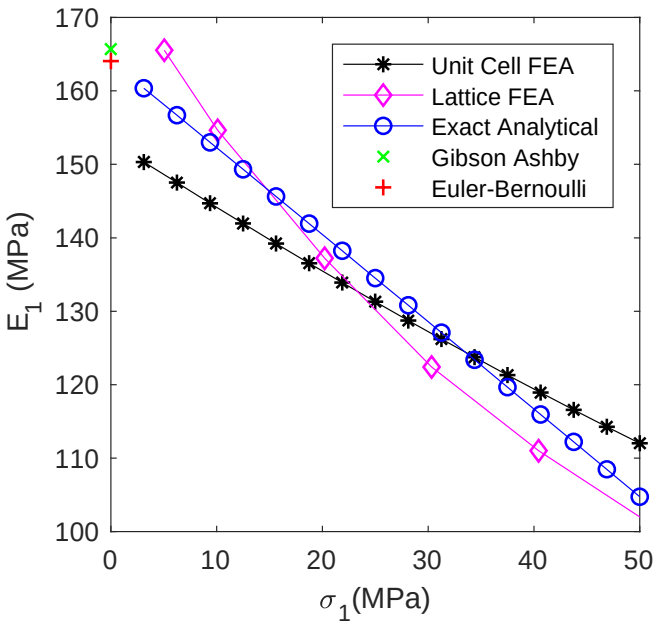

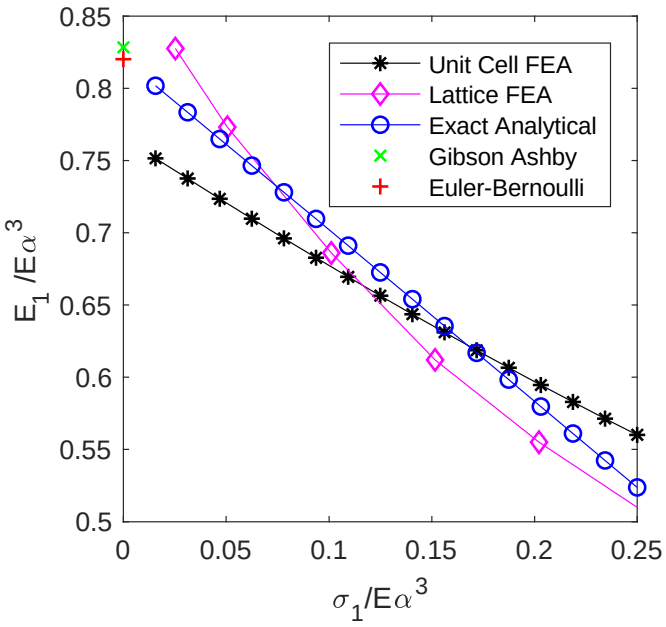

Fig. (21) Three graphs for the results of Case 1 where θ = 45 degrees are illustrated.
(a) Young's Modulus against Strain value
(b) Young's Modulus against Stress value
(c) Normalised Axis

The same graphs have been produced for this case where model subjected to compressive forces has an inclined angle of 45 degrees. The young's modulus, E_1, against the strain, ε_1, is displayed in fig. 21(a). The relationships between the variables are again seen to have a strong negative correlation for the unit cell and lattice results. Evidently as the applied compressive stress increases, the young's modulus draws further from the classical results. In comparison to the previous model, it is perceptible that the young's modulus is found to be larger, more than double, in the model with an inclined angle of 30 degrees. This would indicate a more rigid body, being able to cope with larger magnitudes of compressive stress.

Furthermore, fig. 21(b) again exhibits the young's modulus, E_1, against the compressive stress, σ_1. Linear negative correlations can again be seen in this figure. Similarly, fig. 21(c) shows the same correlation where the equivalent normalised modulus, $E_1/E\alpha^3$, against the normalised compressive stress, $\sigma_1/ E\alpha^3$ is plotted. For both cases, the relationships are identical to the preceding case whereas the independent variable increases, the dependent variable decreases proportionally and goes further from the classical results. It should be noted that lattice results are again seemingly nonlinear.

For this case where the models possess an inclined angle of 45 degrees, the percentage error found between the exact analytical results, unit cell and lattice results were: 15% and 19% respectively.

2.7.3 Case 4 Results for θ = 30 degrees

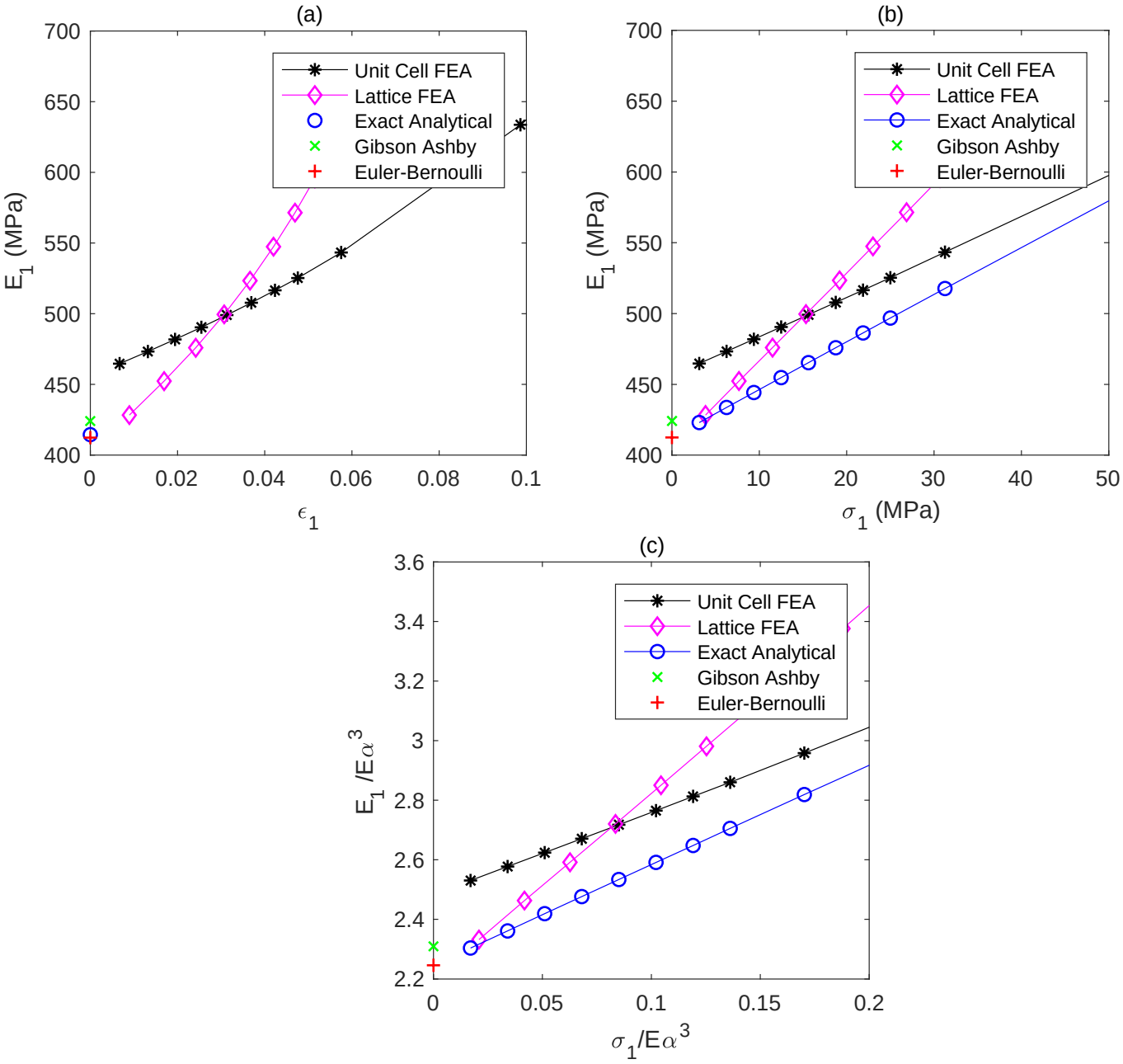

Fig. (22) Three graphs for the results of Case 4 where θ = 30 degrees are illustrated.
(a) Young's Modulus against Strain value
(b) Young's Modulus against Stress value
(c) Normalised Axis

The same graphs have again been produced for this case where the model with an inclined angle of 30 degrees is subjected to magnitudes of tensile forces. The young's modulus, E_1, against the strain, ε_1, is displayed in fig. 22(a). The relationships between the variables are again seen to have a comparatively opposite correlation of Case 1 for the unit cell and lattice results. But similarly, to preceding case, as the applied compressive stress increases, the young's modulus draws further from the classical results.

Continuing, fig. 22(b) again exhibits the young's modulus, E_1, against the compressive stress, σ_1. Linear positive correlations are evident in this figure. Similarly, fig. 22(c) shows the same correlation where the equivalent normalised modulus, $E_1/E\alpha^3$, against the normalised compressive stress, $\sigma_1/ E\alpha^3$ is plotted. For both cases, the relationships are inversely identical to the preceding case whereas the independent variable increases, the dependent variable increases proportionally and goes further from the classical results. It should be noted that the gradient is steeper than the unit cell.

For this case where the models possess an inclined angle of 30 degrees, the percentage error found between the exact analytical results, unit cell and lattice results were: 9% and 2% respectively.

2.7.4 Case 4 Results for $\theta = 45$ degrees

Identical graphs to the preceding cases have been produced for these sets of simulation and theoretical results. The relationships between the variables seen in fig. (23) are similar to the trends in fig. (22). But due to the change in dimensions of the models where the inclined angle has now changed, the percentage errors have increased between the exact analytical values and unit cell results and lattice results: 19% and 22% respectively.

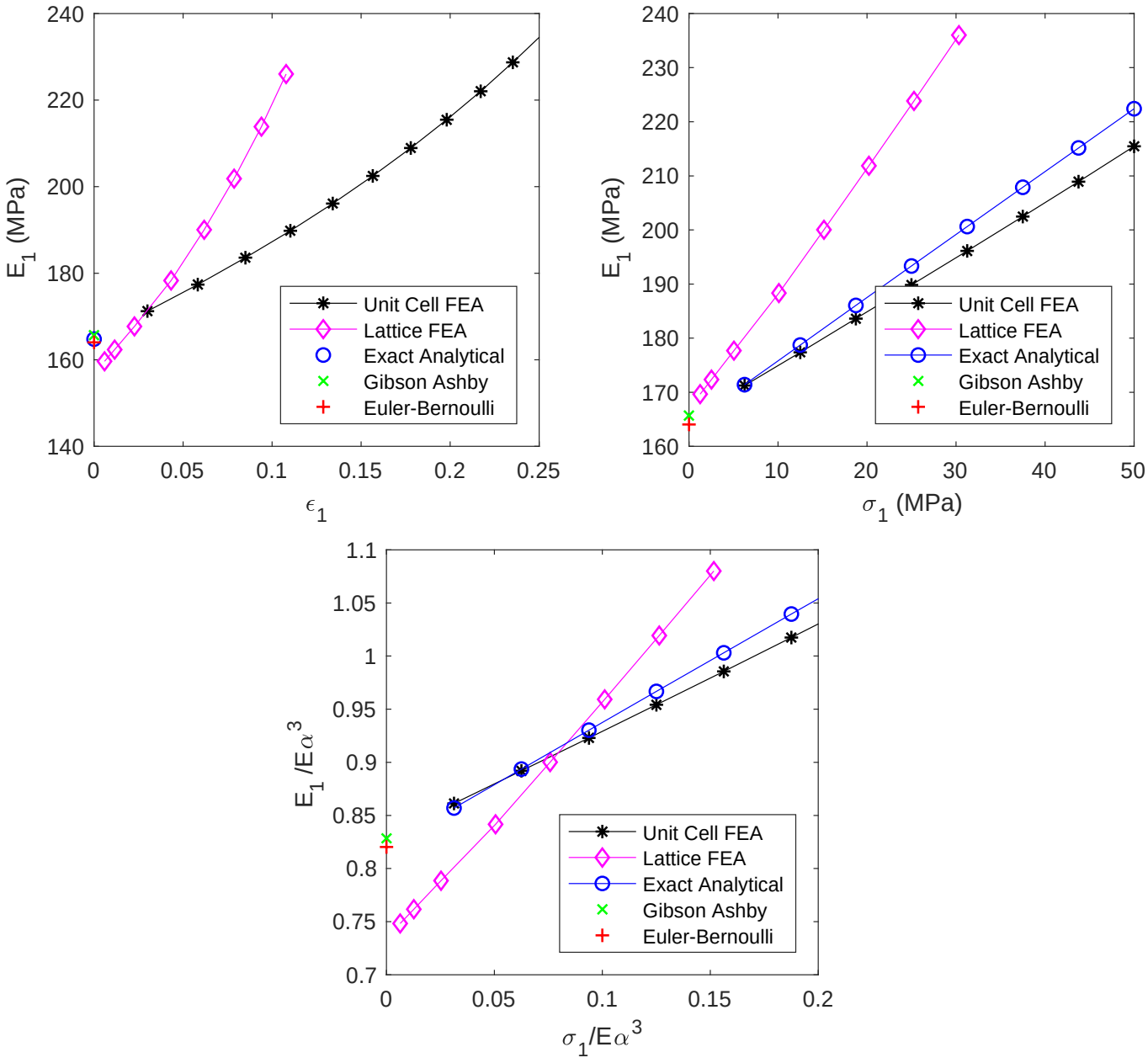

Fig. (23) Three graphs for the results of Case 4 where θ = 45 degrees are illustrated.
(a) Young's Modulus against Strain value
(b) Young's Modulus against Stress value
(c) Normalised Axis

2.7.5 Discussion

It is evident that there is a significant difference in percentage errors between the two cases with varying cell angles. This may occur as the numerical analysis is based on a 2D system. Therefore, when applying the numerical analysis to a 3D simulation with the use of solid elements, it is difficult to determine whether the dimensions for the unit cell and ultimately the

lattice is how the study for finite element analysis has or should have been conducted where the inner skeleton represents the 2D system indicated. Albeit the similarity between the results obtained for the unit cell and lattice for both the numerical analysis and finite element simulations is still remarkable.

2.8 The analysis of different lattice models

The suggested analytical method can be extended to a variety of other lattice patterns and geometry of constituent members thanks to the general formulation built here.

Fig. (24) illustrates three cases specifically chosen to be analysed due to wide interest put upon them. The three cases include the auxetic lattice (θ is negative), the rhombus lattice (h = 0) and the rectangular lattice (θ = 0). Fig. (24) also shows the corresponding unit cell for each special case. The equivalent elastic moduli and Poisson's ratios for all three special cases are then derived.

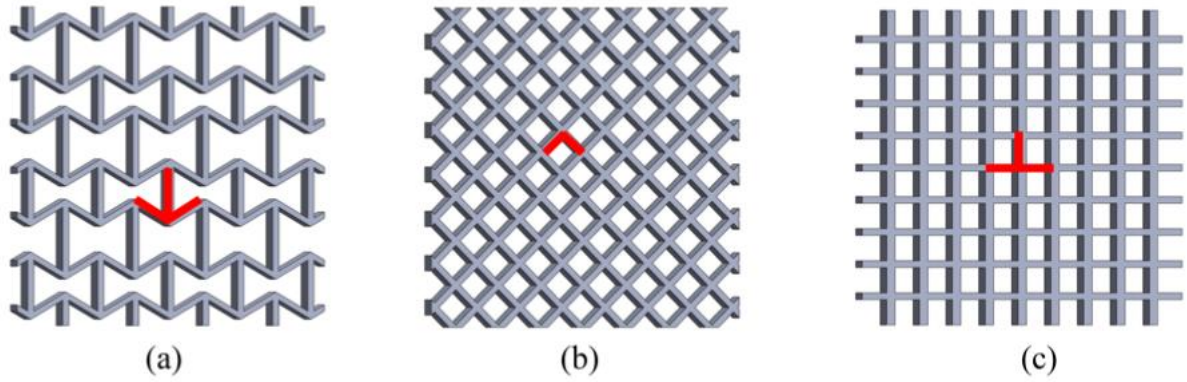

Fig. (24) Three special 2D geometric cases are illustrated.
(a) The auxetic lattice where θ is negative
(b) The rhombus lattice where h=0
(c) The rectangular lattice where θ=0. The corresponding and degenerated unit cells are highlighted in red in the figures.

2.8.1 The auxetic lattice: θ is negative

The first case to be analysed is the auxetic lattice. It can also be known as the re-entrant lattice. This configuration can be obtained when the cell angle, θ, is negative. fig. 24(a) illustrates the unit cell and the corresponding lattice material for this case. Thus, by using the negative angle

of theta and eqs. (60) and (70), for the two directions, the axial force parameter can be obtained as

$$\text{For direction 1: } \mu^2 = \left(\frac{\sigma_1}{E\alpha^3}\right) 12(\beta - \sin\theta)\cos\theta \tag{82}$$

$$\text{For direction 2: } \mu^2 = -\left(\frac{\sigma_2}{E\alpha^3}\right) 12\sin\theta\cos\theta \tag{83}$$

For the stress in direction- 2, it is crucial to be aware that the value of μ^2 is negative. The unit cell structure in fig. 24(a) will physically verify this. Thus, from this, when the subjected stress is in direction- 2, the values of the non-dimensional coefficients, d_1 and d_2 is required to be altered from that in direction- 1. The stiffness coefficients for the tensile case in eq. (44) can be used for the compressive stress, σ_2. And similarly, the stiffness coefficients for the compressive case in eq. (38) can be used for the tensile stress, σ_2. Once the axial force parameter, μ is obtained, the next steps can be taken. The derivation of the equivalent elastic properties of the auxetic lattice from eqs. (52), (53), (54) and (55) as well as using substitution by inputting the negative value of theta. The five equivalent elastic moduli are expressed as

$$E_1(\mu) = \frac{E\alpha^3\cos\theta}{(\beta - \sin\theta)(12\sin^2\theta/d1 + \alpha^2\cos^2\theta)} \tag{84}$$

$$E_2(\mu) = \frac{E\alpha^3(\beta - \sin\theta)}{(12/d1 - \alpha^2)\cos^3\theta + \alpha^2(2\beta + 1)\cos\theta} \tag{85}$$

$$v_{12}(\mu) = -\frac{\cos^2\theta\,(12/d_1 - \alpha^2)}{(\beta - \sin\theta)\sin\theta\,(12/d_1 + \alpha^2\cot^2\theta)} \tag{86}$$

$$v_{21}(\mu) = -\frac{(\beta - \sin\theta)\sin\theta\,(12/d_1 - \alpha^2)}{(12/d_1 - \alpha^2)\cos^2\theta + \alpha^2(2\beta + 1)} \tag{87}$$

The shear modulus can also be obtained from Eq. (58) as:

$$G_{12}(\mu) = \frac{E\alpha^3(\beta - \sin\theta)}{\left(\beta^2\left(\frac{6}{d_2} + 2\beta\right) + \alpha^2(\cos\theta - (\beta - \sin\theta)\tan\theta)^2\right)\cos\theta} \tag{88}$$

2.8.2 The rhombus lattice: h=0

The second case is the rhombus lattice, and this can be obtained when h = β = 0. Due to this, it indicates that vertical member is absent in this case. This reconfigured unit cell is illustrated in fig. 24(b) with its corresponding lattice structure. By using the limit β = 0 and substituting it into eq. (60), the axial force parameter for stress applied in direction- 1 can be obtained as

$$\mu = \lim_{\beta \to 0} \sqrt{\left(\frac{\sigma_1}{E\alpha^3}\right) 12(\beta + \sin\theta)\cos\theta} = \sqrt{\left(\frac{\sigma_1}{E\alpha^3}\right) 12 \sin\theta \cos\theta} \tag{89}$$

But on the contrary, eq. (70) does not change which is the expression giving the axial force parameter for stress in direction- 2. This is because it is not a function of β. Once the axial force parameter, μ is obtained, the next steps can be taken. The derivation of the equivalent elastic properties of the auxetic lattice from the same equations as the previous case, eqs. (52), (53), (54) and (55), as well as using substitution by inputting the value of beta. The five equivalent elastic moduli are expressed as

$$E_1(\mu) = \lim_{\beta \to 0} \frac{E\alpha^3 \cos\theta}{(\beta - \sin\theta)(12\sin^2\theta\,/d1 + \alpha^2\cos^2\theta)} = \frac{E\alpha^3\cos\theta}{\sin\theta\,(12\sin^2\theta\,/d1 + \alpha^2\cos^2\theta)} \tag{90}$$

$$E_2(\mu) = \lim_{\beta \to 0} \frac{E\alpha^3(\beta + \sin\theta)}{(12/d1 - \alpha^2)\cos^3\theta + \alpha^2(2\beta + 1)\cos\theta} = \frac{E\alpha^3\sin\theta}{\cos\theta\,(12\sin^2\theta\,/d1 + \alpha^2\cos^2\theta)} \tag{91}$$

$$v_{12}(\mu) = \lim_{\beta \to 0} \frac{\cos^2\theta\,(12/d_1 - \alpha^2)}{(\beta + \sin\theta)\sin\theta\,(12/d_1 + \alpha^2\cot^2\theta)} = \frac{\cos^2\theta\,(12/d_1 - \alpha^2)}{12/d_1 + \alpha^2\cos^2\theta} \tag{92}$$

$$v_{21}(\mu) = \lim_{\beta \to 0} \frac{(\beta + \sin\theta)\sin\theta\,(12/d_1 - \alpha^2)}{(12/d_1 - \alpha^2)\cos^2\theta + \alpha^2(2\beta + 1)} = \frac{\sin^2\theta\,(12/d_1 - \alpha^2)}{12\cos^2\theta\,/d_1 + \alpha^2\sin^2\theta} \tag{93}$$

Following the same procedure, the shear modulus can be obtained from Eq. (58) as

$$G_{12}(\mu) = \lim_{\beta \to 0} \frac{E\alpha^3(\beta - \sin\theta)}{\left(\beta^2\left(\frac{6}{d_2} + 2\beta\right) + \alpha^2(\cos\theta + (\beta + \sin\theta)\tan\theta)^2\right)\cos\theta} = E\alpha\sin\theta\cos\theta \tag{94}$$

2.8.3 The rectangular lattice: θ = 0

Finally, the last case of the rectangular lattice is analysed. This configuration can be obtained when θ = 0. Due to this, it indicates that two inclined members/beams are parallel in this case. This reconfigured unit cell is illustrated in fig. 24(c) with its corresponding lattice structure. By using the limit θ = 0 and substituting it into eq. (60), the axial force parameter for stress applied in direction- 1 can be obtained as

$$\mu = \lim_{\theta \to 0} \sqrt{\left(\frac{\sigma_1}{E\alpha^3}\right) 12(\beta + \sin\theta)\cos\theta} = \sqrt{\left(\frac{\sigma_1}{E\alpha^3}\right) 12\beta} \tag{95}$$

Eq. (70), the expression giving the axial force parameter for stress in direction- 2, is now equal to 0 when θ = 0. Due to this equation being nullified, the elastic properties of the rectangular lattice are not affected by the stress applied in direction- 2. The derivation of the equivalent elastic properties of the auxetic lattice from the same equations as the previous case, eqs. (52), (53), (54) and (55), as well as using substitution by inputting the value of theta as

$$E_1(\mu) = \lim_{\theta \to 0} \frac{E\alpha^3 \cos\theta}{(\beta + \sin\theta)(12\sin^2\theta\,/d1 + \alpha^2\cos^2\theta)} = \frac{E\alpha}{\beta} \tag{96}$$

$$E_2(\mu) = \lim_{\theta \to 0} \frac{E\alpha^3(\beta + \sin\theta)}{(12/d1 - \alpha^2)\cos^3\theta + \alpha^2(2\beta + 1)\cos\theta} = \frac{E\alpha^3\beta}{12/d_1 + 2\alpha^2\beta} \tag{97}$$

$$v_{12}(\mu) = \lim_{\theta \to 0} \frac{\cos^2\theta\,(12/d_1 - \alpha^2)}{(\beta + \sin\theta)\sin\theta\,(12/d_1 + \alpha^2\cot^2\theta)} = 0 \tag{98}$$

$$v_{21}(\mu) = \lim_{\theta \to 0} \frac{(\beta + \sin\theta)\sin\theta\,(12/d_1 - \alpha^2)}{(12/d_1 - \alpha^2)\cos^2\theta + \alpha^2(2\beta + 1)} = 0 \tag{99}$$

It is evident that both the Poisson's ratios are equal to zero and the moduli E1 is independent of the applied stress.

Following the same procedure, the shear modulus can be obtained from eq. (58) as

$$\begin{aligned} G_{12}(\mu) &= \lim_{\theta \to 0} \frac{E\alpha^3(\beta + \sin\theta)}{\left(\beta^2\left(\frac{6}{d_2} + 2\beta\right) + \alpha^2(\cos\theta + (\beta + \sin\theta)\tan\theta)^2\right)\cos\theta} \\ &= \frac{E\alpha^3\beta}{\beta^2\left(\frac{6}{d_2} + 2\beta\right) + \alpha^2} \end{aligned} \tag{100}$$

2.9 Conclusions

From the analysis executed in the preceding sections, it is evident that a vital problem of highly stretchable and compressible lattice materials is the underlying geometric nonlinearity. This feature of the lattice was found to cause both the axial softening and stiffening of the constituent beam elements depending on whether a compressive or tensile stress is subjected upon the lattice. An in-depth analysis and solely physics-based approached was observed. Following this approach led to the determination of closed-form expressions of in-plane equivalent elastic properties of the hexagonal lattice configuration. The bottom-up approach was also presented allowing three key steps required to be accomplished to acquire the correct analytical derivations. The first step to be taken was grasping that the constituent members of the lattice are thin beam elements. In this case, it was understood that the stiffness matrices of beams when subjected to compressive and tensile stresses were then derived. The exact solutions of the governing ordinary differential equation with appropriate boundary conditions, also known as transcendental displacement functions, were used to attain these matrices. Secondly, from the bottom-up approach, the unit cell was next observed. Using the mechanics, a selected unit cell the five equivalent elastic moduli of the lattice were derived: Young's Moduli, Poisson's ratios, and the shear modulus. This was the case as the expressions resulting from this analysis utilise the stiffness matrix derived in the first stage. And finally, from combining steps one and two, the equivalent elastic properties were obtained for lattice subjected to compressive and tensile stresses. Th equivalent properties found were nonlinear functions of the applied compressive stresses (through trigonometric functions) and tensile stresses (through hyperbolic functions). Due to the nature of the functions used, this resulted in a nonlinear homogenous stress-strain relationship for the cellular material.

The distinct aspects of this chapter include:

- A general methodology and procedure to be taken to derive the equivalent elastic properties of the hexagonal lattice configurations using the non-dimensional coefficients of the stiffness matrix of the constituent beams.
- The use of ordinary differential equations to govern the deformation of axially loaded beams and the integration of the results into the unit cell-based analysis.
- Exact closed-form expressions are used to directly quantify the effect of external compressive and tensile stresses on analogous elastic properties.

- Many special cases of interest are defined by taking approximate mathematical limits, resulting in the generalised nature of the newly derived expressions. The general expressions for the equivalent elastic properties were used to examine three special cases of broad interest, namely auxetic hexagonal, rhombus-shaped, and rectangular lattices.

The validation for the analytical expressions derived has been determined through finite element analysis with nonlinear analysis for both compression and tension applied. The results obtained from the analytical expressions are graphically depicted as functions of the applied compressive and tensile stresses. Three special cases were analysed for each type of applied stress; the stress is applied in directions 1, direction- 2 and both directions 1 and 2. When a compressive stress is applied to the lattice, it was found that there was a decrease in the effective elastic moduli. But for the tensile case the circumstances were different and opposite to the preceding case as the effective elastic moduli would increase. The Poisson's ratio for both cases were analogous where there was no significant change when subjected to an external stress.

Further into the finite element analysis static simulations conducted. Solid elements (3D FEA) were analysed over beam elements since the real world and physical phenomena are better replicated and simulated through this element type. A further analysis is conducted using solid elements since it provides more detail about the mechanical properties of the structure. This is particularly important in the procurement of the results required for this paper. The results in each case show somewhat matching results in the two analytical methods used. Most notably, cases 1 and 4, for both cell angles analysed, show promising results with miniscule percentage errors ranging between 2 and 10%. Whilst for more complicated cases, namely cases 3 and 6, where two forces are applied to the structures in different directions, the percentage errors were almost triple the errors of the preceding cases discussed. In terms of physical meaning, general behaviours of the structure have been depicted highlighting the stiffening/softening effect of increasing stress.

2.10 Recommendations for Future Work

The expressions derived provide a basis and great opportunity to be utilised in many engineering and scientific applications. More specifically in the design and optimisation of highly stretchable and compressible 2D lattices. While the geometric nonlinearity resulting from large deformation is written in this paper, the material behaviours are presumed to be linear. Therefore, upon completing this chapter of this research, there are numerous ways in which the work covered in the prior sections could be further developed. It is recommended that the following aspects are considered in the future:

- Focus on nonlinear material behaviour to incorporate the numerous available materials that can manufacture lattices.
- The same analysis procedure to be carried out on different lattice structures such as the three special cases discussed in section 6 of this chapter.

Chapter 3 – Stepped Profile

3.1 Introduction

As previously mentioned, this chapter of the paper explores one approach of optimising a hexagonal structure, with the aim of increasing the strength to weight ratio, through redistributing the cross-sectional area of the single beam element by introducing ‘steps’. This is then developed into a full system and analysed. The structural nature of the distorted hexagonal cellular lattice is once again analysed through computational modelling. The two major forms to be analysed and demonstrated are step-up and step-down geometries.

The optimisation approach of the stepped lattice was chosen to be analysed since it was found that specific sections of the constituent beams of the lattice experience different magnitudes of stress. The outer section of the segment experiences the higher magnitudes of stress whilst the inner section experiences the least. Therefore, different forms as mentioned, the step-up and step-down geometries, are set to be analysed.

3.2 Framework of Stepped Lattices

The stepped lattice optimisation concept was developed as a simple solution where analysis can be conducted. As mentioned, two types of geometrical changes have been applied with the aim of optimising the properties of the lattice structure. The optimisation of the lattice in this section involves the redistribution of the mass of a conventional honeycomb lattice through the introduction of ‘steps. This is better depicted in fig. (25). The objective of this analysis is to understand the effect of this redistribution whilst also obtaining the range of equivalent elastic parameter values which can then be further exploited for design purposes. Due to the mass constraints, this causes a limitation upon the parameters of the structure. The geometry of the constituent beam member of regular hexagonal lattice, stepped lattice and their parameter limitations are described in the next subsection. A stepped lattice and its corresponding unit cells are seen in fig. (25).

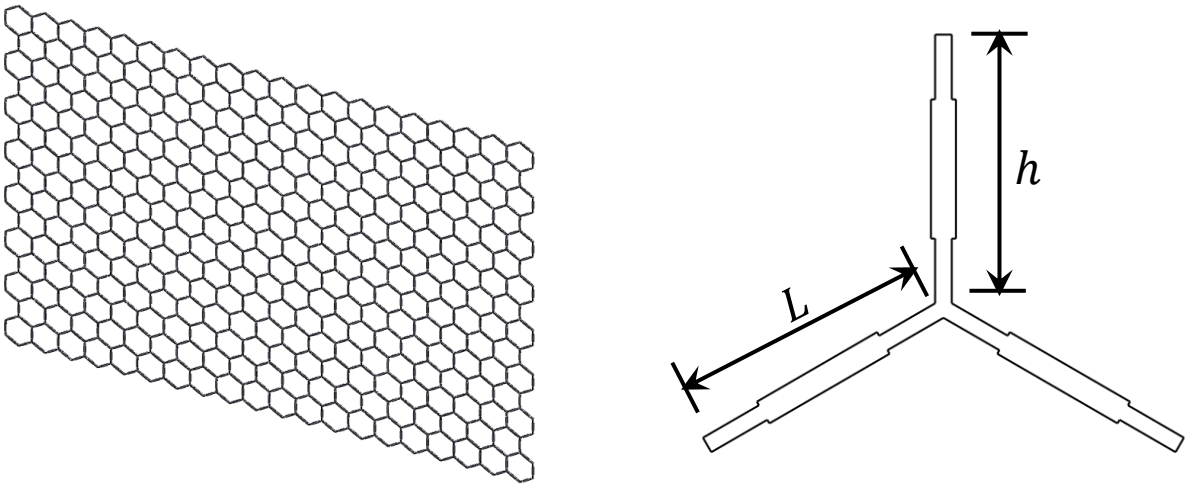

(a) (b)

Fig. (25) (a) Stepped Lattice Geometry
Fig. (25) (b) Corresponding Unit Cell of the stepped lattice seen in (a)

3.3 Numerical Analysis

Following the bottom-up approach previously used in the preceding chapter, the honeycomb is once again deconstructed and analysed individually and eventually altogether as one whole system.

3.3.1 Numerical Analysis of a Cantilever Beam

When completely dismantling the lattice, the first segment to be analysed is the cantilever beam. Fig. (26) demonstrates the uniform prismatic structure whilst fig. (27) displays the irregular altered beam. The new dimensions applied to the optimised beam for the numerical analysis were as follows:

- Thickness of middle segment (t_1)
- Thickness of outer segments (t_2)
- Length on middle segment (L_1)

- Length of outer segments (L_2)

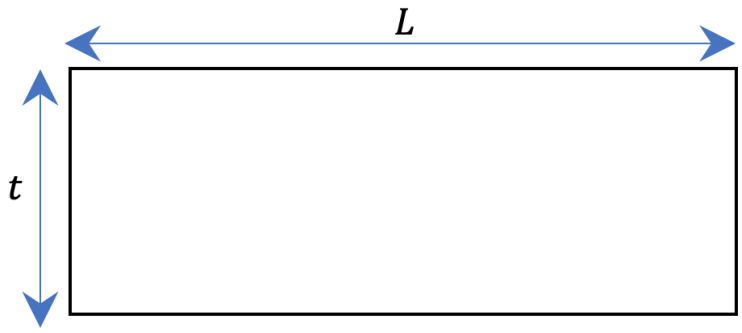

Fig. (26) Dimensions of Uniform Beam

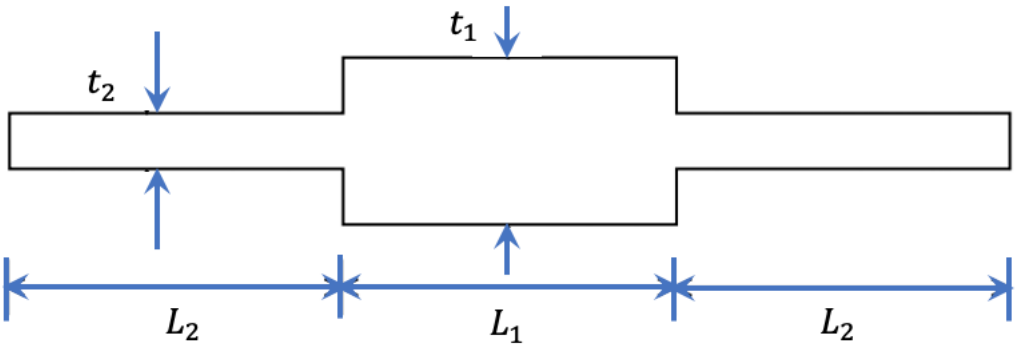

Fig. (27) Dimensions of Stepped Beam

The key aim in the numerical analysis of the beam element is to equate the cross-sectional area of the uniform beam and the stepped beam for comparison purposes. This would then also lead to equating masses. The values of different lengths and thicknesses of the stepped beam are as follows:

- $L_2 = \eta L$
- $L = (1 - 2\eta)$
- $t_1 = \alpha_1 t$
- $t_2 = \alpha_2 t$

When considering the density of the material, ρ, and through equating the masses of the uniform beam and the optimised stepped beam, the following can be obtained:

$$A\rho = Lt\rho = 2(\alpha_2 t)\eta L\rho + \alpha_1 t(1 - 2\eta)L\rho \quad (101)$$

$$2(\alpha_2 t)\eta + \alpha_1 t(1 - 2\eta) = 1 \quad (102)$$

Thus, the value of α_1 is:

$$\alpha_1 = \frac{1 - 2\alpha_2\eta}{1 - 2\eta} \quad (103)$$

From this, it is evident that $\eta < \frac{1}{2}$.

As seen in fig. (27), the stepped beam has been divided into three parts. Therefore, the equation for the strain energy becomes:

$$U = \frac{1}{2}\int_0^{L_2} \frac{M^2}{EI_2}dx + \frac{1}{2}\int_0^{L_2} \frac{N^2}{EA_2}dx + \frac{1}{2}\int_{L_1}^{L_1+L_2} \frac{M^2}{EI_1}dx + \frac{1}{2}\int_{L_1}^{L_1+L_2} \frac{N^2}{EA_1}dx + \frac{1}{2}\int_{L_1+L_2}^{L} \frac{M^2}{EI_2}dx + \frac{1}{2}\int_{L_1+L_2}^{L} \frac{N^2}{EA_2}dx \quad (104)$$

The coefficients Qis for the stepped beam are defined as

$$Q_i = \int_0^{L_2} \frac{x^{(i-1)}}{EI_2}dx + \int_{L_2}^{L_1+L_2} \frac{x^{(i-1)}}{EI_1}dx + \int_{L_1+L_2}^{L} \frac{x^{(i-1)}}{EI_2}dx \qquad i = 1-3 \quad (105)$$

$$S = \int_0^{L_1} \frac{1}{EA_2}dx + \int_{L_2}^{L_1+L_2} \frac{1}{EA_1}dx + \int_{L_1+L_2}^{L} \frac{1}{EA_2}dx \quad (106)$$

The representation of each symbol is as follows:

- $I_1 = \frac{bt_1^3}{12}$
- $I_2 = \frac{bt_1^3}{12}$
- $A_1 = bt_1$
- $A_2 = bt_2$

The stiffness values of the bending and axial parts are obtained separately. After all simplifications are conducted, the stiffness matrix for the constituent Euler Bernoulli is as follows

$$K_{ij} = \begin{bmatrix} a_1\frac{EA}{L} & 0 & 0 & -a_1\frac{EA}{L} & 0 & 0 \\ 0 & d_1\frac{12EI}{L^3} & d_2\frac{6EI}{L^2} & 0 & -d_1\frac{12EI}{L^3} & d_2\frac{6EI}{L^2} \\ 0 & d_2\frac{6EI}{L^3} & d_3\frac{4EI}{L} & 0 & -d_2\frac{6EI}{L^2} & d_4\frac{2EI}{L} \\ -a_1\frac{EA}{L} & 0 & 0 & a_1\frac{EA}{L} & 0 & 0 \\ 0 & -d_1\frac{12EI}{L^3} & -d_2\frac{6EI}{L^2} & 0 & d_1\frac{12EI}{L^3} & -d_2\frac{6EI}{L^2} \\ 0 & d_2\frac{6EI}{L^3} & d_4\frac{2EI}{L} & 0 & -d_2\frac{6EI}{L^2} & d_3\frac{4EI}{L} \end{bmatrix} \quad (107)$$

Where the representation of each symbol is as follows:

- A – Cross sectional area of the regular beam with equivalent mass as the stepped beam
- I – Moment of Inertia of the regular beam with equivalent mass as the stepped beam
- $a_1 = \frac{1}{{\alpha_1}^2 - 2\eta({\alpha_1}^2 - {\alpha_2}^2)}$
- $d_1 = \frac{{\alpha_1}^3 {\alpha_2}^3}{({\alpha_1}^3 - {\alpha_2}^3)(((2\eta-1)^3+1)+{\alpha_2}^3}$
- $d_2 = d_1 = \frac{{\alpha_1}^3 {\alpha_2}^3}{({\alpha_1}^3 - {\alpha_2}^3)(((2\eta-1)^3+1)+{\alpha_2}^3}$
- $d_3 = \frac{{\alpha_1}^3 {\alpha_2}^3 ((((\alpha_1^3 - \alpha_2^3)((\eta-1)^3+1+\eta^3)+\alpha_2^3)}{(2\eta(\alpha_1^3 - \alpha_2^3)+\alpha_2^3)((\alpha_1^3 - \alpha_2^3)(((2\eta-1)^3+1)+{\alpha_2}^3}$
- $d_4 = \frac{{\alpha_1}^3 {\alpha_2}^3 (\alpha_2^3 - (\alpha_1^3 - \alpha_2^3)(4\eta^3 - 6\eta^2))}{(2\eta(\alpha_1^3 - \alpha_2^3)+\alpha_2^3)((\alpha_1^3 - \alpha_2^3)(((2\eta-1)^3+1)+{\alpha_2}^3}$

By applying the limits, $\lim_{\alpha_1 \to 1 \alpha_2 \to 1}$ from the case of a regular beam and the coefficient a_1, $\bar{d}_i$ become

$$\lim_{\alpha_1 \to 1 \alpha_2 \to 1} a_1 = \lim_{\alpha_1 \to 1 \alpha_2 \to 1} \frac{1}{\alpha_1^2 - 2\eta(\alpha_1^2 - \alpha_2^2)} = 1 \tag{108}$$

$$\lim_{\alpha_1 \to 1 \alpha_2 \to 1} d_1 = \lim_{\alpha_1 \to 1 \alpha_2 \to 1} \frac{1}{(\alpha_1^3 - \alpha_2^3)(2\eta - 1) + 1) + \alpha_2^3)} = 1 \tag{109}$$

$$d_2 = d_1 \tag{110}$$

$$\lim_{\alpha_1 \to 1 \alpha_2 \to 1} d_3 = \lim_{\alpha_1 \to 1 \alpha_2 \to 1} \frac{\alpha_1^3 \alpha_2^3 (((\alpha_1^3 - \alpha_2^3)((\eta-1)^3 + 1 + \eta^3) + \alpha_2^3}{(2\eta(\alpha_1^3 - \alpha_2^3) + \alpha_2^3)(\alpha_1^3 - \alpha_2^3)((2\eta-1)^3 + 1) + \alpha_2^3)} = 1 \tag{111}$$

$$\lim_{\alpha_1 \to 1 \alpha_2 \to 1} d_4 = \lim_{\alpha_1 \to 1 \alpha_2 \to 1} \frac{\alpha_1^3 \alpha_2^3 (\alpha_2^3 - (\alpha_1^3 - (\alpha_1^3 - \alpha_2^3)(4\eta^3 - 6\eta^2)}{(2\eta(\alpha_1^3 - \alpha_2^3) + \alpha_2^3)((\alpha_1^3 - \alpha_2^3)((2\eta-1)^3 + 1) + \alpha_2^3)} = 1 \tag{112}$$

When considering, all the limitations of the values, the stiffness matrix for the regular Euler Bernoulli beam becomes

$$K_{ij} = \begin{bmatrix} \frac{EA}{L} & 0 & 0 & -\frac{EA}{L} & 0 & 0 \\ 0 & \frac{12EI}{L^3} & \frac{6EI}{L^2} & 0 & -\frac{12EI}{L^3} & \frac{6EI}{L^2} \\ 0 & \frac{6EI}{L^3} & \frac{4EI}{L} & 0 & -\frac{6EI}{L^2} & \frac{2EI}{L} \\ -\frac{EA}{L} & 0 & 0 & \frac{EA}{L} & 0 & 0 \\ 0 & -\frac{12EI}{L^3} & -\frac{6EI}{L^2} & 0 & \frac{12EI}{L^3} & -\frac{6EI}{L^2} \\ 0 & \frac{6EI}{L^3} & \frac{2EI}{L} & 0 & -\frac{6EI}{L^2} & \frac{4EI}{L} \end{bmatrix} \tag{113}$$

Where again:

- $I = \frac{bt^3}{12}$
- $A = bt$

After considering the stiffness coefficients from eq. (31), the non-dimensional geometric parameters are defined as

$$\alpha = \frac{t}{L} \quad and \quad \beta = \frac{h}{L} \tag{114}$$

where *t*, is the thickness of the uniform beam.

3.3.2 Numerical Analysis of the Lattice

For the numerical analysis of the lattice, the expressions of the moment of inertia and the cross-sectional area can be used to obtain the stiffness coefficients. These are given by the follow expressions:

- $K_{55} = d_1 \frac{12EI}{L^3} = d_1 Eb{\alpha_1}^3$
- $K_{44} = a_1 \frac{EA}{L} = a_1 Eb\alpha$
- $K_{44}^h = a_1 \frac{EA}{h} = a_1 \frac{Eb\alpha}{\beta}$

It can then be found that

- $\frac{K_{55}}{K_{44}} = \alpha^2 \frac{d_1}{a_1}$
- $\frac{K_{55}}{K_{44}^h} = \alpha^2 \beta \frac{d_1}{a_1}$

The generalised expressions for the optimised stepped lattice can now be obtained as

$$E_1 = \frac{d_1 E \alpha^3 cos\theta}{(\beta + sin\theta)\left(\sin^2\theta + \alpha^2 \frac{d_1}{a_1} cos^2\theta\right)} \tag{115}$$

$$E_2 = \frac{d_1 E \alpha^3 (\beta + sin\theta)}{cos^3\theta\left(1 + \alpha^2 \frac{d_1}{a_1} tan^2\theta + 2\alpha^2 \beta \frac{d_1}{a_1} sec^2\theta\right)} \tag{116}$$

$$v_{12} = \frac{\left(1 - \alpha^2 \frac{d_1}{a_1}\right) sin\theta\, cos^2\theta}{(\beta + sin\theta)\left(\sin^2\theta + \alpha^2 \frac{d_1}{a_1} cos^2\theta\right)} \tag{117}$$

$$v_{21} = \frac{\left(1 - \alpha^2 \frac{d_1}{a_1}\right) sin\theta(\beta + sin\theta)}{\left(1 + \alpha^2 \frac{d_1}{a_1} tan^2\,\theta + 2\alpha^2 \beta \frac{d_1}{a_1} sec^2\,\theta\right)} \tag{118}$$

Where;

$$G_{12} = \frac{(\beta + sin\theta) E \alpha^3 d_2 (4d_{1h} - 3d_{2h}^2) a_1 cos\theta}{2\left(a_1 d_2 \beta + 2\left(-\alpha^2 d_2 + a_1\right)\left(d_{1h} d_{3h} - \frac{3}{4} d_{2h}^2\right)\right)\beta^2 cos^2\,\theta + 8d_2\left(\beta + sin\theta + \frac{1}{2}\beta^2 + \frac{1}{2}\right)\left(d_{1h} d_{3h} - \frac{3}{4} d_{2h}^2\right)\alpha^2} \tag{119}$$

$$K_{55}^{\frac{h}{2}} = K_{55}^0 d_{1h} = \frac{12EI}{\left(\frac{h}{2}\right)^3} d_{1h} \tag{120}$$

$$K_{56}^{\frac{h}{2}} = K_{56}^0 d_{2h} = -\frac{6EI}{\left(\frac{h}{2}\right)^2} d_{2h} \tag{121}$$

$$K_{66}^{\frac{h}{2}} = K_{66}^0 d_{3h} = \frac{4EI}{\frac{h}{2}} d_{3h} \tag{122}$$

$$d_{1h} = \frac{\alpha_1^3 \alpha_2^3 (2\eta(\alpha_1^3 - \alpha_2^3)\alpha_2^3)}{D_{EB}^h} \tag{123}$$

$$d_{2h} = \frac{((\alpha_1^3 - \alpha_2^3)(4\eta^2 - 4\eta) - \alpha_2^3)\alpha_1^3 \alpha_2^3}{D_{EB}^h} \tag{124}$$

$$d_{3h} = \frac{((\alpha_1^3 - \alpha_2^3)(8\eta^3 - 12\eta^2 + 6\eta) + \alpha_2^3)\alpha_1^3 \alpha_2^3}{D_{EB}^h} \tag{125}$$

$$D_{EB}^h = 16\left(\left(\eta - \frac{1}{2}\right)^4 \alpha_2^6 - 2\eta\alpha_1^3\left(\eta - \frac{1}{2}\right)\left(\eta^2 - \frac{\eta}{2} + \frac{1}{2}\right)\alpha_2^3 + \alpha_1^6 \eta^4\right) \tag{126}$$

3.4 Methodology and Finite Element Analysis Procedures

Finite Element Analysis (FEA) was again used to simulate loading conditions. Again, as previously mentioned, simulations are an incredibly useful way to visualise how the structure will behave. To investigate the structural stability of the hexagonal design the three-dimensional design and engineering software, ANSYS was once again utilised.

3.4.1 Geometry of Beam Model

From the numerical analysis, as previously mentioned the dimensions were reformed as the cross-sectional area was redistributed. 6 different cases were modelled and simulated, the dimensions in each case are shown in table (3) (where all values are in millimetres):

Case	α_1	t_1	L_1	α_2	t_2	L_2
1	1.0	1.5	10	1.0	1.5	5
2a	1.3	1.95		0.7	1.05	
2b	1.2	1.8		0.8	1.2	
3a	0.8	1.2		1.2	1.8	
3b	0.7	1.1		1.3	2	
3c	0.5	0.75		1.5	2.3	

Table (3) The dimensions of the cases analysed

In cases where $t_1 > t_2$, this is considered as a step-up model whilst evidently for cases $t_2 > t_1$, this is considered as a step-down model. This is better depicted in fig. (28).

(a)

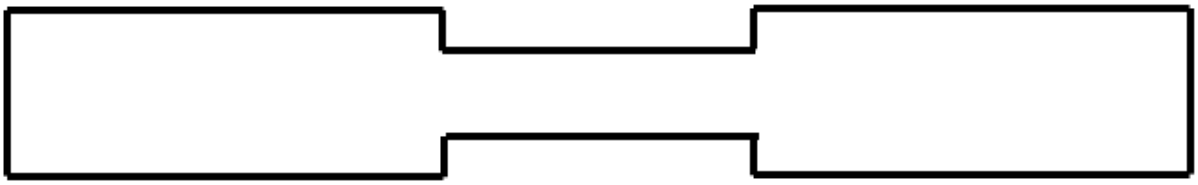

(b)

Fig. 28 (a) Schematic of step-up beam model i.e. where $t_1 > t_2$
Fig. 28 (b) Schematic of step-down beam model i.e. where $t_1 > t_2$

3.4.2 Geometry of Lattice Model

To create the lattice models, the beam elements for the 6 cases mentioned are repetitively made and combined to therefore develop tessellations. The lattice consists of 20-unit cells by 8 units. Fig. (29) shows the whole system of the lattice and how it has been built through the combinations of the cantilever beam and corresponding unit cells. And as these were only two dimensional, another dimension must be added for the simulation study and thus an extrusion of 1.5mm was applied.

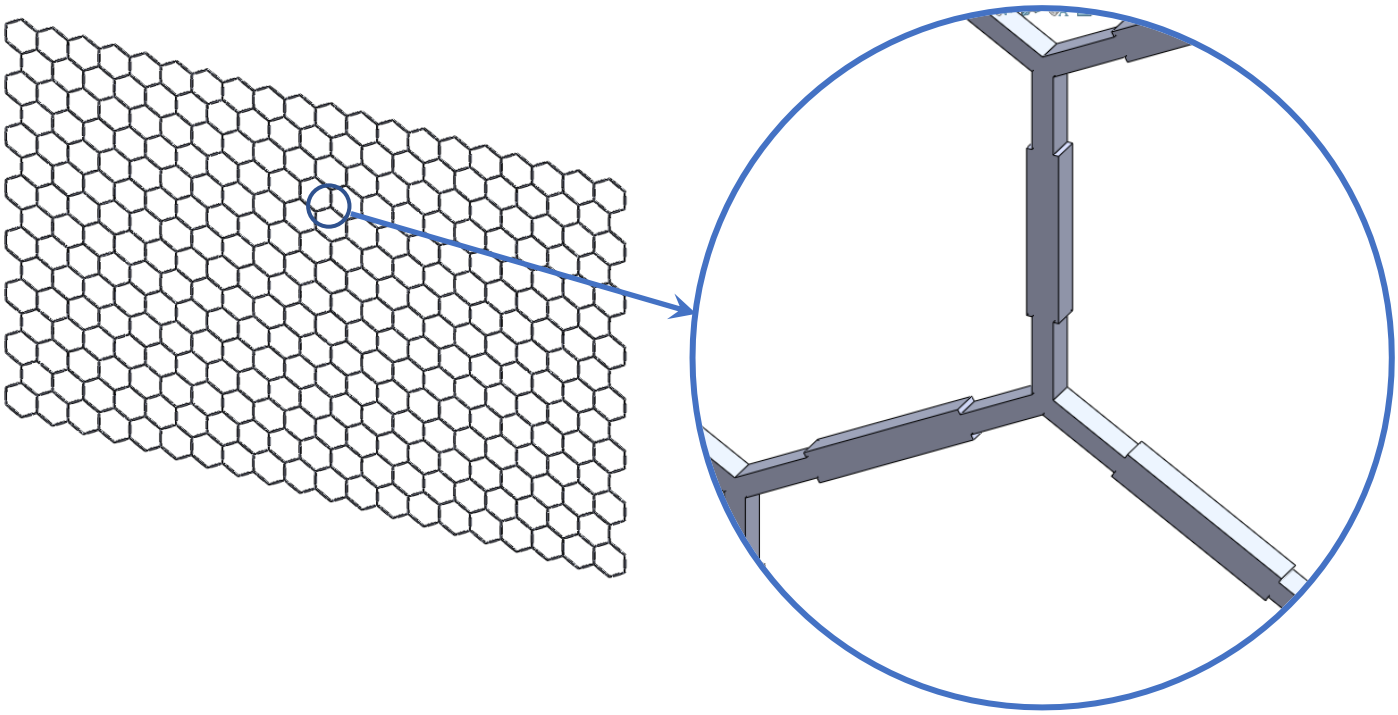

Fig (29). Stepped Lattice and a detailed view of its corresponding unit cell to show how the unit cell is multiplied and developed to make the whole system

3.4.3 Mesh Refinement of Lattice Model

For any and in this case, all the finite element analysis studies for the stepped and uniform lattice, it was important for a mesh refinement study to be conducted. This would ensure the reliability, validity and accuracy of the results produced by the static simulations. This was carried out in prior simulations in preceding chapters.

ANSYS has a convergence feature that can be applied to allow for an in-depth and detailed mesh that “adapts” to the complex geometry. This feature reduces the element size on the structure until the desired allowable change is achieved, 5% was chosen for all simulations, therefore conducting the mesh refinement study automatically. This procedure was utilised in all simulations conducted. Fig. 30 shows a less than 0.1% change in the 2 solutions therefore a more than sufficient mesh size has been chosen; this is further specified in Table (4).

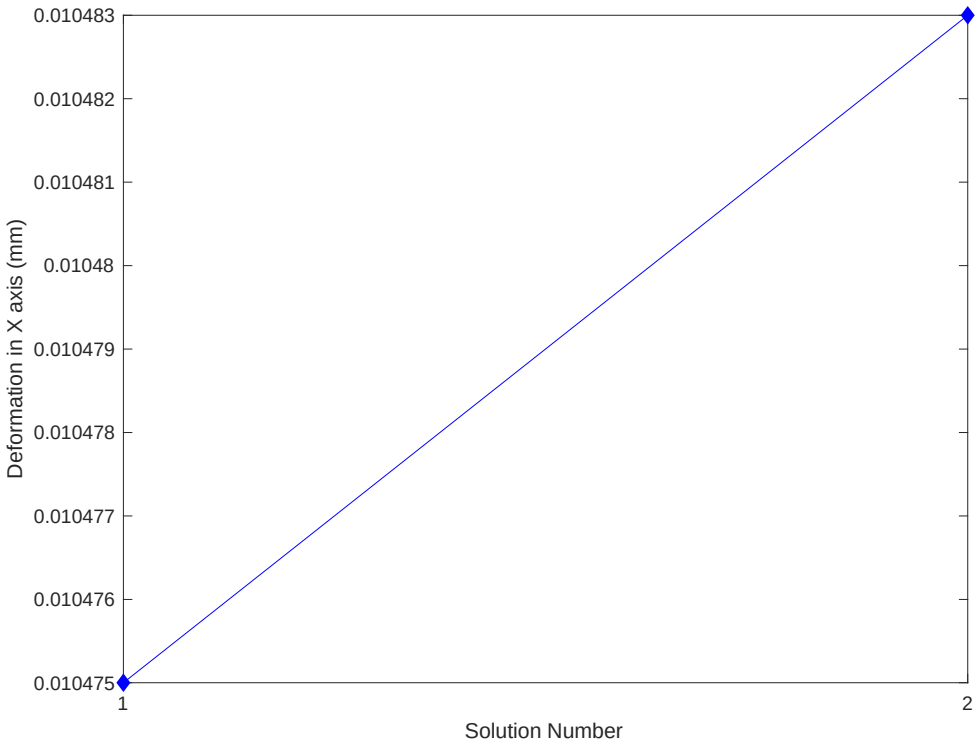

Fig. (30) Mesh Convergence Results for Case 2a

Solution Number	Deformation in X axis(mm)	Percentage Change in X axis deformation (%)	Number of Nodes	Number of Elements
1	0.010475	-	364821	100395
2	0.010483	0.076372	554310	294644

Table (4) Mesh Convergence Results for case 2a showing allowable change to be fulfilled

3.4.4 Lattice Simulation Set-Up

For the simulation of a lattice, the re-enactment of a simple general static analysis is conducted. The following initial external loads, fixtures and limitations were applied:

- Varying compressive magnitudes of force subjected on all faces of the right-hand side of the lattice in the x direction
- A fixed support on the left outer faces of the lattice
- Deformation in the z-axis is limited to a value of 0

As previously mentioned, the large deflection feature was also applied, meaning the change in stiffness due to change in the shape being tested were accounted for during analysis, therefore nonlinear analysis is being undergone.
This is better depicted in fig. (31).

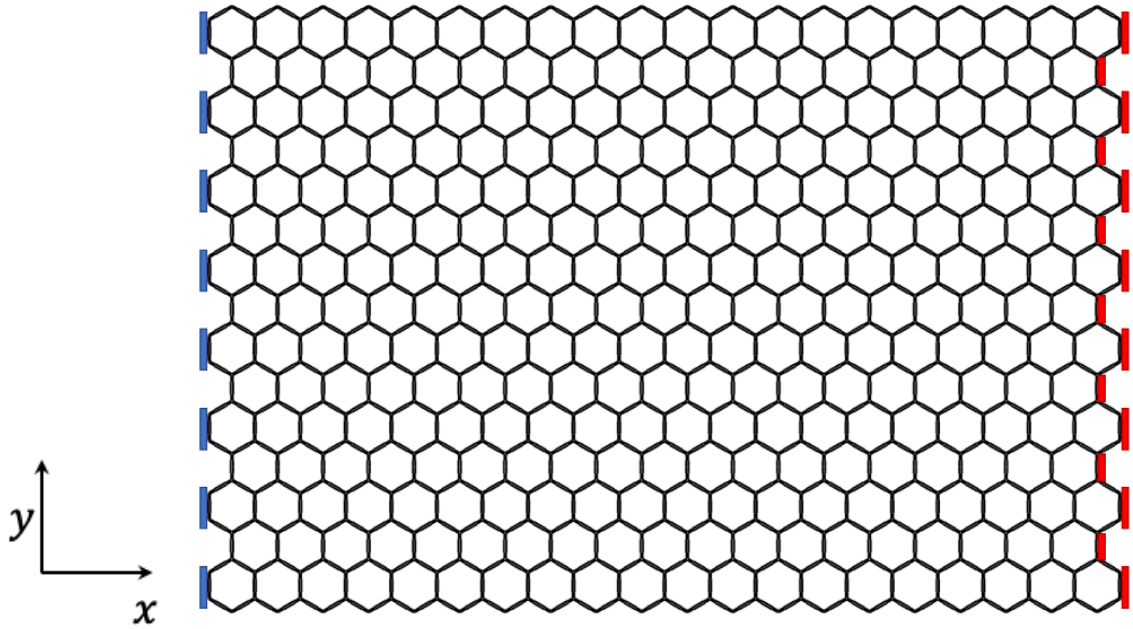

Fig. (31) The simulation set up of the lattices to be tested where the blue areas are where the fixed support was applied whilst the red cross-sectional areas represent where the magnitude of forces were subjected

The mechanical properties of structural steel were applied to the models. These were as follows:

Property	***Value***	***Units***
Elastic Modulus	200	GPa
Poisson's Ratio	0.3	-
Mass Density	7850	kgm^{-3}
Tensile Strength	250	MPa
Compressive Strength	250	MPa

Table (5) Mechanical Properties of Structural Steel

3.5 Discussion and Comparison of Numerical and Finite Element Results of Lattice

The displacements collected from the simulations were used to calculate the Young's modulus. The dimensions of the lattice after testing and the area in which the force was applied were also noted for the stiffness calculation. Basic structural mechanics equations (127), (128) and (129) were used for this computation.

$$\sigma = \frac{F}{A} \qquad (127)$$

$$\varepsilon = \frac{\Delta l}{l_0} \qquad (128)$$

$$E = \frac{\sigma}{\varepsilon} \qquad (129)$$

The representation of each symbol within these structural equations are as follows:

- σ – Stress
- F – Force
- A – Cross-sectional Area

- ε – Strain
- Δl – Deformation in Y Axis
- l_0 – Original Length of Lattice
- E – Transverse Young's Modulus

Fig. (32) shows plots of stress against strain for all cases mentioned. This stress dependency study shows the relationship between the stress and strain as a logarithmic curve for all cases.

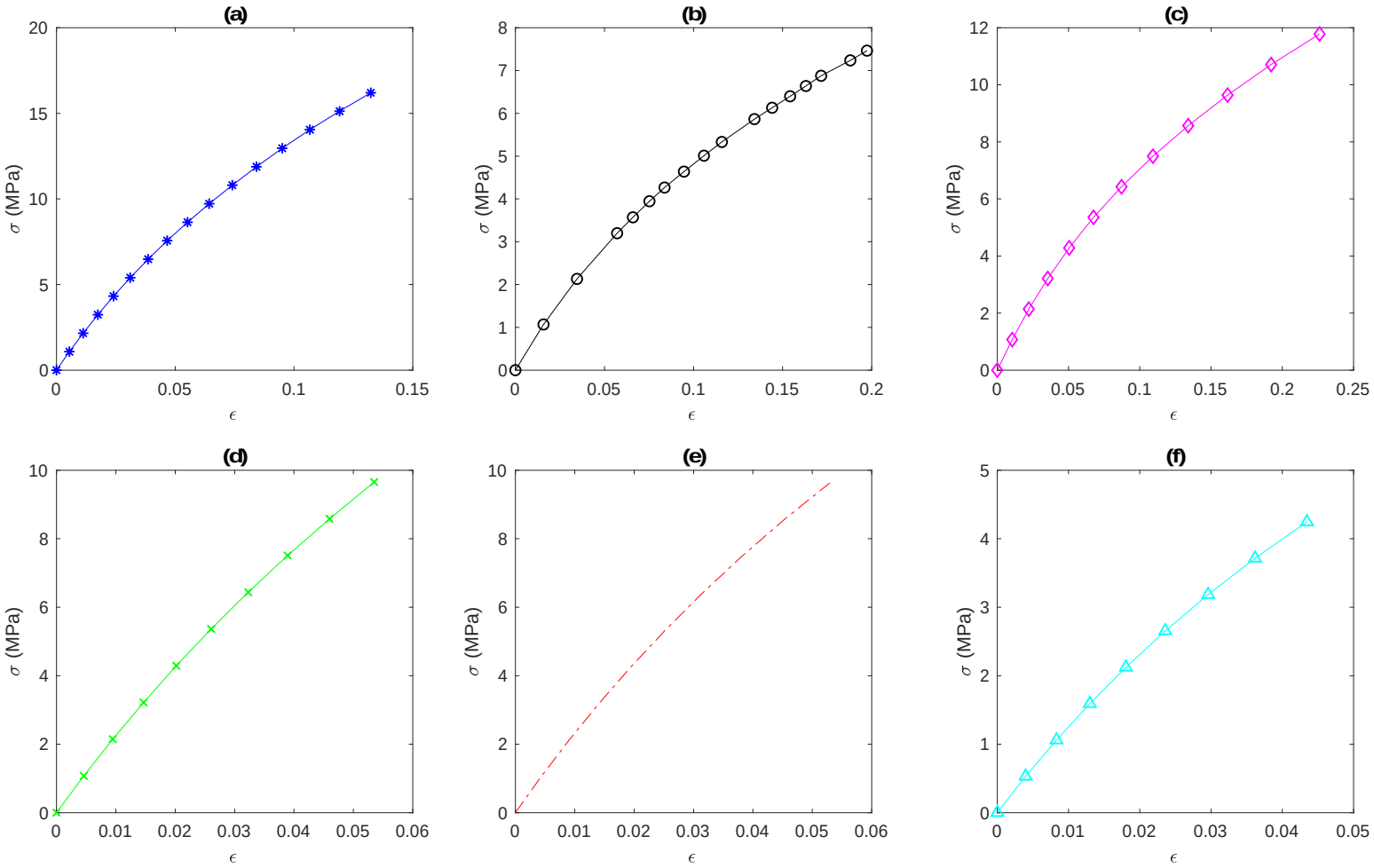

Fig (32):The relationship between the stress and strain for all cases
(a) Case 1 Results
(b) Case 2a Results
(c) Case 2b Results
(d) Case 3a Results
(e) Case 3b Results
(f) Case 3c Results

Fig. (32) displays the stress and strain results for all cases. A nonlinear relationship is shown for all cases.

Fig. (33) displays the results collected for both the numerical and finite element analysis of all cases mentioned but now plotting the young's modulus against the magnitude of force in which the lattice is subjected to. Since, the theoretical result does not depend upon the force or stress, this is seen as a single plot.

When comparing the numerical and finite element analysis values, generally it was found that with increasing stress comes with increasing percentage error. But oddly, for Case 1, when uniform lattice is subjected to a magnitude of 1 newton, the error percentage was found to be 6.85% whilst when subjected to 2000 newton this declined to 0.31% and then continually increased with increasing force.

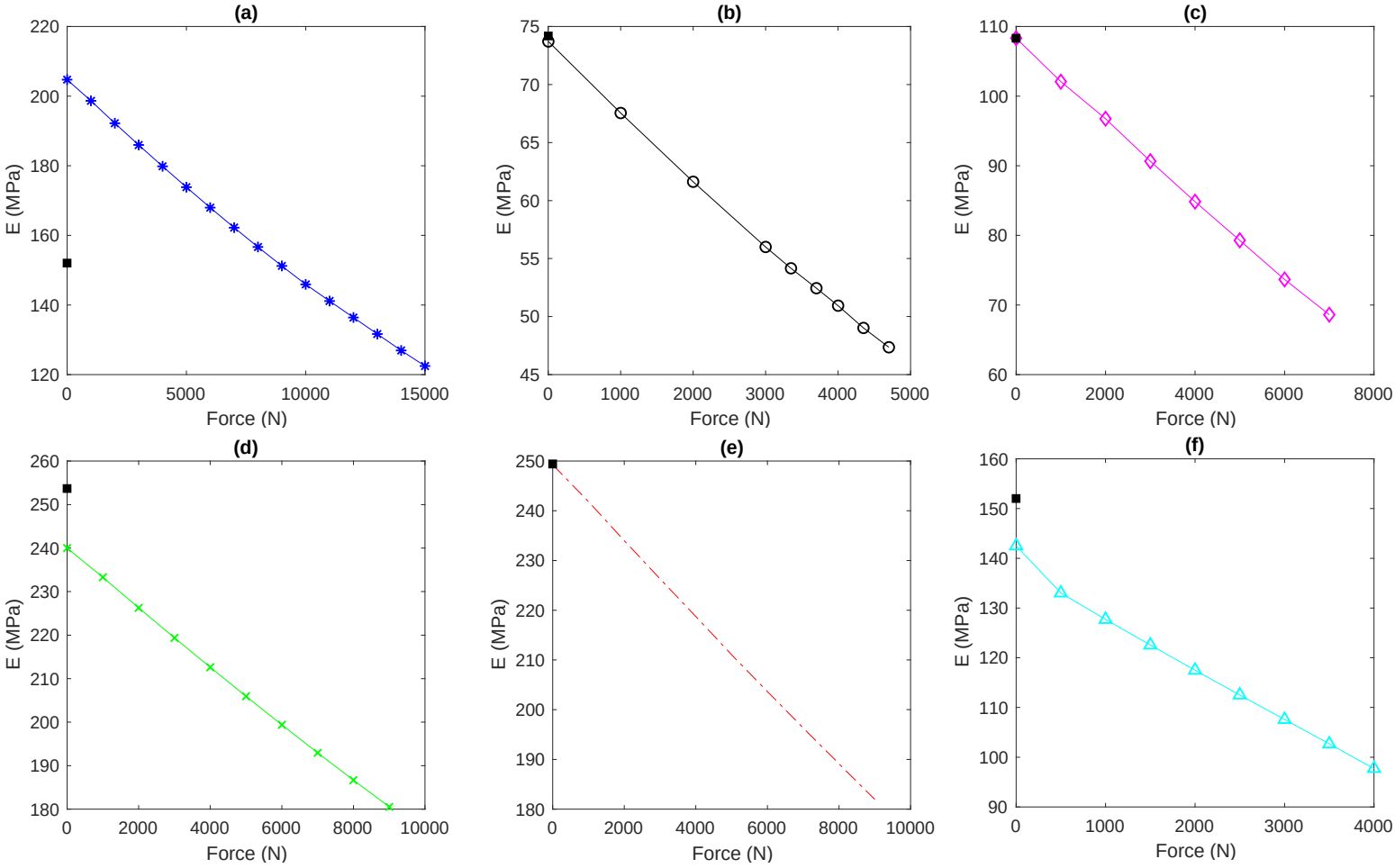

Fig (33): The finite results for all cases where the relationship is shown between the young's modulus and force whilst also a single plot is shown for the theoretical young's modulus value

(a) Case 1 Results
(b) Case 2a Results
(c) Case 2b Results
(d) Case 3a Results
(e) Case 3b Results
(f) Case 3c Results

	Young's Modulus		
Case	**Analytical Result (MPa)**	**FE Result when subjected to a 1 newton force (MPa)**	**Percentage Error**
1	191.62	204.740	6.85%
2a	74.189	73.716	0.64%
2b	108.32	108.322	0.002%
3a	253.69	240.005	5.39%
3b	249.42	249.266	0.062%
3c	152.02	142.481	6.28%

Table (6) Summarised Analytical and finite element results for all cases and their corresponding percentage errors

It is evident that the 'step-up' lattices have a lower Young's modulus value than the uniform cases whilst this varies in the 'step-down' configurations. It's found that for the step-down models, the young's modulus value was lower than the uniform structure whilst for step-up models this was significantly larger. This was particularly evident in cases 3a and 3b whilst for 3c was not the case. It's crucial to highlight that the lattice models' masses for all cases simulated differed on a minuscule scale. The magnitude of the largest difference was 2.23%.

3.6 Conclusions

A proposed approach to optimise the hexagonal configuration, with the aim of maximising the strength to weight ratio, has been investigated where 'steps' have been introduced. The stepped lattice has been developed by redistributing the cross-sectional area of the uniform lattice ensuring their equivalence. 6 models were specifically investigated further through modelling and running finite element analysis upon the structures. Table (6) summarises the results obtained from the analytical results as well as the finite element analysis. It can be observed from table (6) that the percentage error was found to be <6.28% therefore showing promising results that the numerical analysis has been conducted correctly. Case 3a was found to have the highest magnitude of the young's modulus with a value ~32% larger than the prismatic structure. The ratio between the minimum and maximum values of thickness parameters was therefore found to be optimal. Further investigation into the ideal parameter combinations could potentially offer a huge advancement in the manufacturing of additively manufactured structures.

Chapter 4 – Quadratic Profile

4.1 Introduction

Continuing from the previous chapter, this section of the paper of again focuses on the natural structure of the honeycomb configuration but a further look into the introduction of a quadratic profile for geometrical optimisation. For aerospace, weight reduction and deformation resistance enhancement are key to extensive applications, hence being the stimuli of the project. Similarly, to the preceding chapter, in this instance, the bottom-up approach is used. A cantilever beam is the first element to undergo analysis, then a unit cell (Y shaped segment), followed eventually by a complete complex system of an entire lattice. The obtained numerical theoretical results are then reviewed through ANSYS static structural simulations. This is naturally the extension of the analytical formulations that are established as it can represent the real-life model without compromising the cost of manufacturing and reduce the duration of attaining the results. The models used for the experiments are additively manufactured thus being another focus of this paper.

4.2 Numerical Analysis

4.2.1 Numerical Analysis of a Cantilever Beam

Following the bottom-up approach previously used in the first chapter, the honeycomb structure analysis involves splitting the structure into individual elements. And the first piece to be analysed is the cantilever beam. Fig. (34) displays the uniform prismatic structure whilst fig. (35) demonstrates the irregular altered beam. The dimensions applied to the optimised beam for the numerical analysis were as follows:

- Maximum Thickness (αt)
- Minimum Thickness (ηt)
- Length (L)

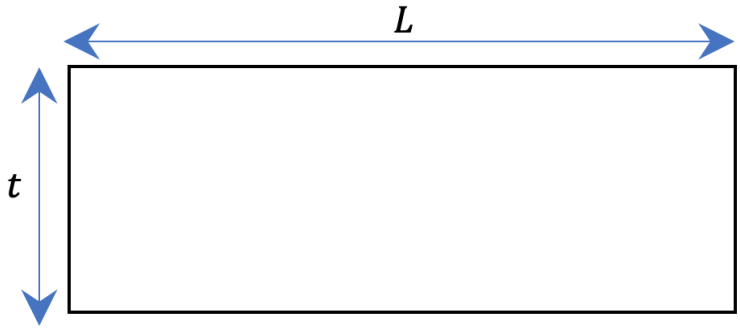

Fig. (34) Dimensions of Uniform Beam

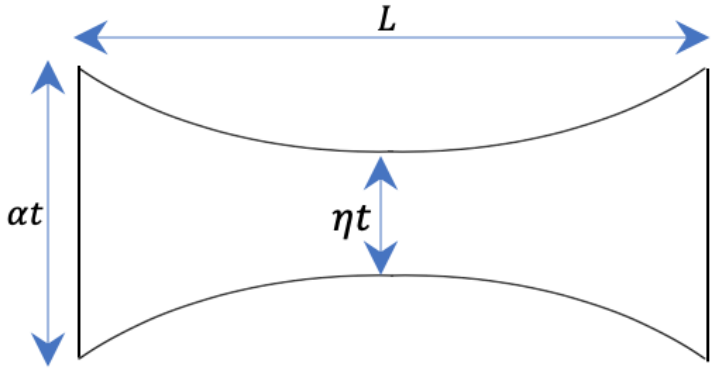

Fig. (35) Dimensions of Optimised Beam

For the attainment of theoretical values, boundary conditions were first introduced. These were based on the coordinates of the structure shown in fig. (36). It is also evident from fig. (36) that $\alpha > \eta$ and $t = 1 - \eta$.

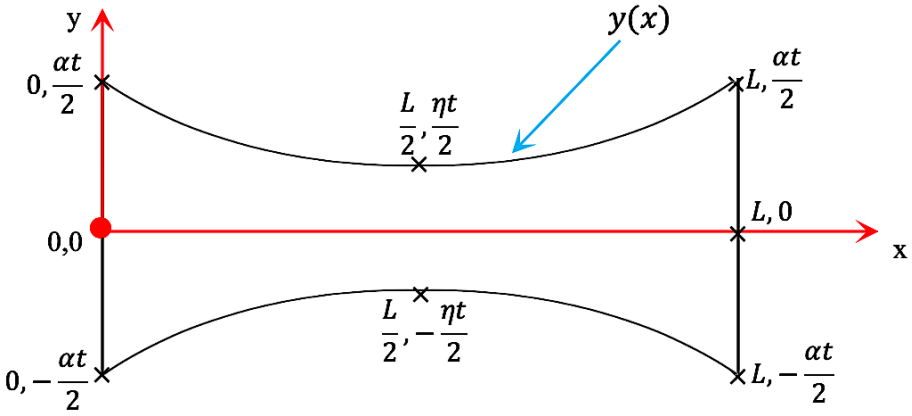

Fig. (36) Co-ordinates of Optimised beam with quadratic profile

These conditions were then used to obtain the quadratic equation, eq. (130):

$$y\,(x) = \frac{2t(\alpha-\eta)}{L^2}x^2 - \frac{2t(\alpha-\eta)}{L}x + \frac{\alpha t}{2} \qquad (130)$$

These boundary conditions also allowed the establishment of the unknown constants from the quadratic equations. Once this was achieved, it was critical to ensure the optimised structure and original beam cross-sectional areas were equal for comparison purposes as the structures would then sustain equivalent masses. Calculations were therefore formulated to fulfil this criterion. As seen in the equations (131), (132) and (133) below, an area condition was evaluated to sustain the masses of the beams as a control variable.

$$\int_0^L y(x)dx = \frac{tL}{2} \tag{131}$$

$$\frac{tl(\alpha + \eta^2)}{6} = \frac{tL}{2} \tag{132}$$

$$Area\ Condition: \alpha = 3 - 2\eta \tag{133}$$

For simplification purposes, η = 1 – ε was substituted into the equation (130). This created equation (134) for the final optimised dimension of the length in the irregular structure.

$$\boxed{y\,(x) = t\varepsilon\left(\frac{12}{L^2}x^2 - \frac{12}{L}x + 2\right) + t} \tag{134}$$

Further analysis was then conducted to find the optimal epsilon value where peak strength is found when the edge of the beam is subjected to a force, P which can be seen in fig. (37). The equation for rotation due to bending moments and displacement were used to derive the optimal epsilon value through basic calculus. Thus, the properties of the uniform beam structure are then found through equations (135) and (136).

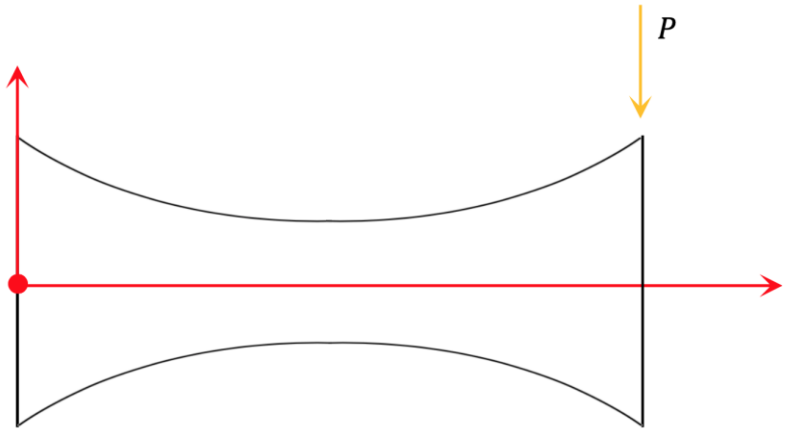

Fig. (37) Non-uniform beam subjected to a downwards force, P.

$$\theta(x) = \int \frac{M(x)}{EI(x)} dx = \frac{P\left(lx - \frac{1}{2}x^2\right)}{EI} \tag{135}$$

$$\delta(x) = \int \theta(x) = \frac{P\left(\frac{1}{2}lx^2 - \frac{1}{6}x^3\right)}{EI} \tag{136}$$

For the nonuniform structure, the same integration process was followed as seen in equation (137) and (138).

$$\theta(x) = \int \frac{M(x)}{EI(x)} dx = \frac{P(L-x)}{EI\left(\varepsilon\left(\frac{12x^2}{L^2} - \frac{12x}{L} + 2\right) + 1\right)^3} \tag{137}$$

$$\delta(x) = \int \theta(x) = \int \frac{P(L-x)}{EI\left(\varepsilon\left(\frac{12x^2}{L^2} - \frac{12x}{L} + 2\right) + 1\right)^3} \tag{138}$$

Equations (137) and (138) were evaluated and used to obtain stiffness coefficients with appropriate boundary conditions. To ensure the correct equations were acquired, the epsilon value of 0, corresponding to the uniform structure, was substituted into equations (137) and (138). The results were then compared to the results from equations (135) and (136), where their equality is a criterion to be fulfilled.

4.2.2 Numerical Analysis of the Unit Cell and Lattice

The next segment in the study procedure to be analysed constitutes of three beam elements combined to make the unit cell as discussed in previous chapters. Each beam element is treated as beams of thickness (t), depth (b), length (l) at an inclined angle (θ).

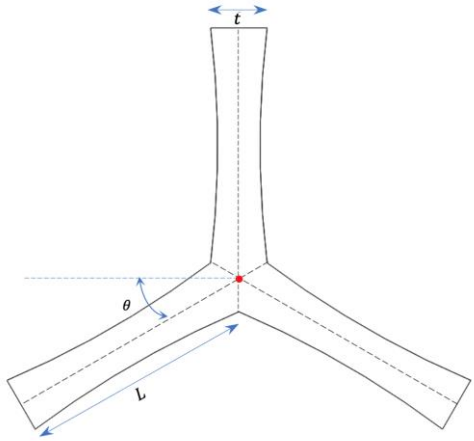

Fig. (38) Dimensions and geometry of Unit Cell with epsilon value of 0.1

For the unit cells analysed, the inclined angle is at an obligatory 30°, but necessary changes could be made to the derivations if θ ≠ 30°. The numerical analysis of the unit cell consists of formulating the individual cantilever beams' local stiffness matrices and transforming them into a global coordinate system which in this case represents the lattice. The equations of the whole complex system of the lattice are thus derived from the unit cell. The beam stiffness matrix can be expressed by equation (139). Periodic boundary conditions were applied for a minimum number of unit cells. These are a set of boundary conditions chosen and applied to enable the approximation of a larger system (which in this case is the lattice) from the unit cell i.e. the deformation of one-unit cell occurs, all the other unit cells deform in the same manner within the lattice.

$$K_e = \begin{bmatrix} \frac{12}{L^3} & \frac{6}{L^2} & -\frac{12}{L^3} & \frac{6}{L^2} \\ \frac{6}{L^2} & \frac{4}{L} & -\frac{6}{L^2} & \frac{2}{L} \\ -\frac{12}{L^3} & -\frac{6}{L^2} & \frac{12}{L^3} & -\frac{6}{L^2} \\ \frac{6}{L^2} & \frac{2}{L} & -\frac{6}{L^2} & \frac{4}{L} \end{bmatrix} \quad (139)$$

$K_{5,5}$ represents one of the stiffness matrix coefficients needing to be established as it is used in Young's modulus calculations. The stiffness coefficients and their ratios are first found for the uniform structure.

$$K_{55} = \frac{Ebt^3}{L^3} \tag{140}$$

$$K_{44} = \frac{Ebt}{L} \tag{141}$$

$$K_{44h} = \frac{Ebt}{h} \tag{142}$$

$$R_1 = \frac{K_{55}}{K_{44}} = \frac{t^2}{L^2} \tag{143}$$

$$R_2 = \frac{K_{55}}{K_{44h}} = \frac{t^2 h}{L^3} \tag{144}$$

The same formulation process is followed for the irregular altered structure as seen in equations (145) – (149).

$$K_{55} = \frac{8Eb^3(\varepsilon-1)^{\frac{3}{2}}\varepsilon^{\frac{3}{2}}(2\varepsilon+1)^2}{L^3\left(4\left(\varepsilon+\frac{1}{2}\right)^2\sqrt{3}\tanh^{-1}\left(\sqrt{\frac{3\varepsilon}{\varepsilon-1}}\right)+\sqrt{\varepsilon-1}\left(\sqrt{\varepsilon}-4\varepsilon^{\frac{3}{2}}\right)\right)} \tag{145}$$

$$K_{44} = \frac{Ebt\sqrt{3\varepsilon(\varepsilon-1)}}{L\tanh^{-1}\left(\sqrt{\frac{3\varepsilon}{\varepsilon-1}}\right)} \tag{146}$$

$$K_{44h} = -\frac{Ebt\sqrt{3\varepsilon(\varepsilon-1)}}{h\tanh^{-1}(\left(\sqrt{\frac{3\varepsilon}{\varepsilon-1}}\right)} \tag{147}$$

$$R_1 = \frac{K_{55}}{K_{44}} = \frac{8(\varepsilon-1)\varepsilon\left(\varepsilon+\frac{1}{2}\right)^2 t^2 \tanh^{-1}\left(\sqrt{\frac{3\varepsilon}{\varepsilon-1}}\right)\sqrt{3}}{L^2\left(\left(\varepsilon+\frac{1}{2}\right)^2\sqrt{3}\tanh^{-1}\left(\sqrt{\frac{3\varepsilon}{\varepsilon-1}}\right)+\frac{3\sqrt{\varepsilon-1}\left(\sqrt{\varepsilon}-4\varepsilon^{\frac{3}{2}}\right)}{4}\right)} \quad (148)$$

$$R_2 = \frac{K_{55}}{K_{44h}} = \frac{32\sqrt{3}(\varepsilon-1)\tanh^{-1}\left(\sqrt{\frac{3\varepsilon}{\varepsilon-1}}\right)\varepsilon t^2 h\left(\varepsilon+\frac{1}{2}\right)^2}{3L^2\left(\frac{4\left(\varepsilon+\frac{1}{2}\right)^2\sqrt{3}\tanh^{-1}\left(\sqrt{\frac{3\varepsilon}{\varepsilon-1}}\right)}{3}+\sqrt{\varepsilon-1}\left(\sqrt{\varepsilon}-4\varepsilon^{\frac{3}{2}}\right)\right)} \quad (149)$$

The formulation for $K_{5,5}$ was simplified to obtain equations (150) and (151). These formulae, equations (150) and (151), are equal but consisting of different variables [11].

$$E_{1R} = \frac{\left(24(cos\theta^2-1)\right)(2\varepsilon+1)^2\varepsilon^{\frac{3}{2}}(\varepsilon-1)^{\frac{3}{2}}\alpha^3 E}{\left(32\sqrt{3}\left(\varepsilon+\frac{1}{2}\right)^2\left(-\frac{1}{8}+(\alpha^2\varepsilon^2-\alpha^2\varepsilon+\frac{1}{8}cos(\theta)^2\right)\tanh^{-1}\left(\sqrt{\frac{3\varepsilon}{\varepsilon-1}}\right)+3\sqrt{\varepsilon-1}(cos(\theta)-1)(cos(\theta)+1)\left(\sqrt{\varepsilon}-4\varepsilon^{\frac{3}{2}}\right)\right)} \quad (150)$$

$$E_{1r} = \frac{\left(6(cos\theta^2-1)\right)(2\varepsilon+1)^2\varepsilon^{\frac{3}{2}}(\varepsilon-1)^{\frac{3}{2}}t^3 E}{L\left(-3L^2(cos(\theta)-1)\left(\varepsilon^{\frac{3}{2}}-\frac{\sqrt{\varepsilon}}{4}\right)(cos(\theta)+1)\sqrt{\varepsilon-1}+\left(\left((8\varepsilon^2-8\varepsilon)t^2+L^2\right)cos\theta^2-L^2\right)\left(\varepsilon+\frac{1}{2}\right)\sqrt{3}\tanh^{-1}\left(\sqrt{\frac{3\varepsilon}{\varepsilon-1}}\right)\right)} \quad (151)$$

Similar to the cantilever beam numerical analysis, the epsilon value of 0 was substituted into the stiffness coefficient and ratio formulas. These were then compared to the uniform case values to verify their equality, if this condition was fulfilled this would imply the correct equations were obtained.

4.3 Methodology and Finite Element Analysis Procedures

Finite Element Analysis (FEA) was again used to simulate loading conditions and determine the deformation experience by the beam in y axis. Again, as previously mentioned, simulations are an incredibly useful way to visualise how the structure will behave. To investigate the

structural stability of the hexagonal design the three-dimensional design and engineering software, ANSYS was once again utilised.

4.3.1 Geometry of Beam Model

From the numerical analysis, the dimensions were reformed by introducing a quadratic curve function. This was applied to the length of the beam. For the model to be simulated, the dimensions were as follows:

- length *(l)* = 20mm
- Thickness *(t)* = 2mm

Both values were then substituted to easily simplify equation (134) into equation (152).

$$y = 0.06\varepsilon x^2 - 1.2\varepsilon x + 4\varepsilon + 12 \tag{152}$$

A variety of epsilon values were also substituted to create several models ready to be structurally analysed and compared. As these were only two dimensional, another dimension must be added for the simulation study and thus an extrusion of 20mm was applied.

4.3.2 Mesh Refinement Study of Beam Model

Again, for all the finite element analysis studies conducted in this optmisation, it was again crucial to conduct a mesh refinement study as mentioned previously. For the cantilever beam, the deformation experienced by the beam in the y axis was recorded. It was assumed that the optimal mesh size differed for each beam since the complexity of each model differed.

Another software, Solidworks, much like ANSYS can be used to run these simulations where a curvature mesh can be applied. This would allow the mesh to account for the geometrical intricacy of the design. But a huge difference between software is that ANSYS has a convergence feature which allows for an in-depth and detailed mesh that “adapts” to the intricacy or simplicity of the geometry. This feature continues to reduce the element size on the structure until the desired allowable change is achieved. Again, 5% was chosen for all simulations, therefore conducting the mesh refinement study automatically. This procedure was utilised in all simulations conducted.

This is completely different to Solidworks as both the minimum and maximum element sizes can be defined for the curvature mesh mentioned. The use of various elements' sizes would therefore increase the accuracy of the results. The aim for the mesh refinement is to find a convergence for the displacements which as mentioned, ANSYS can achieve automatically. Once this was attained, the optimal mesh to be used for the geometry can be easily determined. This is ultimately how a mesh study is conducted manually.

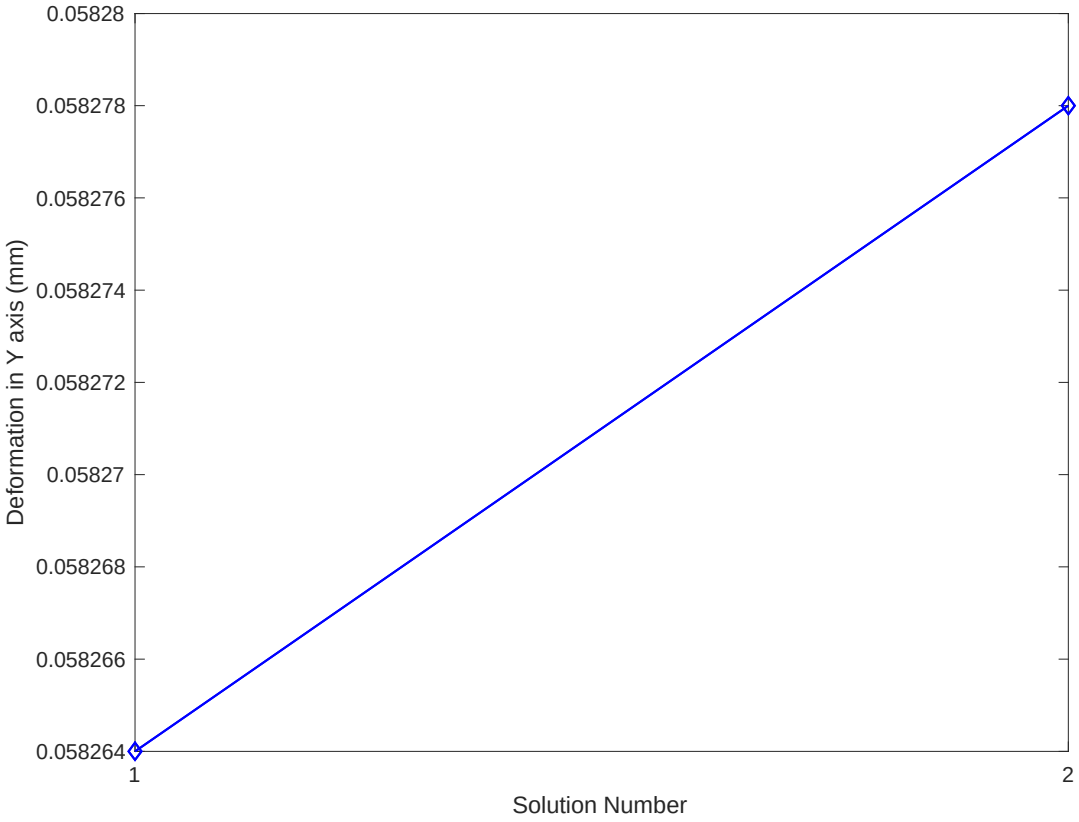

Fig. (39) Mesh Convergence Results for Epsilon=0

Solution Number	Directional Deformation (mm)	Change (%)	Number of Nodes	Number of Elements
1	0.058264	-	26745	13134
2	0.058278	0.22772	80596	47081

Table (7) Mesh Convergence Results for epsilon =0 showing allowable change to be fulfilled

4.3.3 Cantilever Beam Simulation Set-Up

For the simulations, a single vertical downward force was applied on the edge of each beam, ranging from 50 newtons to 500 newtons in 50 newton increments. A fixed geometry was then applied to the opposite end and face of the beam. It is also important to note that the displacements experienced in the z-axis were fixed to a value of zero since this is an in-plane analysis. With this set-up, its replication of a general linear static analysis of a simple cantilever beam was established.

The average deformation experienced by the elements of the opposite face of the fixture in the Y axis was recorded. The mass of each of the structures was observed, ensuring their equivalence. This is particularly important for comparison purposes. Through these simulations, it can be determined whether the model with the found optimal epsilon value can not only be applied mathematically but in real life models.

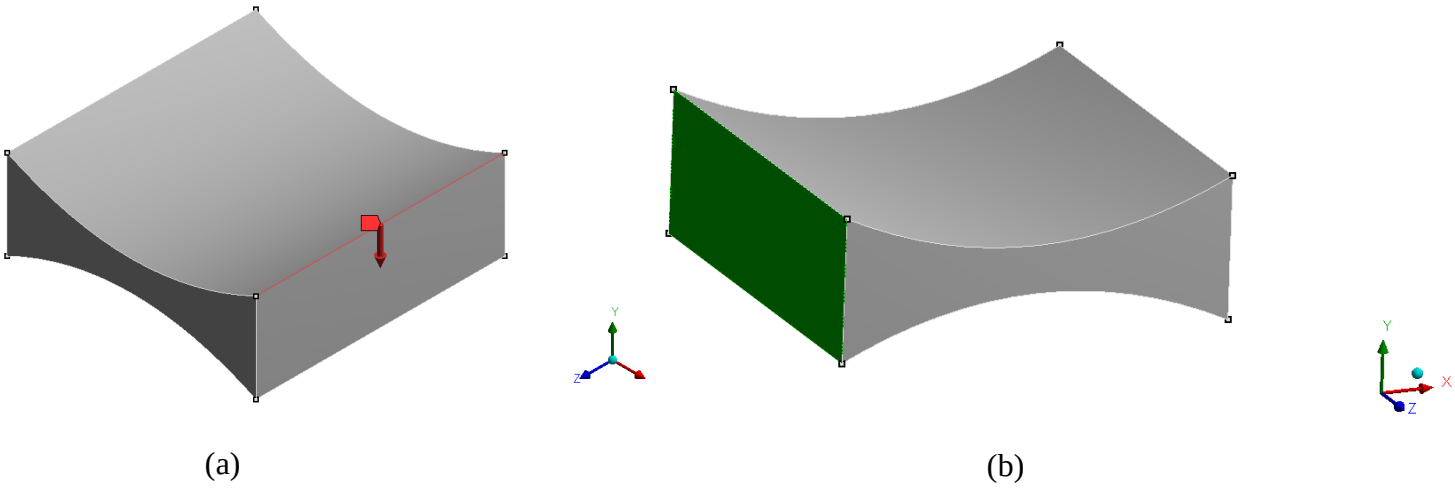

(a) (b)

Fig (40) (a) Arrow indicating where force is applied on a beam model with an epsilon value of 0.4

Fig. (4) (b) Beam model with an epsilon value of 0.4 where the green covered face area indicates the location in which the fixed support is applied

The mechanical properties of structural steel were applied to the models. These were as follows:

Property	***Value***	***Units***
Elastic Modulus	200	GPa
Poisson's Ratio	0.3	-
Mass Density	7850	kgm^{-3}
Tensile Strength	250	MPa
Compressive Strength	250	MPa

Table (8) Mechanical Properties of Structural Steel

4.3.4 Geometry and Mesh Study of Unit Cell

Following on from the reformed beam with a quadratic curve, this is then expanded into the unit cell consisting of three cantilever beams. As previously mentioned, the inclined angle is by default 30 degrees to create this 'Y' segment that we call the unit cell. The same quadratic curve formulations from the beam elements are applied to the unit cell whilst this time, the depth of the unit cell has been reduced to 10mm. Furthermore, the identical procedure applied to the beam was conducted in terms of mesh following through with the convergence feature to optimise the accuracy of the results.

4.3.5 Unit Cell Simulation Set-Up

To replicate the beam's linear static analysis, a fixed support was applied to the top face of the middle beam element and the edge of inclined beams were subjected to forces with a magnitude of 500N. As previously mentioned, as this is an in-plane analysis, the deformation experienced in the z-axis direction is set to 0. This is better demonstrated in fig. (41). The average y axis deformation experienced by the faces of the inclined beams were recorded.

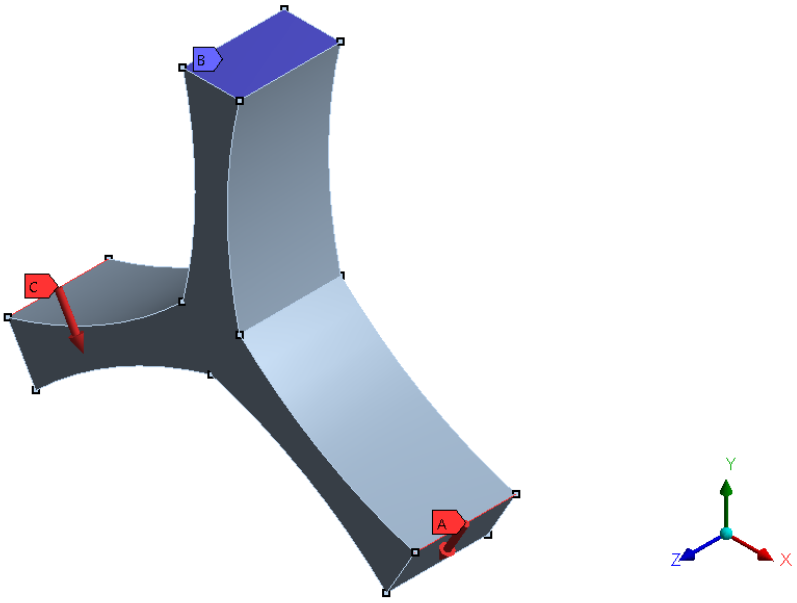

Fig. (41) Simulation set up of unit cell model with epsilon value of 0.2 where the blue covered face indicates where the fixed support has been applied and the red arrows indicating where the fore is subjected upon.

The masses of these various unit cell models were again monitored, as their inequivalence would mean the models are incomparable. It was found that the masses were different where the mass would increase with increasing epsilon value. To enforce control measures, the forces applied to the unit cells were adjusted according to their mass. The force and mass implemented to the uniform structure were arranged into an equation to create a constant as seen in eq. (X). The various epsilon values of the models were represented by 'n' in this equation and '0' represented the uniform case. The adjusted values of force according to the masses of the models can be seen in table (9).

$$\frac{F_0}{m_0} = \frac{F_n}{m_n}$$

Epsilon Value	Mass (g)	Force (N)
0	19.38	500.00
0.01	19.41	500.57
0.02	19.43	501.14
0.03	19.45	501.73
0.04	19.47	502.33
0.05	19.50	502.95
0.06	19.52	503.57
0.07	19.55	504.20

0.08	19.57	504.85
0.09	19.60	505.50
0.1	19.62	506.17
0.2	19.91	513.47
0.3	20.23	521.88
0.4	20.60	531.42
0.5	21.02	542.09
0.6	21.47	553.87
0.7	21.97	566.78
0.8	22.52	580.81
0.9	23.10	595.96

Table (9) Varying Epsilon values and their respective masses and forces in which they are subjected to

The mechanical properties of structural steel, shown in table (7), were again applied to this set of models.

4.3.6 Geometry and Mesh Refinement Study of Lattice Model

The complete system of an entire lattice is last to be analysed. The lattice consisted of 20-unit cells by 8 units. Fig. (42) shows the whole lattice and how it has been built through the combinations of the cantilever beam and unit cells.

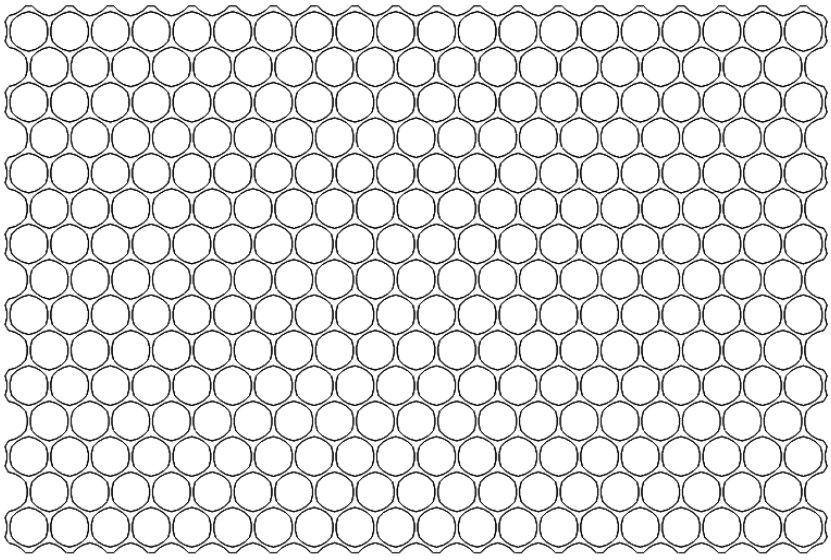

Fig. (42) Model of Lattice with ε=0.3136

4.3.7 Lattice Simulation Set-Up

To re-enact the same structural test undergone by the beam and unit cell for the optimised lattice, the following initial external loads, fixtures, and limitations were applied:

- 50N force subjected on all bottom faces of the lattice.
- A fixed support was applied on the top faces of upper cells of the lattice
- Deformation in the z-axis is limited to a value of 0

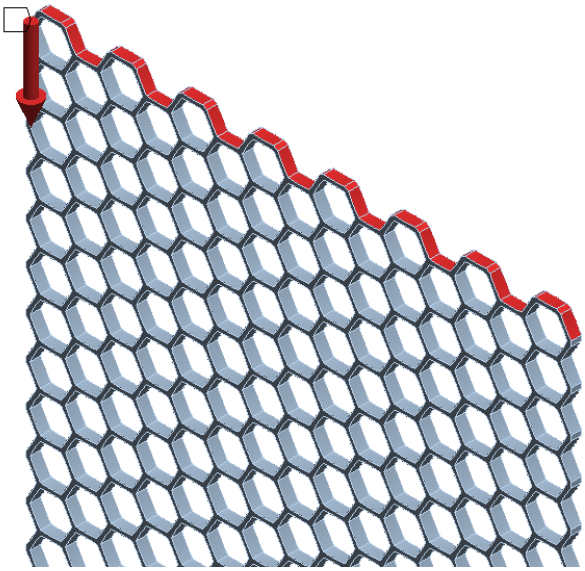

Fig. (43) Faces of Lattices indicated by blue covered area that are subjected to compressive forces

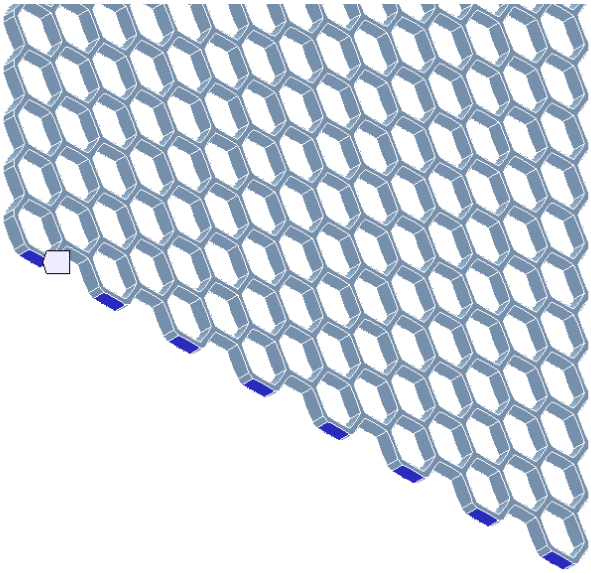

Fig. (44) Faces of Lattices with fixed supports

Again, it was essential to pay attention to the mass of the lattices as if these were not identical, the lattices are not comparable. It was found that the masses were in fact different just like the preceding case; the masses increased as the epsilon value increased which is not ideal. Identical control measures applied to the unit cell were applied to the complex system of the lattice.

Epsilon Value	**Force (N)**
0	50.000000000
0.01	50.114210641
0.02	50.230681414
0.03	50.349413055
0.06	50.719174516
0.1	51.243919898
0.2	52.713936706
0.3136	54.658347162
0.4	56.332659702
0.5	58.481142789
0.6	60.855778304

Table (10) Magnitude of forces applied to lattice models dependent on each value of epsilon

Property	***Value***	***Units***
Elastic Modulus	2.96	GPa
Poisson's Ratio	0.37	-
Mass Density	1420	kgm^{-3}
Tensile Strength	57.3	MPa
Compressive Strength	92.9	MPa
Thermal Conductivity	0.261	W/mK
Specific Heat	1140	J/kgK

Table (11) Mechanical Properties of PET

For future research comparison purposes, the mechanical properties of a material called polyethylene terephthalate (PET) were applied to the lattice models. This was applied as it was readily available for printing in the experimental stage, the values are then easily comparable to real life models due to the similarities in mechanical properties.

4.4 Discussion and Results

4.4.1 Discussion and Comparison of Beam Element Results

Fig. (45) illustrates the results collected for the numerical analysis of the cantilever beam where D_0/D_n represents the ratio of displacements experienced by the uniform beam to the displacement of the altered cantilever beam . Similarly, the influence of epsilon on the y axis displacement from the simulation results are shown in table (12). It can evidently be seen that the curvatures created by both methods are extremely alike. As expected, both graphs experience a declination of vertical displacement before escalating.

The displacement is minimal at slightly different values of epsilon; the numerical analysis found the optimal value of epsilon to be 0.06086460418 whilst in the simulations, it was found to be around 0.06. Therefore, showing an 98.6% margin of accuracy.

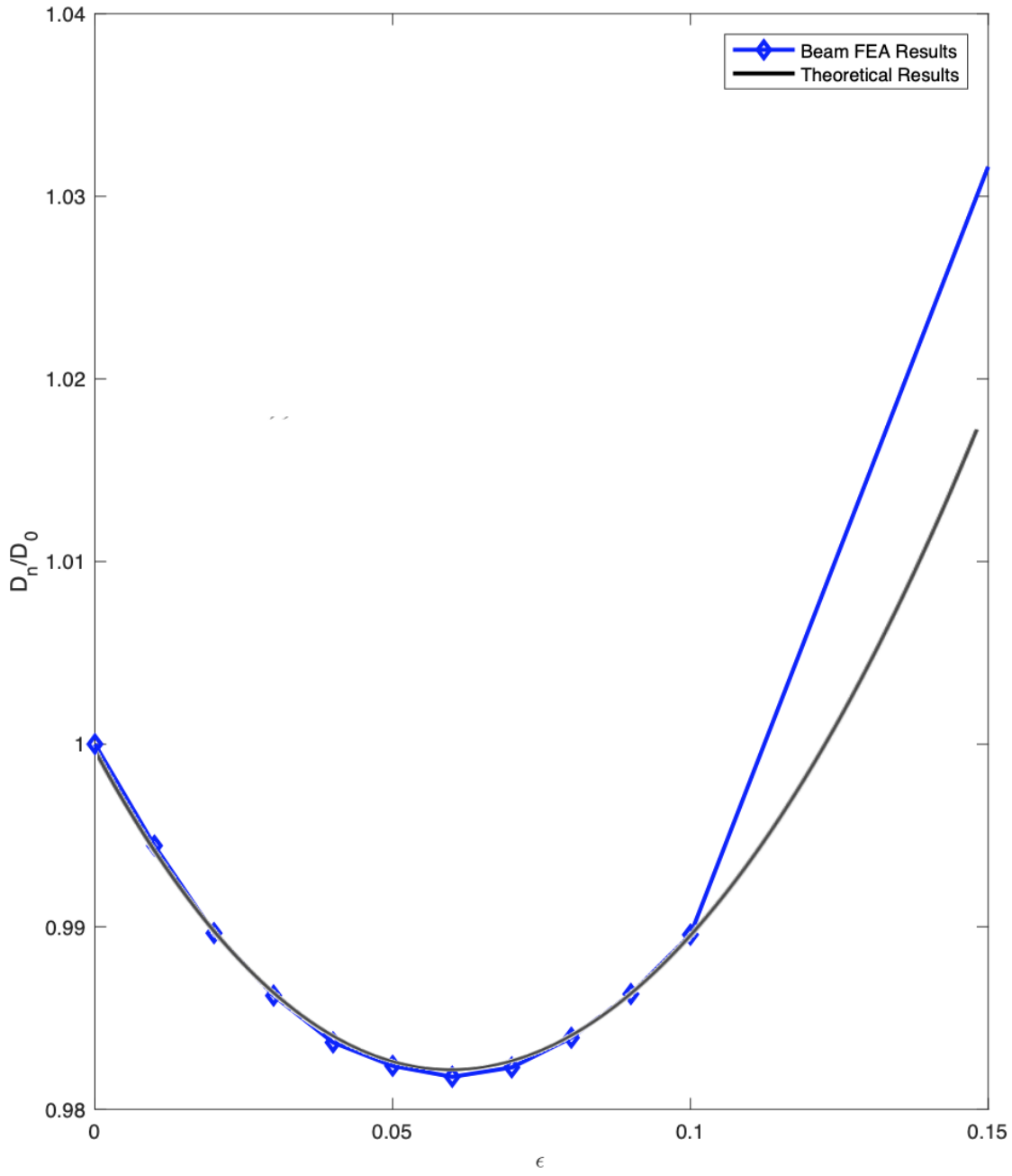

Fig. (45) Numerical and Finite Element Analysis Results

Table (12) displays the simulations results when a force of 100N is subjected upon the beam. It can also be clearly seen that the masses of all the models with varying epsilons are identical, allowing for their comparison. The original uniform structure displaced by 0.011691mm whilst at the optimal value of 0.06, displaced at a decreased value of 0.011478mm. This demonstrates a promising ~1.02% increase in structural stability.

Epsilon Value	Mass (g)	Force (N)	Displacement (mm)	D_n/D_0
0	12.56	100	0.011691	1.000000
0.01			0.011626	0.994440
0.02			0.011570	0.989650
0.03			0.011530	0.986229
0.04			0.011500	0.983663
0.05			0.011485	0.982380
0.06			0.011478	0.981781
0.07			0.011484	0.982294
0.08			0.011503	0.983919
0.09			0.011531	0.986314
0.1			0.011569	0.989565
0.2			0.012552	1.073646
0.3			0.014759	1.262424
0.4			0.018791	1.607305
0.5			0.026107	2.233085
0.6			0.040718	3.482850
0.7			0.075462	6.454709
0.8			0.190320	16.279189
0.9			1.036600	88.666496

Table (12) Finite Element Analysis results when a force of 100N is subjected upon the beam models

4.4.2 Discussion of Unit Cell Results

The ratio of displacements was also found in this case, seen in table (13). Similarly, the influence of epsilon value on the y axis displacement from the simulations results are shown in fig. (46) and table (13).

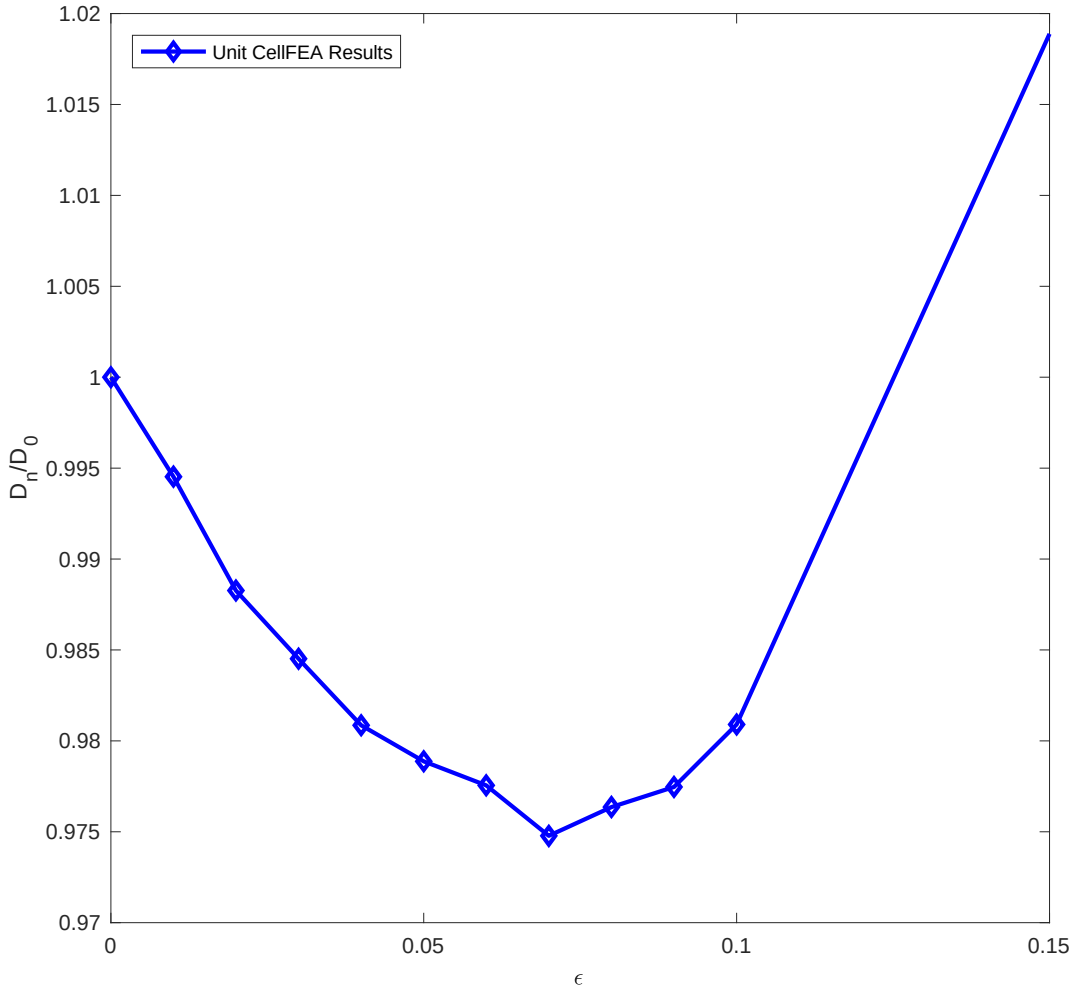

Fig. (46) Results of Unit Cell Models where the ratio of the uniform unit cell deformation

Epsilon Value	Average Y Displacement	Dn/D0
0	0.113380	1.000000
0.01	0.112760	0.995849
0.02	0.112050	0.990374
0.03	0.111625	0.985605
0.04	0.111210	0.982602
0.05	0.110985	0.980041
0.06	0.110835	0.977303
0.07	0.110520	0.975007
0.08	0.110700	0.977215
0.09	0.110825	0.979776
0.1	0.111215	0.982690
0.2	0.119825	1.057670
0.3	0.140430	1.239601
0.4	0.179795	1.588802
0.5	0.253485	2.234214
0.6	0.414095	3.631370
0.7	0.783200	6.830522
0.8	2.112950	18.679679
0.9	-	-

Table (13) Results from Finite Element Analysis of the Unit Cell

It is evident that the deformation decreases with increasing epsilon value until a specific point where the displacement starts to increase once again. This point where minimum displacement was achieved, was at the epsilon value of around 0.07. In comparison to the beam element results, this is within a reasonable range. But this is expected as the simulations conducted for the unit cell were methodised to replicate the structural analysis undergone by the beam element.

4.4.3 Discussion and Comparison of Numerical and FEA Results of Lattice

The displacements collected from the simulations were used for the Young's modulus calculation. The dimensions of the lattice after testing and the area in which the force was applied were also noted for the stiffness calculation. Basic structural mechanics equations (127), (128) and (129) were used for this computation.

Fig. (47) displays the results collected for both the numerical and finite element analysis of the lattice. The trends in both analysis results indicates that the ratio of the prismatic young's modulus to the optimised structures' young's modulus (E_n/E_0) increases with rising values of epsilon but reaches a point where a sudden decrease occurs.

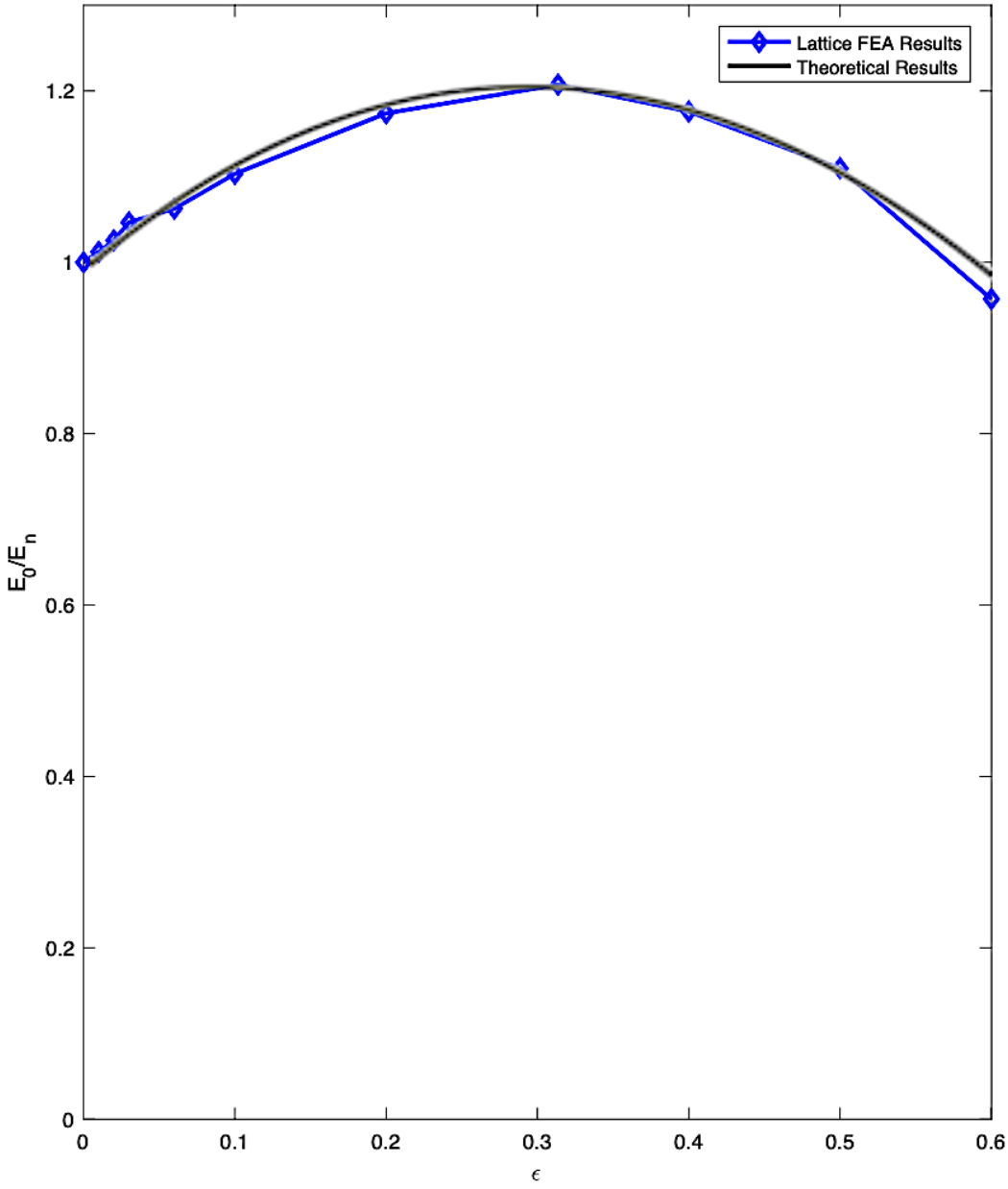

Fig. (47) Finite Element Results of Lattice Models where the ratio of Young's Modulus for the uniform model and altered model is plotted again the epsilon value corresponding to individual lattice models

The curvatures created by both methods are extremely alike where the peak of the Young's modulus ratio occurs at the epsilon value of 0.3136 in both the numerical and finite element analysis.

4.5 Conclusions

The detailed analysis of a natural design, the honeycomb structure, was investigated with the aim of optimising the structure's resistive capabilities to deformation. The analysis was conducted by following the bottom-up approach and two different methods: numerical and finite element analysis. It can be observed from fig. (47) that the mechanical properties in the lattice where $\varepsilon = 0.3136$ performed better than the original prismatic structure where $\varepsilon = 0$. Through these two different methods, it was found that the optimised structure can resist the occurrence of elastic deformation by ~20% in comparison to the uniform structure. This optimal resistance came with the benefit of sustaining the mass of the prismatic structure. When the lattice was analysed through splitting its structure into different elements, the optimal value of epsilon would range but the altered structures would always perform better than the uniform structure. This applied to both the beam model and unit cell model and of course as discussed, the full complex system of the lattice. In this case, the optimised geometry of the honeycomb infill could offer an innovative favourable change for the development of additively manufactured structures where its current parameters and analysis remains limited.

4.6 Recommendations for Future Research

Upon completing the research for this chapter, the results are very promising but, there are numerous ways in which the work covered could be further elaborated. It is recommended that the following aspects are considered in the future:

- Due to unfortunate circumstances, lattices of various epsilon values were three dimensionally printed but were not experimentally tested. Therefore, a full investigation should be carried out on the optimised structure through conducting more experimental studies (e.g., compression and tensile tests) for the purpose of verifying the results obtained from the numerical analysis and simulations.
- An in-depth comparison between the honeycomb structure made by bees and the optimised structure developed in this chapter should be considered.
- Since the paper covered the optimisation of the geometry in a single plane, changes in further planes could be examined. Or even an analysis of microstructure upon microstructure of the hexagonal lattice.

- Instead of focusing on the honeycomb infill, following the same analysis procedures, research could be carried out to explore the optimisations of other infill patterns' geometries.
- The potential of combining infill structures depending on the structural objective. The hybrid configuration could exhibit versatility.
- Due to the varying masses of the unit cell and lattices dependent on the epsilon values, this is not ideal therefore further numerical analysis should be considered to maintain this property for improved comparison purposes

Chapter 5 – Summary and Conclusions

Chapter 2 has analysed the hexagonal structure and a vital problem of highly stretchable and compressible lattice materials is the underlying geometric nonlinearity. This feature of the lattice was found to cause both the axial softening and stiffening of the constituent beam elements depending on whether a compressive or tensile stress is subjected upon the lattice. An in-depth analysis led to the determination of closed-form expressions of in-plane equivalent elastic properties of the hexagonal lattice configuration. The key sections of this chapter include as mentioned the general methodology and procedure to be followed to derive the elastic properties of the hexagonal configuration as well as the use of ordinary differential equations. Furthermore, special cases were of particularly interest and were defined through approximations which then lead to newly derived expressions. These special cases were namely auxetic hexagonal, rhombus-shaped, and rectangular lattices. The numerical analysis was further validated through finite element analysis. The results in each case show somewhat matching results in the two analytical methods used. As previously mentioned, cases 1 and 4, for both cell angles analysed, show results with miniscule percentage errors ranging between 2 and 10%. Whilst for more complicated cases, namely cases 3 and 6, where two forces are applied to the structures in different directions, the percentage errors were almost triple the errors of the preceding cases discussed. Therefore, for future recommendations of this chapter, further analysis with the aim of reducing these percentages for all cases should be considered as well as also following the same procedure for the three special cases mentioned.

The third and fourth chapter of this paper explores two approaches of optimising a hexagonal lattice configuration through varying the geometry of the constitutive beam elements. One approach was through the introduction of steps whilst the second approach involved the introduction of a quadratic curve on the beam profile. The objective of the optimisation process is to heighten resistive capabilities to deformation whilst maintaining equal masses of the uniform structure. The bottom-up approach has been executed where again, the lattice has been separated into sub systems and individually analysed. This would then be put together to produce the whole honeycomb configuration which is then again analysed as a whole system. Likewise, the validation of results is then again executed through different approaches and methods: numerical analysis and finite element analysis. It was found that for the stepped

lattice analysis, the optimal structure had a young's modulus around 32% larger than the uniform structure whilst for the beam profile optimisation this was found to be ~20%. Both incredibly encouraging results.

Upon completing the research for these chapters, the results are very promising but nonetheless, there is always room for improvement in which the work covered could be further developed. As previously mentioned, the recommended key areas to be considered in the future are as follows: the production of lattice models through 3D printing ready to be experimentally tested, in-depth analysis to fulfil the mass control variable for improved comparison purposes, hybrid configurations depending on the structural objectives.

References

[1] Fernandez-Vicente M, Calle W, Ferrandiz S, Conejero A. Effect of infill parameters on tensile mechanical behavior in desktop 3D printing. 3D printing and additive manufacturing. 2016 Sep 1;3(3):183-92.

[2] Gibson I, Rosen DW, Stucker B. Additive manufacturing technologies. New York: Springer; 2014.

[3] Lipson H, Kurman M. Fabricated: The new world of 3D printing. John Wiley & Sons; 2013 Jan 22.

[4] Pereira T, Kennedy JV, Potgieter J. A comparison of traditional manufacturing vs additive manufacturing, the best method for the job. Procedia Manufacturing. 2019 Jan 1; 30:11-8.

[5] Evans B. Practical 3D printers: The science and art of 3D printing. Apress; 2012 Sep 25.

[6] Attaran M. The rise of 3-D printing: The advantages of additive manufacturing over traditional manufacturing. Business Horizons. 2017 Sep 1;60(5):677-88.

[7] Chu C, Graf G, Rosen DW. Design for additive manufacturing of cellular structures. Computer-Aided Design and Applications. 2008 Jan 1;5(5):686-96.

[8] Amendola A, Carpentieri G, Feo L, Fraternali F. 2016 Bending dominated response of layered mechanical metamaterials alternating pentamode lattices and confinement plates. Composite Structures 157, 71 – 77.

[9] Li X, Gao H. 2016 Mechanical metamaterials: Smaller and stronger. Nature materials 15, 373– 374.

[10] L. 2016 Hierarchical honeycomb lattice metamaterials with improved thermal resistance and mechanical properties. Composite Structures 152, 395 – 402.

[11] Christensen J, Kadic M, Kraft O, Wegener M. 2015 Vibrant times for mechanical metamaterials. 5, 453–462.

[12] Chen Y, Barnhart M, Chen J, Hu G, Sun C, Huang G. 2016 Dissipative elastic metamaterials for broadband wave mitigation at subwavelength scale. Composite Structures 136, 358 – 371.

[13] Zheng X, Lee H, Weisgraber TH, Shusteff M, DeOtte J, Duoss EB, Kuntz JD, Biener MM, Ge Q, Jackson JA, Kucheyev SO, Fang NX, Spadaccini CM. 2014 Ultralight, ultrastiff mechanical metamaterials. Science 344, 1373–1377.

[14] Kadic M, Buckmann T, Stenger N, Thiel M, Wegener M. 2012 On the practicability of pentamode mechanical metamaterials. Applied Physics Letters 100, 1901.

[15] Kim K, Ju J. 2015 Mechanical metamaterials with 3D compliant porous structures. Composite Structures 132, 874 – 884.

[16] Petrovic V, Vicente Haro Gonzalez J, Jordá Ferrando O, Delgado Gordillo J, Ramón Blasco Puchades J, Portolés Griñan L. Additive layered manufacturing: sectors of industrial application shown through case studies. International Journal of Production Research. 2011 Feb 15;49(4):1061-79.

[17] Triantafyllidis N, Schraad MW. 1998 Onset of failure in aluminum honeycombs under general in-plane loading. Journal of the Mechanics and Physics of Solids 46, 1089 – 1124.

[18] Liu W, Wang N, Huang J, Zhong H. 2014 The effect of irregularity, residual convex units and stresses on the effective mechanical properties of 2D auxetic cellular structure. Materials Science and Engineering: A 609, 26–33.

[19] Papka SD, Kyriakides S. 1994 In-plane compressive response and crushing of honeycomb. Journal of the Mechanics and Physics of Solids 42, 1499 – 1532.

[20] Jang WY, Kyriakides S. 2015 On the buckling and crushing of expanded honeycomb. International Journal of Mechanical Sciences 91, 81 – 90.

[21] Li K, Gao XL, Wang J. 2007 Dynamic crushing behavior of honeycomb structures with irregular cell shapes and non-uniform cell wall thickness. International Journal of Solids and Structures 44, 5003 – 5026.

[22] Flores ES, DiazDelaO F, Friswell M, Sienz J. 2012 A computational multi-scale approach for
the stochastic mechanical response of foam-filled honeycomb cores. Composite Structures 94, 1861 – 1870.

[23] Papka SD, Kyriakides S. 1998 Experiments and full-scale numerical simulations of in-plane crushing of a honeycomb. Acta Materialia 46, 2765 – 2776.

[24] L. Gibson, M. F. Ashby, Cellular Solids Structure and Properties, Cambridge University Press, Cambridge, UK, 1999.

[25] D. Dawe, Matrix and Finite Element Displacement Analysis of Structures, Oxford University Press, Oxford, UK, 1984.

[26] S. Adhikari, The in-plane mechanical properties of highly compressible and stretchable 2d lattices, Composite Structures, 2021

[27] S. Adhikari, The eigen buckling analysis of hexagonal lattices: Closed-form solutions, Proceedings of the Royal Society of London, Series - A 477 2251, 2021

[28] S. Mukherjee, S. Adhikari, The in-plane mechanics of a family of curved 2d lattices, Composite Structures, 2021

[29] S.Mukherjee, S.Adhikari, A general analytical framework for the mechanics of heterogeneous hexagonal lattices, Thin-Walled Structures

[30] O.Weeger, N.Boddeti, S.K.Yeung, S.Kaijima, M.L.Dunn, Digital design and nonlinear simulation for additive manufacturing of soft lattice structures, Additive Manufacturing, 2019

[31] S.Balawi, J.Abot, A refined model for the effective in-plane elastic moduli of hexagonal honeycombs, Composite Structures, 2008

[32] L. Gibson, K. Easterling, M. F. Ashby, The structure and mechanics of cork, Proceedings of the Royal Society of London. A. Mathematical and Physical Sciences 377, 1769

[33] T. Mukhopadhyay, S. Adhikari, Effective in-plane elastic moduli of quasi-random spatially irregular hexagonal lattices, International Journal of Engineering Science, 2017

[34] F. Abd El-Sayed, R. Jones, I. Burgess, A theoretical approach to the deformation of honeycomb based composite materials, Composites 10 (4) (1979) 209–214.

[35] O.Weeger, N.Boddeti, S.K.Yeung, S.Kaijima, M.L.Dunn, Digital design and nonlinear simulation for additive manufacturing of soft lattice structures, Additive Manufacturing, 2019

[36] S. Adhikari, T. Mukhopadhyay, X. Liu, Broadband dynamic elastic moduli of honeycomb lattice materials: A generalized analytical approach, Mechanics of Materials, 2021

[37] Y. Jiang, Q. Wang, Highly stretchable 3d-architected mechanical metamaterials, Scientific reports

[38] Malek, S. and Gibson, L., 2015. Effective elastic properties of periodic hexagonal honeycombs. Department of Materials Science and Engineering, Massachusetts Institute of Technology, 77 Massachusetts Ave, Cambridge, MA 02139, USA.

[39] Janbaz, S., Weinans, H. and Zadpoor, A., 2016. Geometry-based control of instability patterns in cellular soft matter. Royal Society of Chemistry.

[40] Y. Wu, Y. Lai, and Z.-Q. Zhang, Elastic Metamaterials with Simultaneously Negative Effective Shear Modulus and Mass Density, Phys. Rev. Lett. 107, 105506, 2011

[41] T. Mukhopadhyay and S. Adhikari, Equivalent in-plane elastic properties of irregular honeycombs: An analytical approach, Int. J. Solids Struct. 91, 169, 2016

[42] N.A. Fleck, V.S. Deshpande, M.F. Ashby, Micro-architectured materials: past. present and future. Proc R Soc London A, 466 (2121) (2010), pp. 2495-2516

[43] A. Amendola, C. Smith, R. Goodall, F. Auricchio, L. Feo, G. Benzoni, F. Fraternali. Experimental response of additively manufactured metallic pentamode materials confined between stiffening plates. Compos Struct, 142 (2016), pp. 254-262

[44] F.K.A. El-Sayed, R. Jones, I.W. Burgess. A theoretical approach to the deformation of honeycomb based composite materials. Composites, 10 (4) (1979), pp. 209-214

[45] M. Tauhiduzzaman, L.A. Carlsson. Influence of constraints on the effective inplane extensional properties of honeycomb core. Compos Struct, 209 (2019), pp. 616-624

[46] S.D. Papka, S. Kyriakides. In-plane compressive response and crushing of honeycomb. J Mech Phys Solids, 42 (10) (1994), pp. 1499-1532

[47] F. Cote, V. Deshpande, N. Fleck, A. Evans. The out-of-plane compressive behavior of metallic honeycombs. Mater Sci Eng: A, 380 (1–2) (2004), pp. 272-280

[48] X.-Z. Yue, K. Matsuo, K. Kitazono. Compressive behavior of open-cell titanium foams with different unit cell geometries. Mater Trans, 58 (11) (2017), pp. 1587-1592

[49] Tanaka K, Nishida M, Ueki G. Shock absorption of aluminum honeycombs for in-plane impacts. In28th International Congress on High-Speed Imaging and Photonics 2009 Feb 10 (Vol. 7126, p. 71260V). International Society for Optics and Photonics.

[50] Clark J, Ali M, Hoffman J, Kara T, Takak S. The effects of functionally graded structures on contact stress distributions in metal hip joints. In2012 38th Annual Northeast Bioengineering Conference (NEBEC) 2012 Mar 16 (pp. 11-12). IEEE.

[51] K. Qiu, Z. Wang, W. Zhang. The effective elastic properties of flexible hexagonal honeycomb cores with consideration for geometric nonlinearity. Aerospace Sci Technol, 58 (2016), pp. 258-266

[52] M. Bodaghi, A. Damanpack, G. Hu, W. Liao. Large deformations of soft metamaterials fabricated by 3d printing. Mater Design, 131 (2017), pp. 81-91